

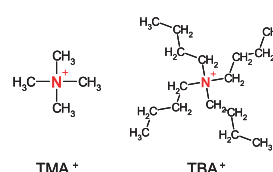
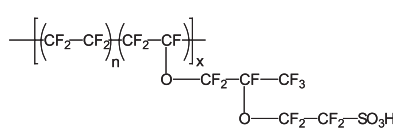
Counter-ion Dynamics and the Mechanical Properties of Fuel Cell Membranes



A key element of hydrogen fuel cells is the proton exchange membrane which serves both as the separator to prevent direct physical mixing of the hydrogen and the oxygen at the electrodes and as the electrolyte for proton transfer. Improvements that relate to structural changes during use are required in several aspects of these membranes in order to improve durability at higher temperatures, increase resistance to fuel crossover, and reduce water transport rates. Perfluorosulfonate ionomers (PFSI's) are of great importance in polymer electrolyte membrane fuel cell (PEMFC) applications. In order to optimize membrane performance, it is essential to understand the mechanisms of morphological changes that affect properties in these materials. This study aims to expand our fundamental understanding of the influence of electrostatic interactions on chain dynamics and developing morphology in PFSI materials. Quasi-elastic neutron scattering (QENS) was used to investigate the correlations between counter-ion dynamics and bulk mechanical relaxations in alkyl ammonium neutralized membranes, thus advancing the current state of understanding of the properties of materials.

FIGURE 1:

Structure of Nafion and the counter-ions tetra-methyl (TMA⁺) and tetra-butyl (TBA⁺) ammonium.



framework of a *static* physically cross-linked network of chains [2, 3].

Given the large incoherent scattering

PFSI's are copolymers containing runs of tetrafluoroethylene and generally less than 15 mol % of perfluorovinyl ether units that are terminated with a sulfonic acid exchange site. The most widely studied PFSI and the focus of this study, Nafion, is a product of the E. I. DuPont Chemical Company (Fig. 1). The polar perfluoroether side-chains containing the ionic sulfonate groups aggregate, thus leading to a nanophase-separated morphology where the ionic domains, termed clusters, are distributed throughout the non-polar polytetrafluoroethylene (PTFE) matrix. This morphology gives a characteristic scattering peak in small angle x-ray scattering at $Q \approx 0.2 \text{ \AA}^{-1}$. The membranes used in this study have been neutralized with tetramethyl (TMA⁺) and tetrabutyl (TBA⁺) ammonium counter-ions (Fig. 1). The size difference between these two counter-ions acts to change the strength of the electrostatic interactions, thus changing the chain dynamics and, in turn, the mechanical properties [1, 2].

length of hydrogen (located only on the counter-ions), the results obtained from QENS can provide specific information about the counter-ion dynamics, thus allowing confirmation and characterization of the ion-hopping process.

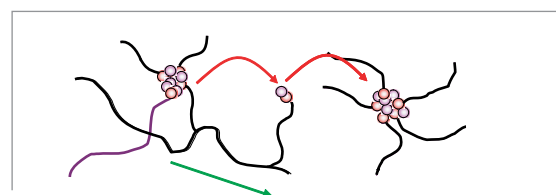


FIGURE 2:

Depiction of the ion-hopping process, in which ions can "hop" from aggregate to aggregate, thus allowing for long-range mobility of the polymer chains.

The temperature dependant elastic scattering at $Q = 0.25 \text{ \AA}^{-1}$ for both TMA⁺ and TBA⁺ Nafion can be seen in Fig. 3. The elastic scattering for each sample is characterized by a distinct drop in intensity, which is attributed to the onset of mobility of the counter-ions that have motions roughly on the size scale of the ionic aggregates. The most striking feature of these data is the excellent correlation between the temperature at which there is a transition in the scattering intensity and the α -relaxation temperature (T_α) obtained by DMA for each material. These data show unequivocally that the α -relaxation is indeed linked to the onset of mobility of the counter-ions, thus lending support to the presence of an ion-hopping process.

Recent studies have shown that the α -relaxation in dynamic mechanical analysis (DMA) of PFSI materials is due to the onset of long-range mobility of both the main and side chains facilitated by a profound weakening of the electrostatic interactions within the ionic aggregates. At temperatures in the vicinity of the α -relaxation, a significant destabilization of the electrostatic network may be observed, which results in the activation of a *dynamic* network facilitated through an ion-hopping process (Fig. 2). In contrast, the β -relaxation is associated with the onset of segmental motions (principally backbone motions) within the

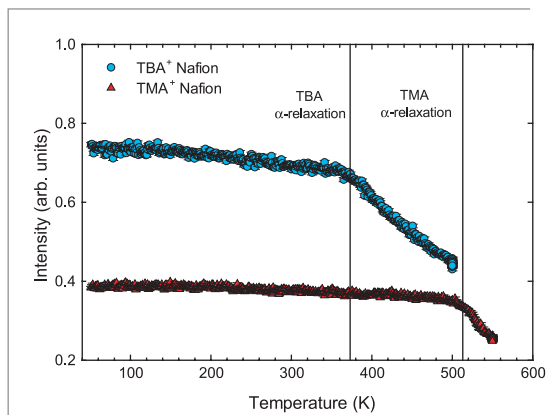
K.A. Page¹
R.B. Moore²
J.K. Park²
V. Garcia Sakai^{3,4}

¹ Polymers Division
National Institute
of Standards and
Technology
Gaithersburg, MD
20899-8542

² The University of
Southern
Mississippi
Hattiesburg, MS
39406

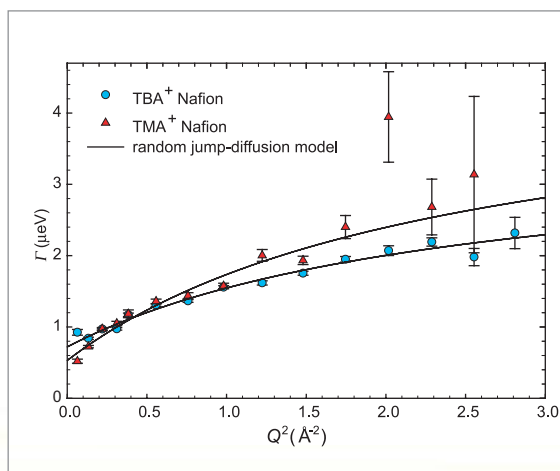
³ NIST Center for
Neutron Research
National Institute
of Standards and
Technology
Gaithersburg, MD
20899-8562

⁴ University of
Maryland
College Park, MD
20742


FIGURE 3:

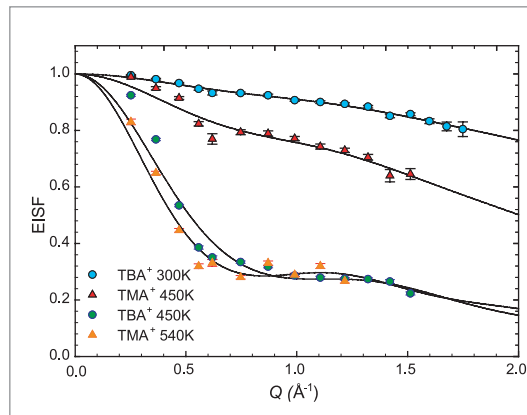
Elastic scattering intensity as a function of temperature ($Q = 0.25 \text{ \AA}^{-1}$) showing the correlation between the bulk mechanical α -relaxation and the onset of mobility of the counter-ions.

Further information regarding the dynamics of the counter-ions was obtained from quasi-elastic scans in the energy range of $\pm 17 \text{ \mu eV}$. By plotting the half-width at half maximum Γ of the quasi-elastic component of the dynamic structure factor $S(Q, \omega)$, the diffusive nature of the counter-ions has been ascertained. The data for both TMA⁺ and TBA⁺ above their respective T_{α} s can be seen in Fig. 4. The non-zero intercept of Γ at low Q values is indicative of spatially confined diffusion of the counter-ions, where the rise in Γ at high Q values indicates random jump-diffusion within the confined region. Below the α -relaxation, a drastic decrease in the mobility of the counter-ions results in less quasi-elastic broadening, thus Γ becomes relatively flat and noisy [4, 5].


FIGURE 4:

The half-width at half-maximum for TMA⁺ and TBA⁺ above their respective α -relaxation temperatures. The solid lines represent a fit of a random jump-diffusion model to the data.

Finally, in order to characterize the dynamic length scales of the counter-ion motions, the elastic incoherent structure factor (EISF) was determined for each sample over a range of temperatures. The EISFs for TMA⁺ and TBA⁺ at temperatures above and below T_{α}


FIGURE 5:

EISF of TMA⁺ and TBA⁺ above and below T_{α} . The solid lines represent the models used to fit the data.

are shown in Fig. 5. Considering the vast difference in counter-ion dynamics above and below T_{α} , it was necessary to fit the EISF with a model describing diffusion between concentric spheres (*i.e.*, on two different length scales) [6]. The EISF for both counter-ions at low temperatures was dominated by diffusion on a very short length-scale ($\approx 1 \text{ \AA}$), which means that the dynamics are dominated by local motions of the alkyl “arms” of the counter-ions.

At temperatures above T_{α} , the EISF showed contributions from diffusion on a larger length-scale. The short-range length-scale was again characteristic of very local diffusive motions, probably facilitated through motions of the alkyl arms of the counter-ion. However, the long-range length-scale was found to be on the order of the size of the counter-ions (6 \AA to 7 \AA). Therefore, within the time-scales measured by QENS, the counter-ion motions appear to be governed by very local motions at temperatures $< T_{\alpha}$. However, at temperatures $> T_{\alpha}$ the counter-ions are able to move over a much larger length scale on the order of magnitude of the size of the counter-ion itself.

In conclusion, using QENS, we have been able to show explicitly that the α -relaxation in these materials is indeed linked to the onset of mobility of the counter-ions on the length-scale related to the characteristic ionomer morphology, thus lending support to the presence of an ion-hopping process. These data provide further fundamental understanding of the link between electrostatic interactions and dynamics in ionomers.

REFERENCES

- [1] K. Mauritz, R.B. Moore, *Chem. Rev.*, **104**, 4535 (2004).
- [2] K.A. Page, K. Cable, R.B. Moore, *Macro.*, **38**, 6472 (2005).
- [3] K.A. Page, F.A. Landis, A.K. Phillips, R.B. Moore, *Macro.*, **39**, 3939 (2006).
- [4] M. Bee, *Quasielastic Neutron Scattering*, Adam Hilger, 1988.
- [5] A. Pivovar, B. Pivovar, *J. Phys. Chem. B.*, **109**, 785 (2005).
- [6] D. Bicout, *Phys. Rev. E*, **62**, 261 (2000).

Novel Magnetic Order in $\text{Na}_{0.5}\text{CoO}_2$

Surprisingly, when you add a bit of water to Na_xCoO_2 , where $x \approx 0.3$, it becomes a superconductor—the first known superconducting cobaltate. The parent compound, non-hydrated Na_xCoO_2 , is a doped spin- $1/2$ magnet on a frustrated triangular lattice. Doping by sodium changes the average valence for the cobalt ions, formally converting magnetic Co^{4+} to non-magnetic Co^{3+} ions. It has been suggested that the average cobalt valence in the superconducting compound is close to that in the half-doped, non-hydrated phase ($\text{Na}_{0.5}\text{CoO}_2$), which is *not* superconducting. Understanding the ground state of the half-doped CoO_2 plane may help distinguish how it differs from the superconducting phase, and will help elucidate the important magnetic interactions.

As a function of sodium doping x , non-hydrated Na_xCoO_2 displays a rich electronic phase diagram, consisting of a paramagnetic phase for $x < 1/2$, and an unusual Curie-Weiss metallic phase for $x > 1/2$. In the half-doped compound ($x = 1/2$), a unique state is realized: The Na ions are chemically ordered to form zigzag chains in an orthorhombic superstructure with two-fold symmetry. Based on resistivity, Hall coefficient, thermal transport, and angular magnetoresistance oscillation measurements, the ground state is believed to be a magnetically ordered insulator. In order to further investigate the electronic ground state of the half-doped CoO_2 plane, we have performed neutron scattering, susceptibility, and transport studies on single crystal samples. The combination of polarized and unpolarized neutron scattering data allows us to determine the ordered spin direction and arrangement. We find that the ground state is well described by an ordered array of stripes of antiferromagnetic spins interleaved with stripes of non-ordered Co ions.

The samples used in this study were prepared by electrochemically de-intercalating a floating-zone grown Na_xCoO_2 crystal to yield a final concentration of $x \approx 0.5$. The crystal studied was cylindrically shaped, with mass 2.41 g (Fig. 1). Our neutron scattering experiments were conducted at the NCNR using the BT-9 and BT-2 triple-axis spectrometers. Neutrons interact with the magnetic moments of the ions and are an ideal probe for studying magnetism in solids.

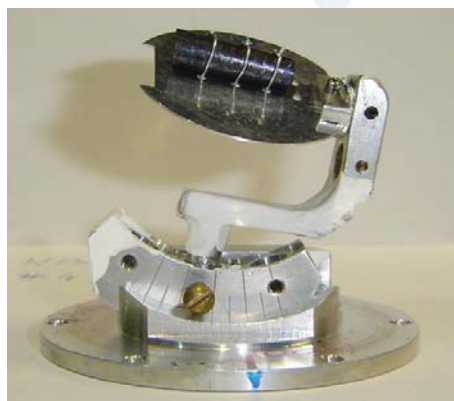


FIGURE 1:

The $\text{Na}_{0.5}\text{CoO}_2$ sample used in our studies, mounted for neutron scattering measurements in (HHL) reciprocal lattice plane.

Figure 2 shows evidence for magnetic order below $T_N = 88$ K obtained by elastic neutron scattering. At low temperatures, new peaks arise that are distinct from nuclear reflection peaks. In the (HHL) reciprocal lattice plane, we observe such peaks at $\mathbf{Q} = (1/2, 1/2, \text{odd})$ locations. The temperature dependence of the peak intensities of the $(1/2, 1/2, 1)$ and $(1/2, 1/2, 3)$ peaks are shown in Fig. 2(a). The observed dependence is typical for second-order magnetic phase transitions. Figures 2(b) and 2(c) show reciprocal-space scans through the $(1/2, 1/2, 1)$ peak along the $[HH0]$ and $[00L]$ directions, respectively, at $T = 8$ K and $T = 120$ K. The low temperature peak widths are resolution-limited, indicating a long-range magnetic order (> 50 Å).

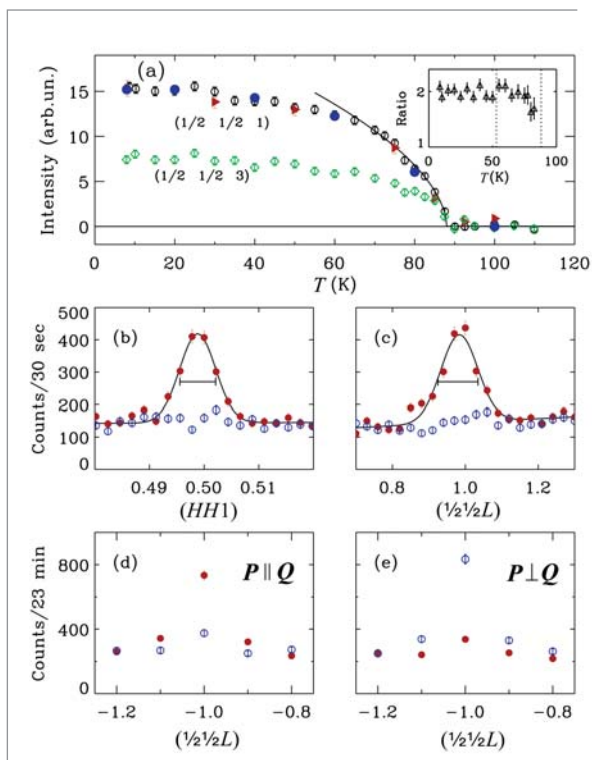
In order to confirm that these peaks originate from magnetic order, we performed polarized neutron measurements. This is the clearest way to distinguish magnetic peaks from weak nuclear superlattice peaks. We have measured both the spin-flip and non-spin-flip cross sections with neutron polarizations (\mathbf{P}) both parallel and perpendicular to the momentum transfer vector (\mathbf{Q}). Figure 2(d) shows the scattering measured at $T = 8$ K with $\mathbf{P} \parallel \mathbf{Q}$ at the $(1/2, 1/2, 1)$ peak. In this geometry, all magnetic scattering occurs in the spin-flip channel (\bullet), and nuclear scattering is non-spin-flip (\circ). The data show that the scattering is entirely spin-flip, *i.e.*, magnetic. The temperature dependence of this scattering, scaled to match the unpolarized data at low T , is denoted by the filled circles in Fig. 1(a). We see that the temperature dependence is identical. Thus, the scattering below 88 K at $(1/2, 1/2, 1)$ is entirely magnetic.

G. Gašparović¹
R.A. Ott¹
J.H. Cho²
F.C. Chou¹
Y. Chu¹
J.W. Lynn³
Y.S. Lee¹

¹ Massachusetts
Institute of
Technology
Cambridge, MA
02139

² Pusan National
University
Busan 609-735,
Korea

³ NIST Center for
Neutron Research
National Institute
of Standards and
Technology
Gaithersburg, MD
20899-8562


FIGURE 2:

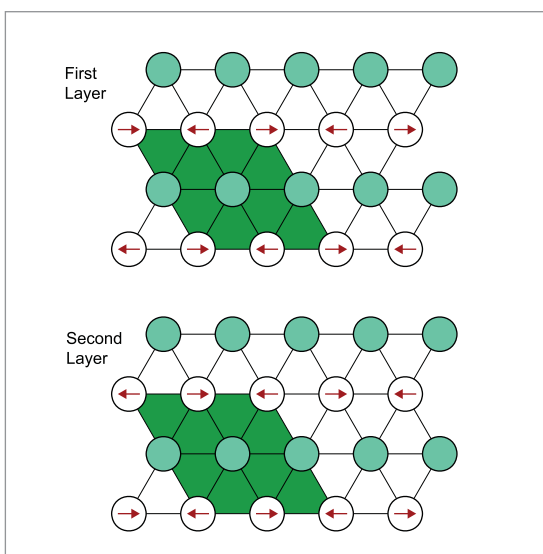
(a) Temperature dependence of the intensities of magnetic Bragg peaks, measured by elastic neutron scattering. The red filled triangles denote the integrated intensities, and the blue filled circles denote the intensities measured using polarized neutrons, both scaled to match the 8 K peak intensity of $(\frac{1}{2} \frac{1}{2} 1)$. (b) $(HH1)$ and (c) $(\frac{1}{2} \frac{1}{2} L)$ scans through $(\frac{1}{2} \frac{1}{2} 1)$ above (\circ , $T = 120$ K) and below (\bullet , $T = 8$ K) the magnetic phase transition. Polarized neutron data with (d) $P \parallel Q$ and (e) $P \perp Q$, for spin-flip (\bullet) and non-spin-flip (\circ) channels at $T = 8$ K.

Neutron polarization analysis is also an extremely useful method to deduce the direction of the ordered moment. In Fig. 2(e), we plot the scattering data measured with $P \perp Q$. In this geometry, magnetic scattering can occur in the non-spin-flip channel if the ordered moment has a component parallel to the polarization direction, whereas a moment along the c -axis would lead to a large spin-flip component. Here, the signal predominately occurs in the non-spin-flip channel. Therefore, the direction of the ordered moments lies within the ab plane, and the ordered moment along the c axis must be small. The temperature dependence of the polarized data indicates that the c -axis component remains small at all measured temperatures below $T_N = 88$ K.

The above information can be combined with measurements of intensities of several nuclear and magnetic Bragg peaks to determine the magnetic structure. Our data are well described by the model shown in Fig. 3. Within each CoO_2 layer, the Co ions are arranged in alternating rows (or stripes) of mag-

netically ordered and “non-ordered” ions. For the magnetic ions, the nearest neighbor spins are coupled antiferromagnetically, both along the row and between rows. Between CoO_2 planes, the rows of magnetic Co ions are stacked directly on top of each other, and the nearest neighbor interplane coupling is also antiferromagnetic. The low temperature ($T = 8$ K) static magnetic moment is $0.26 \mu_B$ per magnetic Co ion. The size of the observed moment is smaller than that expected for $S = \frac{1}{2}$, which may suggest the presence of quantum fluctuations or deviations from a fully charge-disproportionated local moment picture.

In conclusion, our polarized and unpolarized neutron scattering measurements reveal formation of a novel magnetic order in $\text{Na}_{0.5}\text{CoO}_2$ below $T_N = 88$ K. The domains of magnetic order appear to be closely coupled to the domains of Na ion order, consistent with a twofold symmetric spin arrangement. Within each domain, the scattering is consistent with an arrangement of alternating rows of ordered and non-ordered Co ions. Magnetoresistance and anisotropic susceptibility measurements further support this model for the electronic ground state. Understanding the interplay between spin order and charge motion in this correlated electron system remains an important issue for further study.


FIGURE 3:

Model of the spin arrangement in $\text{Na}_{0.5}\text{CoO}_2$. For clarity, only Co ions in the two CoO_2 layers are shown. The solid circles represent non-ordered Co ions, and the hollow circles magnetically ordered Co ions with arrows indicating the directions of the magnetic moments.

REFERENCE

- [1] See G. Gašparović, R. Ott, J.H. Cho, F.C. Chou, Y. Chu, J.W. Lynn, and Y.S. Lee, Phys. Rev. Lett. **96**, 046403 (2006).

A Two-Dimensional Magnetically Ordered Phase on a Geometrically Frustrated Lattice



The two-dimensional (2D) triangular lattice antiferromagnet (TLAFM) is an important model in many areas of condensed matter physics including frustrated magnetism and unconventional superconductivity. Theoretically, TLAFMs have been shown to exhibit many exotic magnetic phases including short-range resonating valence bond [1], Kosterlitz-Thouless and Z_2 -vortex states [2], which are unique to 2D. However, it is difficult to experimentally access these low temperature phases in bulk crystals because there is usually a cross-over to 3D behavior above the magnetic phase transition. Here we show that inter-plane frustration can impede the cross-over to 3D behavior and thus allow one to see intrinsically 2D low temperature physics.

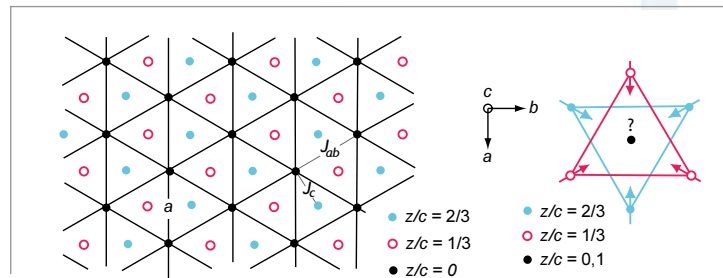


FIGURE 1:

A schematic drawing of the Cr^{3+} sites of NaCrO_2 from a (001) projection (left) showing the nearest neighbor in-plane (J_{ab}) and nearest neighbor inter-plane (J_c) exchange interactions. The $q = (\frac{1}{3}, \frac{1}{3}, 0)$ spin arrangement is shown on the right which illustrates how inter-plane frustration arises.

Of the many materials that are known to possess highly 2D magnetic interactions, those that exhibit a 2D long-range ordered (LRO) phase are extremely rare. This is because even when the inter-plane coupling J_c is much weaker than the in-plane coupling J_{ab} , 3D order is energetically favorable below a temperature T_c at which the in-plane correlation length ξ_{ab} is sufficiently large that

$$k_B T_c = J_c (\xi_{ab}/a)^2 S^2$$

where a is the in-plane inter-spin distance and S is the magnitude of the spin. Therefore a divergence of ξ_{ab} that is driven solely by 2D interactions will simultaneously induce 3D LRO. In a neutron scattering experiment, such behavior is typified by an abrupt conversion from 2D dynamic scattering, due to short-lived in-plane correlations, to 3D Bragg scattering as the system is cooled through the transition temperature. However, if adjacent lattice planes are stacked in such a way that inter-plane interactions cancel out, both the lifetime and spatial extent of in-plane correlations may be allowed to grow without 3D LRO developing.

We investigated such a possibility by performing neutron scattering measurements on the Mott insulator NaCrO_2 , in which ($S = \frac{3}{2}$) Cr^{3+} sites form a rhombohedrally (ABCABC) stacked TL (Fig. 1). Frustrated inter-plane interactions can arise in this system provided the exchange couplings are highly planar and antiferromagnetic. Since this condition forces the spins in each plane to adopt a $q = (\frac{1}{3}, \frac{1}{3}, 0)$ configuration as shown in Fig. 1, the molecular field that a particular spin feels from its

first and second neighboring layers vanishes. A model for the classical ground state of the rhombohedrally stacked TLAFM in the limit $|J_c / J_{ab}| < 3$ was solved by Rastelli and Tassi [3]. They showed that instead of rods through $q = (\frac{1}{3}, \frac{1}{3}, 0)$ in reciprocal space, as would arise from decoupled 120° ordered planes, the ground state is degenerate along helices centered about $q = (\frac{1}{3}, \frac{1}{3}, 0)$. Experimentally however, particular points along the helices would still be selected via further neighbor interactions or quantum order-by-disorder.

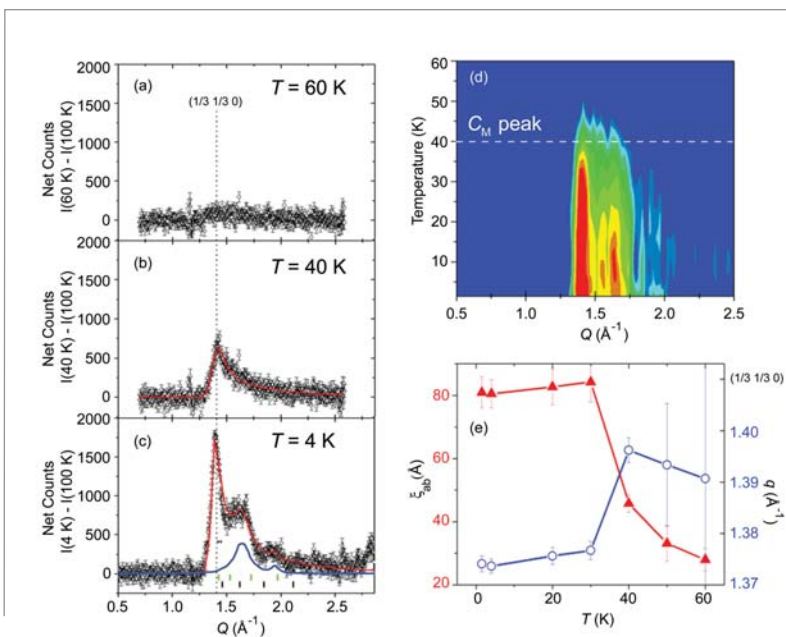
Elastic and inelastic neutron scattering measurements were carried out on a powder sample of NaCrO_2 using the thermal triple-axis spectrometer (BT-9) and the cold neutron Disk Chopper Spectrometer (DCS) respectively. The magnetic diffraction profile at 40 K (Fig. 2b) is well described by a Warren peak centered around $q = (\frac{1}{3}, \frac{1}{3}, 0)$, arising from rods of low energy scattering. The Warren peak is resolution limited in energy, revealing a correlation time exceeding 0.4 ns. As shown in Fig. 2d, this quasi-elastic 2D scattering survives over an unusually large temperature range ($T_l = 35 \text{ K} < T < T_u = 48 \text{ K}$) over which ξ_{ab} grows from $15a$ to $28a$ (Fig. 2e) without the appearance of 3D Bragg peaks. Below T_l , broad peaks emerge along the high q tail of the Warren peak (Fig. 2c) arising from short-range ($\xi_c < 1.08c$) inter-plane correlations. The positions of these peaks cannot be indexed by $(\frac{1}{3}, \frac{1}{3}, n)$ where n is integer or half-integer, which means that the stacking arrangement of the triangular planes is not simply ferromagnetic or antiferromagnetic. A concomitant drop in the Warren peak position at T_l (Fig. 2e)

D. Hsieh¹
D. Qian¹
M.Z. Hasan¹
R.F. Berger¹
R.J. Cava¹
B.G. Ueland²
P. Schiffer²
J.W. Lynn³
Q. Huang³

¹ Princeton University
Princeton, NJ 08544

² Pennsylvania State University
University Park, PA 16802

³ NIST Center for Neutron Research
National Institute of Standards and Technology
Gaithersburg, MD 20899-8562


FIGURE 2:

(a-c) The magnetic contribution to the neutron diffraction pattern of NaCrO₂ along with fits to a combination of Warren and Lorentzian lineshapes (red). Peaks arising from inter-plane correlations are shown in blue (c) and should be compared to the green and black bars which mark the $(\frac{1}{3} \frac{1}{3} n)$; n integer and half-integer positions respectively. (d) shows the temperature dependence of the magnetic diffraction signal and the peak position of the measured magnetic specific heat (C_M) peak. (e) displays the temperature dependence of ξ_{ab} and q extracted from the fits.

NaCrO₂ which support a Heisenberg ($D \approx 0$) character. The origin of the large effective “ D ” term can be understood in analogy with square-lattice

suggests that coupling between planes is instead established by an in-plane modulation of the 120° order which relieves the inter-plane frustration. A departure from purely 120° in-plane order is consistent with a degenerate helix ground state, but the mechanism that lifts the degeneracy is still unclear.

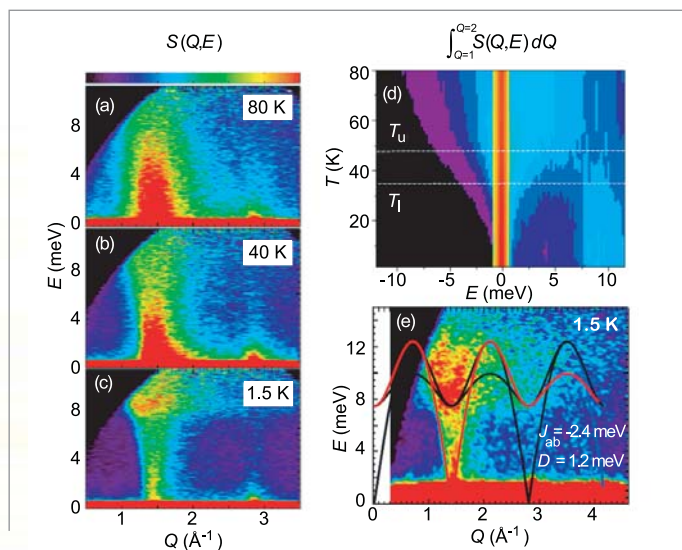
The dynamic structure factor of the spin correlations is shown in Fig. 3a-c. Despite a long in-plane correlation length ($\xi_{ab} = 15a$) at 40 K, there is strong incoherent inelastic scattering and no finite energy spin wave modes, indicating that spin correlations are slowly fluctuating but not truly static. This 2D fluctuation regime is also extended between T_u and T_l (Fig. 3d). Below T_l , dispersive modes that are both gapped and gapless at the Brillouin zone center ($q = 1.4 \text{ \AA}^{-1}$) begin to appear and are well described by the spin wave spectrum of a 2D Heisenberg TIAFM with a single-ion easy-plane anisotropy $D = 1.2 \text{ meV}$ (Fig. 3e). Such a large value of D is inconsistent with electron paramagnetic resonance measurements on

Sr₂Cu₃O₄Cl₂ [4]. Since NaCrO₂ can be separated into multiple Heisenberg AFM sublattices that can be rotated relative to each other without costs in energy, strong fluctuations can then lift one of the zero-energy modes to a finite energy. This provides support for inter-plane correlations developing from an order-by-disorder mechanism.

Our measurements on NaCrO₂ demonstrate that inter-plane frustration provides a new avenue to stabilize 2D magnetic phases in strongly correlated electron systems. Such a phase can be a host for exotic superconductors where pairing could be mediated by spin fluctuations or the lifted zero-modes upon doping.

REFERENCES

- [1] R. Moessner *et al.*, Phys. Rev. Lett. **86**, 1881 (2001).
- [2] H. Kawamura *et al.*, J. Phys.: Condens. Matter **10**, 4707 (1998).
- [3] Rastelli *et al.*, J. Appl. Phys. **63**, 3823 (1988).
- [4] Y. J. Kim *et al.*, Phys. Rev. Lett. **83**, 852 (1999).


FIGURE 3:

(a-c) The dynamic structure factor $S(Q, E)$ of NaCrO₂ where Q and E are the neutron momentum and energy transfers respectively. (d) shows the temperature dependence of the Q integrated dynamic structure factor and the dashed lines enclose the extended fluctuation regime. (e) shows the same data as (c) over a larger dynamic range. The solid lines are the spin wave spectrum calculated using the Hamiltonian $H = -J_{ab} \sum \mathbf{S}_i \cdot \mathbf{S}_j + D \sum (S_i^z)^2$.

Field-Induced Order and Spin Waves in the Pyrochlore Antiferromagnet $Tb_2Ti_2O_7$



Geometric lattices consisting of triangular building blocks are well known venues for phenomena known as magnetic frustration. When combined with antiferromagnetism, such materials often cannot reach a minimum classical ground state energy for the interacting spins, which leads to exotic magnetic ground state behavior. The Disk Chopper Spectrometer (DCS) at the NCNR has allowed us to investigate the influence of an applied magnetic field on the frustrated, pyrochlore antiferromagnet, $Tb_2Ti_2O_7$. These measurements reveal a complex magnetic field versus temperature phase diagram which includes the zero field cooperative paramagnetic phase, a polarized paramagnetic phase and a high-field long-range ordered magnetic phase with spin wave excitations.

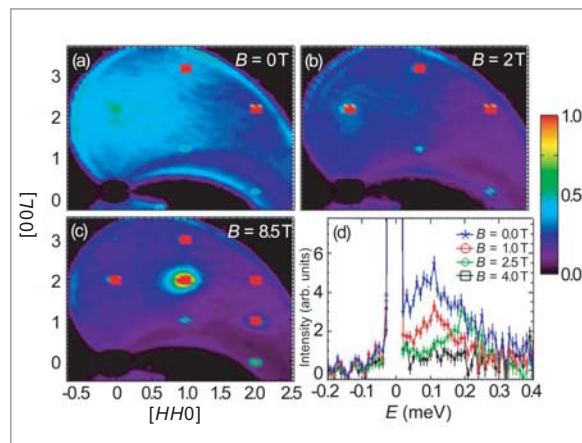


FIGURE 1: Neutron scattering for $-0.5 \text{ meV} < \hbar\omega < 0.5 \text{ meV}$, and within the (HHL) plane of $Tb_2Ti_2O_7$ at $T = 1 \text{ K}$ is shown for (a) $B = 0 \text{ T}$, (b) $B = 2 \text{ T}$ and (c) $B = 8.5 \text{ T}$. Fields were applied along the crystallographic $[110]$ direction. Panel (d) shows high energy resolution scattering at $T = 0.1 \text{ K}$, integrated in Q and including the (002) position.

Bragg intensity when a magnetic field is applied along the Ising $[111]$ axis [5]. Also, combinations of unidirectional and hydrostatic pressure along with magnetic fields have induced magnetic long-range order at low temperatures and applied fields [6, 7]. More recently, in relatively high applied fields and temperatures of 10 K to 20 K , a very slow relaxation rate to an equilibrium state was observed [8].

Time-of-flight neutron scattering measurements were performed with 5 \AA and 9 \AA incident neutrons using NCNR's disk chopper spectrometer (DCS). Figures 1(a-c) show reciprocal space maps in the (HHL) plane, integrating over $-0.5 \text{ meV} < \hbar\omega < 0.5 \text{ meV}$ in energy, and taken at $T = 1 \text{ K}$. In zero field (Fig. 1a), extensive diffuse magnetic scattering was observed around (002) indicating short-ranged spin correlations restricted to distances of about the dimension of a single tetrahedron. This diffuse scattering appears to be quasi-elastic or very weakly inelastic, with a characteristic extent in energy of $\approx 0.3 \text{ meV}$ (Fig. 1d). In a 2 T applied field, oriented along the $[110]$ direction (Fig. 1b), sharp Bragg intensity was observed not only at the allowed nuclear positions, but also at 002 which is forbidden within the $Fd\bar{3}m$ space group. Finally, by 8.5 T (Fig. 1c) a new set of magnetic Bragg peaks was observed signaling a new ordered state. The strongest of these new field-induced peaks is the 112 , as can be seen in Fig. 1c.

$Tb_2Ti_2O_7$ is a geometrically frustrated cubic pyrochlore in which magnetic Tb^{3+} ions are located at the vertices of a network of corner-sharing tetrahedra. At ambient pressure and zero applied magnetic field, $Tb_2Ti_2O_7$ is known to remain a cooperative paramagnet down to temperatures as low as 20 mK [1-3]. Calculations of the crystal field levels appropriate to the Tb^{3+} site predict local $[111]$ Ising anisotropy such that the spins are oriented either into or out from the center of each tetrahedron [4]. Both the ground state and first excited state crystal field levels form doublets which are separated by $\hbar\omega \approx 1.5 \text{ meV}$, while the next highest levels are at $\hbar\omega \approx 10.5 \text{ meV}$ and 14.5 meV [1].

Previous studies show that applied pressure and magnetic fields may relieve the geometric frustration and induce long-range order in $Tb_2Ti_2O_7$. Neutron studies have shown an increase in the nuclear

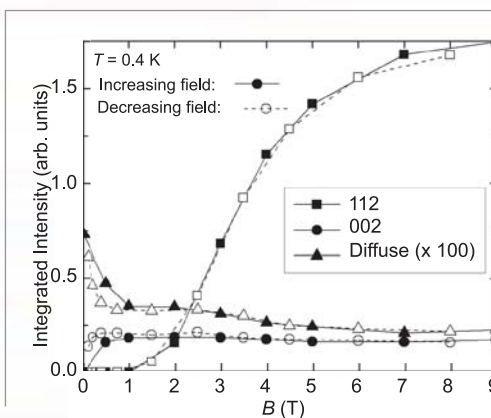


FIGURE 2: The integrated intensity of the 112 and 002 Bragg peaks as a function of B at $T = 0.4 \text{ K}$ are shown, along with the integrated quasi-elastic scattering making up the diffuse scattering.

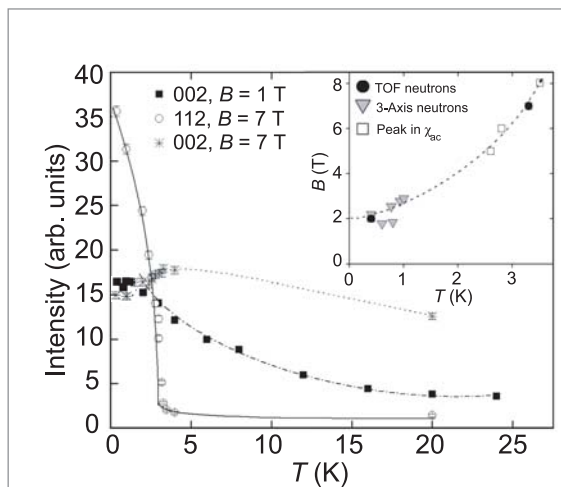
K.C. Rule¹
J.P.C. Ruff¹
B.D. Gaulin¹
S.R. Dunsiger¹
J.P. Clancy¹
M.J. Lewis¹
H.A. Dabkowska¹
I. Mirebeau²
P. Manuel³
J.S. Gardner⁴
Y. Qiu⁴
J.R.D. Copley⁴

¹ McMaster University
Hamilton, ONT, L8S
4M1, Canada

² Laboratoire Leon
Brillouin
CEA-CNRS,
CE-Saclay
91191 Gif-sur-
Yvette, France

³ ISIS Facility
Rutherford Appleton
Laboratory
Didcot, Oxon, OX11
0QX, UK

⁴ NIST Center for
Neutron Research
National Institute of
Standards and
Technology
Gaithersburg, MD
20899-8562

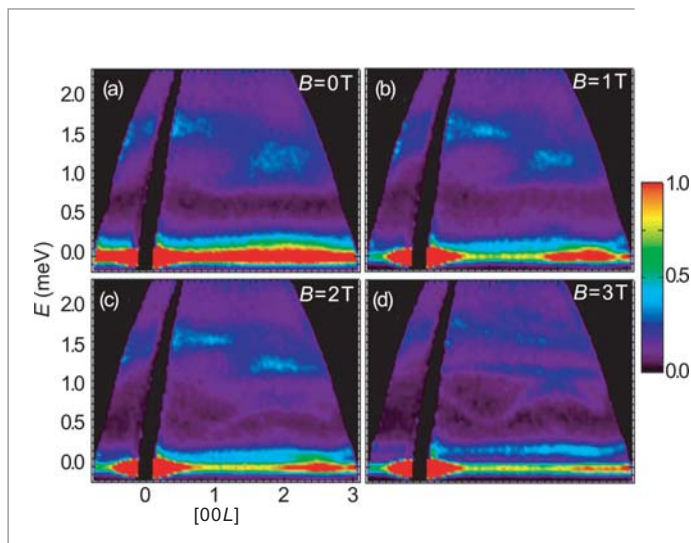

FIGURE 3:

The temperature dependence of the 112 Bragg peak in $B = 7$ T, and the 002 Bragg peak in both $B = 1$ T and 7 T is shown. The inset shows the phase diagram for the magnetically long-range ordered state in $\text{Tb}_2\text{Ti}_2\text{O}_7$, as determined by time-of-flight and triple axis neutron scattering and by ac-susceptibility measurements. All lines shown are guides-to-the-eye.

The intensity of the 002 and 112 Bragg peaks were followed as a function of applied field and temperature. In Fig. 2, the intensity of the 002 peak rises to a maximum by ≈ 0.5 T while the 112 follows an “S-shaped” increase to saturation at around 8 T. Figure 3 shows the temperature dependence of both peaks in applied magnetic fields. At 7 T, the 112 peak falls off sharply with temperature displaying downward curvature with a phase transition near $T_N \approx 3$ K. In contrast, the 002 at 7 T shows an anomaly at T_N but remains finite and large up to at least 20 K.

Figure 4 shows the inelastic magnetic scattering spectrum taken around the (002) position as a function of applied field. In zero field (Fig. 4a), quasi-elastic scattering (responsible for the diffuse scattering in Fig. 2a) can be seen at energies less than ≈ 0.3 meV. As the field was increased, this quasi-elastic scattering appeared to weaken and finally split from the elastic scattering by 3 T (Fig. 4d) leaving a clearly resolved inelastic mode at ≈ 0.3 meV. A broad distribution of inelastic scattering was also observed in zero field between 0.8 meV to 1.8 meV. This inelastic magnetic scattering is also resolved into narrow energy bands as the magnetic field was increased (Fig. 4b-c). At 2 T and 3 T, sharp dispersive spin wave excitations could be seen which appear to have minima in their dispersion near (001) and (003).

These results suggest the 002 Bragg peak which appears on application of a very weak [110] magnetic field, is the signature of a polarized paramagnetic phase. This is supported by the absence of a well defined phase transition associated with the 002


FIGURE 4:

Neutron scattering data within the (00L) - energy plane at $T = 0.4$ K and (a) $B = 0$, (b) $B = 1$ T, (c) $B = 2$ T, and (d) $B = 3$ T are shown.

Bragg intensity with temperature up to 24 K at a field of 1 T (Fig. 3), as well as with the absence of collective spin wave excitations in the magnetic inelastic scattering. In this state, the magnetic Bragg peaks arise from a single-ion polarization of much of the paramagnetic moment along the applied field direction. In contrast, the high field magnetically ordered state shows both well defined spin wave excitations and a clear phase transition at $T_N \approx 3$ K. It is evident, however, that purely [111] Ising spins, as implied by the crystal field calculations, cannot describe the high field state as the dispersive spin wave excitations require continuous spin degrees of freedom. Instead, a model similar to that reported for the pressure induced magnetic order [6, 7] is more likely, suggesting that magnetoelastic effects may play a significant role in the eventual ordering of $\text{Tb}_2\text{Ti}_2\text{O}_7$.

Our DCS results clearly show how the frustrated pyrochlore antiferromagnet $\text{Tb}_2\text{Ti}_2\text{O}_7$ is brought to order at low temperatures by the application of relatively weak magnetic fields applied along [110]. This complex phase behavior and the spin wave dispersion it displays in its high field ordered phase are expected to motivate theoretical study aimed at a complete understanding of $\text{Tb}_2\text{Ti}_2\text{O}_7$ and its enigmatic low temperature behavior.

REFERENCES

- [1] J.S. Gardner, *et al.*, Phys. Rev. B **64**, 224416 (2001).
- [2] J.S. Gardner, *et al.*, Phys. Rev. Lett. **82**, 1012 (1999).
- [3] J.S. Gardner, *et al.*, Phys. Rev. B **68**, 180401 (2003).
- [4] M.J.P. Gingras, *et al.*, J. Phys. Chem. Sol. **62**, 343 (2001).
- [5] Y. Yasui, *et al.*, Phys. Chem. Sol. **62**, 343 (2001).
- [6] I. Mirebeau, *et al.*, Phys. Rev. Lett. **93**, 187204/1 (2004).
- [7] I. Mirebeau and I. N. Goncharenko, J. Phys.: Cond. Matt. **17**, S771 (2005).
- [8] B.G. Ueland, *et al.*, Phys. Rev. Lett. **96**, 27216 (2006).

Resonance Mode in the Electron-Doped Superconducting Cuprate $\text{Pr}_{.88}\text{LaCe}_{.12}\text{CuO}_4$



The nature of the mechanism of high temperature superconductivity (high- T_c) in the cuprates, despite nearly two decades of study, remains one of the major unresolved problems in condensed matter physics. Instead of phonons mediating the electron pairing for superconductivity as in conventional BCS superconductors, it is thought that magnetism plays a fundamental role in the superconductivity of these high- T_c materials, largely because all parent compounds of high- T_c superconductors are long-range ordered antiferromagnets. Studies of universal features in the spin dynamics of the cuprates, via inelastic neutron scattering probing the wave vector and energy dependence of spin fluctuations, provide valuable insight into the precise nature of the interplay between magnetism and superconductivity. We have used the triple-axis spectrometers BT-9 and SPINS at the NCNR to establish a magnetic excitation mode, known as the “resonance”, as the unifying feature in the spin dynamics between hole and electron-doped cuprates. This resonance is therefore an essential component of superconductivity in the cuprates [1].

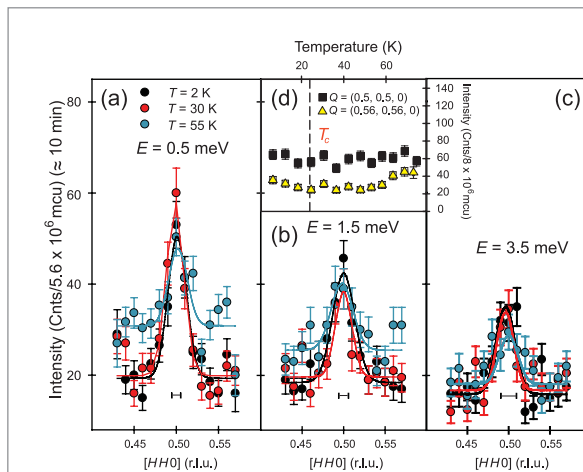


FIGURE 1:

Low energy neutron scattering results from SPINS, (mcu stands for monitor counts units and r.l.u. stands for reciprocal lattice units). a) – c) Constant- E scans through the $\mathbf{Q} = (\frac{1}{2}, \frac{1}{2}, 0)$ point at $E = 0.5$ meV, 1.5 meV, and 3.5 meV, respectively. Scans were taken along the $[HH0]$ direction and show no change from 2 K (black symbols) to 30 K (red symbols). The magnetic scattering centered at (π, π) is much broader than resolution (horizontal bars) and remains gapless down to 0.5 meV. d) T -dependence of 1.5 meV channel at $\mathbf{Q} = (\frac{1}{2}, \frac{1}{2}, 0)$ (black squares) and nonmagnetic background (yellow triangles).

rate wave vector $\mathbf{Q} = (\frac{1}{2}, \frac{1}{2})$, where upon further increase in energy transfer they then disperse back outward but rotated from their original orientation. In $\text{YBa}_2\text{Cu}_3\text{O}_{7-\delta}$, at energies where these incommensurate fluctuations disperse into a commensurate position, a significant enhancement in the spectral weight occurs below T_c and a localized magnetic mode is observed. This mode, known as the resonance excitation, is strongly coupled to superconductivity and appears only below T_c in optimally-doped systems. The resonance mode has also been discovered in a variety of hole-doped systems, and the characteristic energy for this mode, E_R , is intrinsically tied to the superconducting phase of the system through the universal relation $E_R = 5.8 k_B T_c$ thus suggesting that the resonance is linked to the electron-electron pairing mechanism in high- T_c materials.

While the resonance mode and incommensurability are seemingly common in the magnetic spectrum of hole-doped cuprates, the question then arises: are these features also present in the spin excitations of the electron-doped cuprates? In order to address this question, we probed the spin dynamics of the optimally electron-doped cuprate $\text{Pr}_{.88}\text{LaCe}_{.12}\text{CuO}_{4-\delta}$ (PLCCO) with a $T_c = 24$ K. Using the SPINS cold-

The novel phase of high- T_c superconductivity occurs when charge carriers, either holes or electrons, are doped into the CuO_2 planes of their antiferromagnetically (AF) ordered insulating parent compounds. This AF order consists of a simple doubling of the chemical unit cell in the CuO_2 planes, with an in-plane ordering wave vector $\mathbf{Q} = (\frac{1}{2}, \frac{1}{2})$. Upon doping, long-range AF order is dramatically suppressed but strong spin fluctuations persist in all superconducting concentrations. Experiments probing these spin fluctuations in hole-doped cuprates have uncovered a seemingly universal structure of dispersion amongst different families of cuprates. In these hole-doped systems, including the bilayer system $\text{YBa}_2\text{Cu}_3\text{O}_{7-\delta}$ and monolayer cuprates $\text{La}_{2-x}(\text{Sr}, \text{Ba})_x\text{CuO}_4$, low energy magnetic fluctuations are split away from the commensurate $\mathbf{Q} = (\frac{1}{2}, \frac{1}{2})$ wave vector and instead are observed along incommensurate positions $\mathbf{Q} = (0.5 \pm \delta, 0.5 \pm \delta)$. With increasing energy transfer these low energy fluctuations disperse inward until they reach the commensu-

S.D. Wilson¹
P. Dai^{1,2}
S. Li¹
S. Chi¹
H.J. Kang^{3,4}
J.W. Lynn³

¹ The University of Tennessee Knoxville, Tennessee 37996-1200

² Center for Neutron Scattering Oak Ridge National Laboratory, Oak Ridge, Tennessee 37831

³ NIST Center for Neutron Research National Institute of Standards and Technology Gaithersburg, MD 20899-8562

⁴ University of Maryland College Park, MD 20742

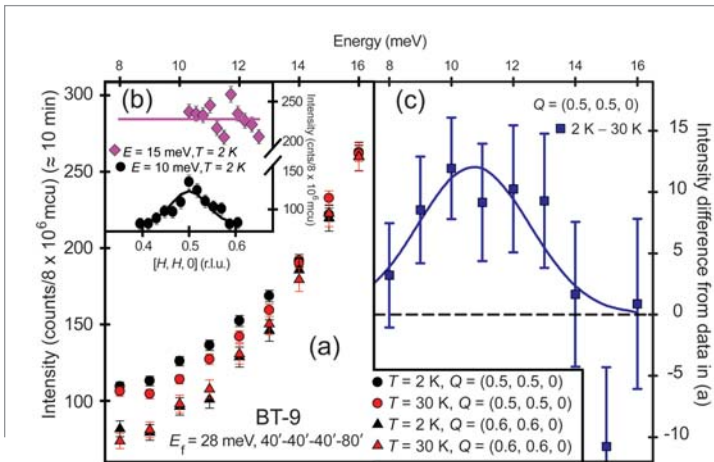


FIGURE 2:

Thermal neutron scattering results from BT-9. a) Constant-Q scans at $(\frac{1}{2}, \frac{1}{2}, 0)$ (circles) and nonmagnetic background (triangles) taken both below and above T_c . b) Constant-E scans at 10 meV (black circles) and 15 meV (purple diamonds) taken through $(\frac{1}{2}, \frac{1}{2}, 0)$ along the $[HH0]$ direction. A clear peak appears at 10 meV centered at $(\frac{1}{2}, \frac{1}{2})$ while no peak is discernible at 15 meV. c) Subtraction of 30 K from 2 K E-scans at $(\frac{1}{2}, \frac{1}{2}, 0)$ in panel (a). A clear localized mode appears centered at ≈ 11 meV when the system is cooled below T_c .

neutron triple-axis spectrometer, our investigations of the low energy excitations of this system reveal that the spin fluctuations are gapless down to 0.5 meV and remain commensurate. This contrasts with the gapped, incommensurate response observed in optimally hole-doped cuprates (Fig. 1). Additionally, these low energy dynamics are independent of the superconductivity in the system as shown by an identical response both below T_c (2 K) and above T_c (30 K). While the commensurate nature of the low energy spin excitations in the electron-doped cuprates seemingly precludes the incommensurability seen in hole-type cuprates as universal to all high- T_c , the question remains as to the existence of the resonance mode in the electron-doped cuprates.

In order to investigate the possible presence of the resonance in PLCCO, we utilized the BT-9 thermal triple-axis spectrometer, allowing higher energy spin excitations to be probed. In the range $8 \text{ meV} \leq \hbar\omega \leq 15 \text{ meV}$ the spin dynamics are no longer decoupled from the onset of superconductivity in the system, and instead, a localized magnetic mode appears as the system is cooled below T_c (Fig. 2). This mode appears centered at ≈ 11 meV and exactly at the commensurate wave vector $(\frac{1}{2}, \frac{1}{2})$. Temperature scans from another spectrometer, HB-1 at Oak Ridge National Laboratory, also confirm that this mode appears only below T_c , and therefore is the identical resonance mode feature observed in hole-doped cuprates.

The resonance energy for this electron-doped system can then be compared to equivalent resonances observed in hole-doped cuprates, as shown in Fig. 3. Surprisingly, E_R for PLCCO falls exactly onto the universal curve for all systems, thus establishing this excitation as fundamental to all high- T_c copper oxides regardless of carrier type. Additionally, the discovery of the resonance mode in a system with known commensurate low energy excitations dispersing into it (Fig. 3) implies that there exists no fundamental connection between the resonance energy

and the inward dispersion of incommensurate excitations observed in the hole-doped classes of cuprates. To fully understand the microscopic origin of the resonance mode requires the use of complementary probes in addition to neutron scattering, such as angle resolved photoemission or scanning tunneling electron-microscopy, for which PLCCO is suitable. Thus, a systematic investigation in a single material is now possible for the first time using several complementary probes, with inelastic neutron scattering providing a foundation for finally deciphering the microscopic origin of the resonance.

REFERENCE

[1] S.D. Wilson, P. Dai, S. Li, S. Chi, H.J. Kang, and J.W. Lynn, Nature 442, 59 (2006).

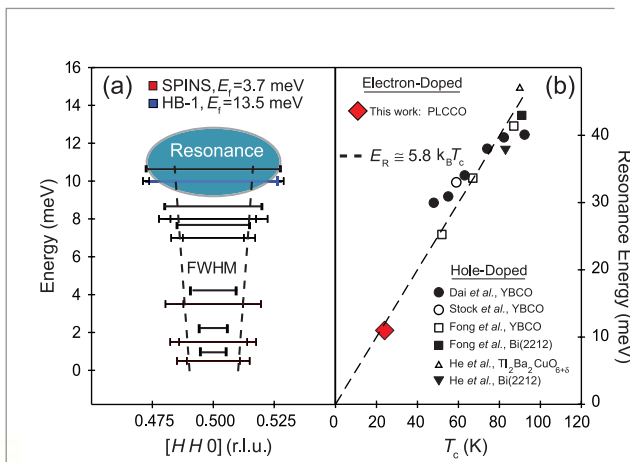


FIGURE 3:

Dispersion relation for PLCCO and universal plot of E_R vs T_c . a) Dispersion of the commensurate excitations in PLCCO with increasing E. Colored bars represent the FWHM of the measured peak along $[HH0]$ while the black bars display the respective instrument's resolution. b) Universal plot showing discovered resonance modes in various classes of cuprates versus their respective system's T_c . The new E_R for PLCCO falls exactly onto the universal curve for all systems, thus signifying a common origin for all resonances in the high- T_c cuprates regardless of carrier type. The citations in the figure can be found in Ref. 1.

Quasiparticle Breakdown in a Quantum Spin Liquid

In the standard microscopic description of condensed matter, elementary excitations, or quasiparticles, are fundamental quanta of energy and momentum. Scattering neutrons from a two dimensional quantum-magnet, we have identified a region of energy-momenta where this description fails [1].

Experiments probed magnons in piperazinium hexachlorodocuprate (PHCC) [2], wherein spin-1/2 copper atoms form a non-magnetic quantum spin liquid ground state. Elementary magnetic excitations in this system are magnon quasiparticles existing above an energy gap. Beyond a threshold where energy and momentum conservation allow one magnon to decay into two, single-particle excitations become unstable and the magnon spectrum ends. In PHCC we have observed a rapid transfer of magnetic intensity to the 2-particle continuum and an abrupt development of damping when a threshold momentum is exceeded.

The quasiparticle concept has proven remarkably successful in describing collective phenomena in condensed matter, in particular quantum fluids which are among the most interesting and fundamental condensed matter systems. The study of quasiparticles which govern the properties of quantum liquids was pioneered by physicist Lev Landau. Landau explained a variety of properties of superfluid ^4He in terms of a system of Bose quasiparticles with a spectrum that has a finite energy minimum (an energy gap) at a particular wave vector [3]. He also realized that the presence of such a quantum gap in the excitation spectrum has dramatic consequences for a quantum Bose liquid and results in an unusual feature – a singular point where the single-quasiparticle spectrum terminates [4]. Like unstable elementary particles in the universe, quasiparticles may not survive beyond an energy-momentum threshold where certain decays become allowed by conservation laws, so the quasiparticle spectrum ends at this threshold. Neutron scattering experiments in ^4He indeed indicate that the spectrum of quasiparticles there (longitudinal acoustic waves, or phonons) ends at about twice the quantum gap energy, where phonon quasiparticles start decaying into pairs of near-gap excitations [1,6].

While only two elemental liquids, the helium isotopes ^4He and ^3He , fail to crystallize at $T = 0$ K, electrons in metals and superconductors and trapped ultracold atoms also form quantum liquids, and some remarkable new examples were recently identified among quantum spins in magnetic crystals [1,2,5]. The organo-metallic material PHCC provides an excellent physical realization of a two-dimensional (2D) quantum spin liquid (QSL). It has Cu^{2+} spins coupled through a complex network of interactions with high degree of frustration, forming a pseudo-

square lattice of $S = 1/2$ dimer pairs in the crystalline $\mathbf{a-c}$ plane [2]. Spin excitations have spectral gap $\Delta_s \approx 1$ meV and a nearly isotropic 2D dispersion relation in PHCC's ($b0l$) plane, with a bandwidth slightly larger than Δ_s , above the gap. In the absence of an external magnetic field, magnetic order in PHCC does not occur down to $T = 0$ K. We explored magnetic excitations in the 2D QSL in PHCC by inelastic neutron scattering and found remarkable similarities with ^4He , particularly where the quasi-particle dispersion reaches the threshold for two-particle decay and interferes destructively with the continuum. There are also distinctions which can be ascribed to the different nature of decay interactions in the 2D QSL.

The generality of the physics underlying termination of the quasiparticle spectrum in ^4He suggests that similar effects may occur in gapped QSLs. The spin-pair dominated structure factor of PHCC is favorable for probing the interaction of magnon quasiparticles with their two particle continuum. In Fig. 1 (a) we present a series of constant wave vector measurements for energies $\hbar\omega \leq 7$ meV along the $[\frac{1}{2}0l]$ and $[b0-1-b]$ directions chosen to elucidate both single-particle and multiparticle excitations and the possibility of spectrum termination in a 2D QSL. There is a clear change in the character of the excitation spectrum at $\mathbf{Q}_c = (b_c, 0, -1-b_c)$ with $b_c \approx 0.15$ near the magnetic Brillouin zone (BZ) boundary, where the one-magnon dispersion reaches the lower boundary of the two-magnon continuum, $\hbar\omega_{2m}(\mathbf{Q}) = \min_q \{ \hbar\omega(\mathbf{q}) + \hbar\omega(\mathbf{Q}-\mathbf{q}) \}$. For $b \leq 0.2$ there are two distinct contributions to magnetic scattering, the resolution-limited quasiparticle peak at lower energy and a broad feature with a sharp onset at higher energy, which we associate with the two-particle continuum. For $b \leq 0.15$ the quasiparticle

M.B. Stone¹
I.A. Zaliznyak²
T. Hong³
C.L. Broholm³
D.H. Reich³

¹ Oak Ridge
National
Laboratory
Oak Ridge, TN
37831

² Brookhaven
National
Laboratory
Upton, NY
11973-5000

³ The Johns
Hopkins
University
Baltimore,
Maryland 21218

peak joins the continuum to form a complex spectral feature that extends from 2.5 meV to 4.5 meV. The first frequency moment integrated over different ranges of energy transfer shown in Fig. 1b illustrates how the oscillator strength is transferred from the quasiparticle excitation to the multiparticle continuum upon approaching the wavevector Q_c where they intersect. This differs markedly from the picture of excitations in $[\frac{1}{2}0l]$ direction shown in Fig. 1a on the left. There, the magnon dispersion is weaker, and single-particle excitation never reaches the boundary of the 2-magnon continuum and therefore does not decay.

Quasiparticles are ubiquitous in nature and quasiparticle spectrum termination as seen in superfluid ^4He can also occur in other condensed matter systems, in quantum magnets in particular. While this has been generally expected, the extent of the phenomenon and how it reveals itself in real materials has not been clear. Our experiments offer a detailed view of quasiparticle decays in the 2D quantum spin liquid of the metallo-organic magnet PHCC. The termination point predicted from the measured quasiparticle dispersion is marked by dramatic changes in the

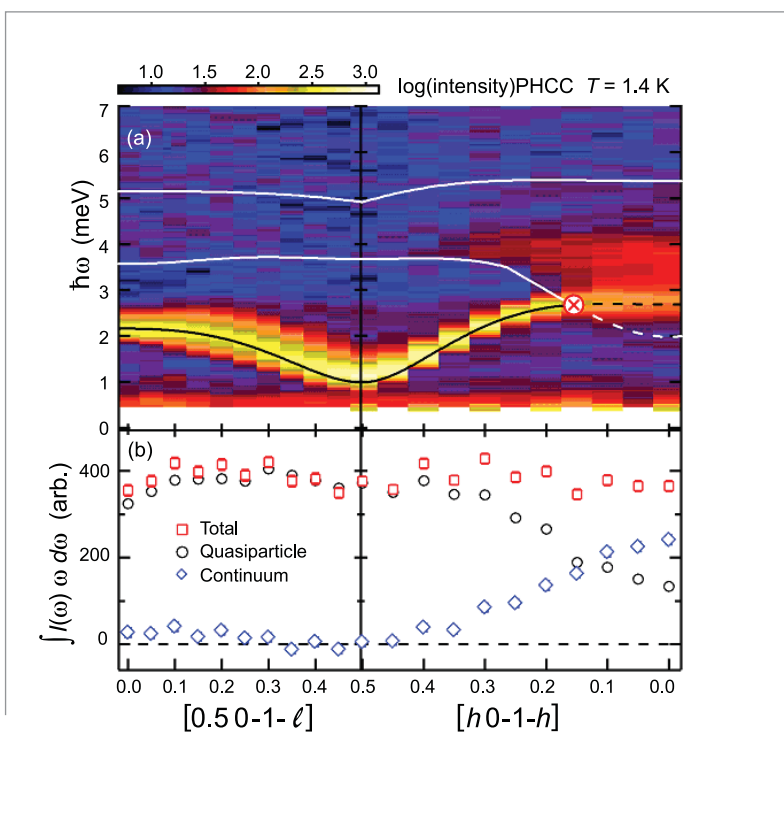
spectrum of magnetic excitations: a rapid transfer of intensity from the magnon peak to the continuum at higher energies and by an abrupt appearance of damping. Our findings have important implications for other quantum magnets such as lamellar copper oxide superconductors where spin excitations above a gap are considered as possible mediators of electron pairing and high-temperature superconductivity.

REFERENCES

- [1] M. B. Stone, I. A. Zaliznyak, T. Hong, C. L. Broholm, D. H. Reich, *Nature* **440**, 187 (2006).
- [2] M. B. Stone, I. Zaliznyak, D. H. Reich and C. Broholm, *Phys. Rev. B* **64**, 144405 (2001).
- [3] L.D. Landau and E. M. Lifshitz, *Course of Theoretical Physics: Statistical Physics, Part 2*, by E. M. Lifshitz, and L. P. Pitaevskii, Vol. 9, 125-139, Pergamon Press, Oxford (1981).
- [4] L. P. Pitaevskii, *Sov. Phys. JETP* **9**, 830 (1959).
- [5] M. B. Stone, J. Rittner, Y. Chen, H. Yardimci, D. H. Reich, C. Broholm, T. Ferraris, and D. V. LECTKA, *Phys. Rev. B* **65**, 064423 (2002).
- [6] B. Fåk, and J. Bossy, *J. Low Temp. Phys.* **112**, 1 (1998), and W. Montfrooij, and E. C. Svensson, *J. Low Temp. Phys.* **121**, 293 (2000).

FIGURE 1:

Magnetic excitation spectrum in PHCC at $T = 1.4$ K. (a) Background corrected intensity along $[\frac{1}{2}0-l]$ and $[h0-1-h]$ directions smoothed by a $\delta\hbar\omega = 0.25$ meV running average applied to each constant wave-vector scan. Black line is the single-magnon dispersion [2], white lines are bounds of the two-magnon continuum calculated from this dispersion. (b) First frequency moment of measured scattering intensity integrated over different energy ranges, $0.8 \hbar\omega \leq 5.5$ meV (red squares, total), $0.8 \leq \hbar\omega \leq 3$ meV (black circles, quasiparticle) and $3 \leq \hbar\omega \leq 5.5$ meV (blue diamonds, continuum).



Radiative Decay Mode of the Free Neutron

Beta decay of the neutron into a proton, electron, and antineutrino is accompanied by the emission of an inner-bremsstrahlung photon. Despite decades of precision measurements of neutron beta decay, this rare branch of a fundamental weak decay has never been observed in the free neutron. We present an experiment to observe the radiative decay mode by detecting photons with energies between 15 keV and 340 keV in coincidence with both the electron and proton emitted in neutron decay.

The neutron is composed of two down quarks and an up quark, and it is stable under the strong and electromagnetic interactions. The weak interaction, however, can convert a down quark into an up quark through the emission of the W gauge boson that subsequently decays into an electron and an antineutrino. This decay is also accompanied by an inner-bremsstrahlung (IB) photon in the rare process $n \rightarrow p + e^- + \bar{\nu}_e + \gamma$, which is an order- α radiative correction to the main branch. While IB has been measured in nuclear beta decay and electron capture decays, the mode has never been observed for the neutron, the fundamental beta decay. A previous experiment resulted in an upper limit of 6×10^{-3} (at the 90 % confidence level) for the branching ratio of photons between 35 keV and 100 keV [1].

15 minutes) makes the rate of detectable photons quite small. An apparatus was mounted at the NG-6 fundamental physics end-station at the Center for Neutron Research at the National Institute of Standards and Technology to search for the decay mode. The experiment registers electron-photon coincidences for electrons followed by a delayed proton, thereby reducing the probability of uncorrelated background events. A strong magnetic field transports charged particles away from the photon detector, which increases the solid angle for detection and minimizes correlated backgrounds. An electrostatic mirror permits one to change the rate of electron-proton coincidences with no change in the photon background rate, thus providing an important systematic check on possible backgrounds.

A cold neutron beam enters parallel to the 4.6 T magnetic field produced by a superconducting solenoid, as illustrated in Fig. 2. When a neutron decays inside the high field region, the charged decay products are confined to move in tight cyclotron orbits typically less than 1 mm in diameter, whose guiding centers are locked to the local magnetic field lines. The solenoid has a slight bend in the magnetic field direction at one end, allowing the decay proton and electron to be guided out of the beam and into a thick silicon surface barrier detector (SBD). The SBD is held at a high negative potential (-25 kV) to accelerate the low energy protons to detectable energies. The apparatus was previously employed on NG-6 to measure the neutron lifetime using a proton trap; its mode of operation has been described in detail elsewhere [4].

Nearly all of the decay electrons have much higher energy (several hundred keV) and reach the detector first, whereas the much slower proton (maximum energy of 751 eV) drifts to the detector a few microseconds later. The electrostatic mirror was constructed in an annular form to permit free passage of the neutron beam, and it was used to reverse the direction of protons with initial momenta away from the detector. Thus, the magnetic field and electrostatic mirror allow for nearly 2π solid angle coverage for the electron detection and up to 4π coverage of the proton detection.

J.S. Nico¹
M.S. Dewey¹
T.R. Gentile¹
H.P. Mumm¹
A.K. Thompson¹
B.M. Fisher²
I. Kremisky²
F.E. Wietfeldt²
T.E. Chupp³
R.L. Cooper³
E.J. Beise⁴
K.G. Kiriluk⁴
J. Byrne⁵
K.J. Coakley⁶

¹ Ionizing Radiation Division
National Institute of Standards and Technology
Gaithersburg, MD 20899-8460

² Tulane University
New Orleans, LA 70118

³ University of Michigan
Ann Arbor, MI 48109

⁴ University of Maryland, College Park, MD 20742

⁵ University of Sussex
BN1 9QH, U.K.

⁶ Statistical Engineering Division
National Institute of Standards and Technology
Boulder, CO 80305

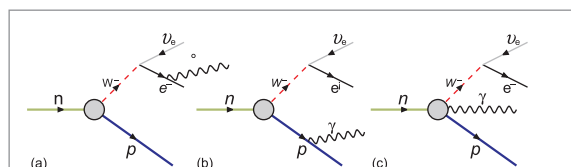


FIGURE 1:

Contributions to radiative neutron decay, showing (a) electron bremsstrahlung, (b) proton bremsstrahlung, and (c) radiation directly from the weak vertex.

The photon energy spectrum and branching ratio for neutron radiative decay has been calculated within a quantum electrodynamics (QED) framework [2] and recently using heavy baryon chiral perturbation (HB_{χ} PT) theory [3]. The QED calculation takes into account the IB produced from the electron and proton (Figs. 1a and 1b) while the HB_{χ} PT approach includes the photon emission from the weak interaction vertex (Fig. 1c). The latter diagram contributes less than one percent and creates only a very slight change in the final photon spectrum and branching ratio calculations; both the photon energy spectrum and the photon polarization observables are dominated by electron IB.

The experimental challenge is to distinguish definitively the low rate of radiative decay events in the large photon background of a neutron beam. The branching ratio above 15 keV is only about 3×10^{-3} , which coupled with the long neutron lifetime (about

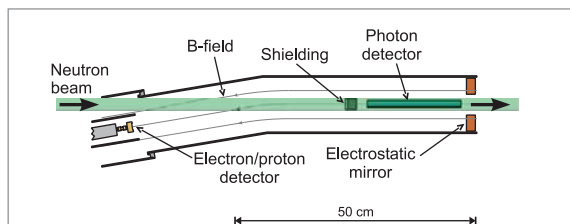


FIGURE 2:

A top-view illustration of the detection scheme for measuring the radiative decay of the neutron. The shielding and photon detector lie below the neutron beam.

To satisfy the need for a large solid-angle photon detector that can operate in a strong magnetic field and at low temperatures, a photon detector consisting of scintillating crystals coupled to avalanche photodiodes was employed. The photon was detected by a single bismuth germanate (BGO) crystal viewed by a silicon avalanche photodiode (APD) [5]. The gain of the APD increases and its noise decreases as the temperature decreases [6]. In addition, BGO exhibits increased light output at low temperatures [7], which reduces the low-energy detection threshold. The BGO crystal was mounted in an aluminum holder and placed below the neutron beam in the downstream end of the bore of the solenoid. The placement of the photon detector well away from the SBD significantly reduces correlated background from external bremsstrahlung photons in the SBD. The photon singles rate, and hence the uncorrelated background rate, was kept low by using a well-collimated neutron beam and gamma-ray shielding.

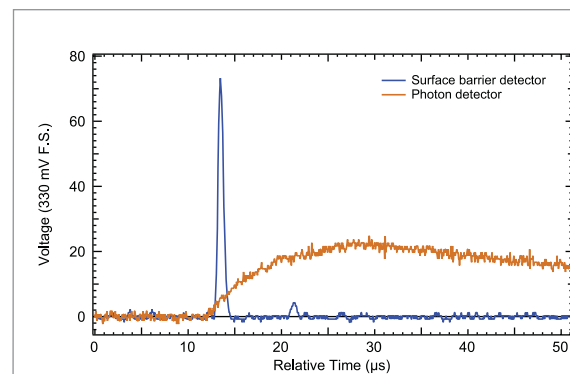


FIGURE 3:

Traces of the digitized waveforms for the two detectors. The blue line shows the SBD signal for an electron event followed by a delayed proton; the orange line shows the much slower pre-amplified output of the APD for a photon event occurring coincident with the electron.

If a proton was detected within a 20 μs timing window after an electron, a conversion signal triggered a computer-based digital oscilloscope board that recorded the amplified electron-proton coincidence signal and the preamplifier output of the APD. Figure 3 shows an example of the two waveforms. Protons are distinguished from electrons based on their pulse heights. Events attributable to radiative decay photons will occur as prompt events in the timing spec-

trum, as shown in Fig. 4, and appear at $-1.25 \mu\text{s}$ due to electronic delays. The approximately 1 μs width of the peak arises primarily from noise on the APD signal. The flat background rate observed is consistent with a calculation of the random coincidence rate determined from the measured singles rates. The apparatus permits a check of correlated back-

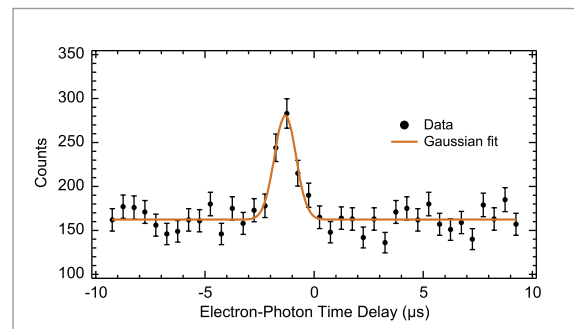


FIGURE 4:

The electron-photon timing spectrum for a three-day run with the mirror reflecting all protons. The spectrum shows all photons in a 20 μs window for which the electron start pulse was accompanied by a delayed proton event.

grounds by varying the electrostatic mirror potential, which changes the electron-proton coincidence rate. The available phase space of the neutron's 4-body decay does not change linearly with the electron-proton rate, in contrast with some sources of correlated backgrounds. Monte Carlo techniques were used to calculate the expected rates as a function of mirror potential. For true radiative decay events, it yields a specific dependence on the neutron decay kinematics and the detector acceptance, thus providing a strong systematic check.

The analysis of the data is in progress; a precise measurement of the photon spectrum should be possible with a straightforward upgrade of the detector by covering more of the available solid angle. A measurement of the spectrum below the 1 % level would reveal the contributions from the weak vertex and provide an alternative determination of the weak coupling constants g_V and g_A . Similarly, if the photon's circular polarization could be measured, it would reveal information about the Dirac structure of the weak current [2,3].

REFERENCES

- [1] M. Beck, *et al.*, JETP Lett **76**, 392 (2002).
- [2] Y. V. Gaponov, R. U. Khafizov, Phys. Atom. Nucl. **59**, 1213 (1996); Phys. Lett. B **379**, 7 (1996); Nucl. Instrum. Meth. A **440**, 557 (2000).
- [3] V. Bernard, S. Gardner, U.-G. Meißner, C. Zhang, Phys. Lett. B **593**, 105 (2004); Phys. Lett. B **599**, 348 (2004).
- [4] J.S. Nico, *et al.*, Phys. Rev. C **71**, 055502 (2005); M.S. Dewey, *et al.*, Phys. Rev. Lett. **91**, 152302 (2003).
- [5] B.M. Fisher, *et al.*, J. Res. Natl. Inst. Stand. Technol. **110**, 421 (2005).
- [6] L. Yang, *et al.*, Nucl. Instrum. Meth. A **508**, 388 (2003).
- [7] H.V.J. Piltingsrud, J. Nucl. Med. **20**, 1279 (1979).

Shear-rate Dependent Structure of Polymer-stabilized TiO₂ Dispersions

How are house-paints designed to spread easily and not lump up or discolor when they are brushed on or applied with other devices? The interactions between polymer chains and colloidal particles are a key to controlling the dispersion of the pigment particles. While studies of polymer-colloid structure and interactions have been performed under quiescent conditions, little is known about the influence of shear (as occurs during brushing) on these properties, where the rheology of such mixtures is strongly shear-rate dependent.

Most paints are typically mixtures of inorganic pigments and latex emulsions, where all particle dimensions are in the range of scattering vectors attainable by light scattering measurements. However, light scattering studies on coatings formulations are not possible due to the opacity/turbidity of these samples. While typical small angle neutron scattering (SANS) measurements are capable of overcoming the opacity issues associated with coatings formulations, the maximum size scale which can be measured by SANS measurements (typical $d_{\text{max}} = 300$ nm) is smaller than the particles encountered in coatings. The perfect crystal diffractometer for ultra-high resolution small-angle neutron scattering (USANS) measurements at the NCNR is capable of measuring size features as large as 10^4 nm, providing the potential for obtaining structural information on coatings formulations which was previously unachievable by other methods.

We measured the shear-rate dependent structure of TiO₂ dispersions (37 % volume fraction) stabilized with commercial polymer dispersants in water. The TiO₂ is a commercial grade product with a nominal particle diameter of approximately 400 nm. The solvent compositions were adjusted to the contrast match point of each dispersant to isolate the behavior of the TiO₂. Two different molecular weight (MW) poly acid dispersants (referred to as “low MW acrylate polymer salt” and “high MW acrylate polymer salt”) and two different molecular weight alkali soluble acrylate copolymers (referred to as “low MW hydrophobic acrylate copolymer salt” and “high MW hydrophobic acrylate copolymer salt”) were used in this study. The shear cell that was used is a couette geometry consisting of double quartz cylinders with a 0.5 mm gap. The shear cell was equipped with a vapor trap which was filled with D₂O to prevent sample drying during the course of the experiment. All experiments were performed at ambient temperature. Data were collected with the incident radiation parallel to the shear gradient and the collected scattering pattern is in the flow — vorticity plane. The shear-rate dependence of the scattering from each

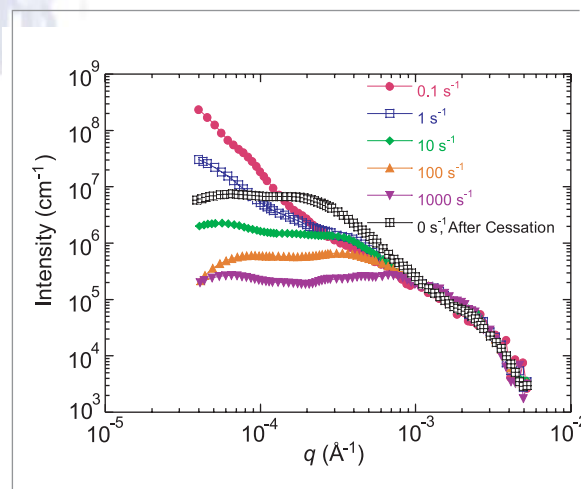


FIGURE 1:

Smearing-corrected shear-rate dependent scattering from a TiO₂ dispersion stabilized with a high MW acrylate polymer salt.

sample was measured at 0.1 s⁻¹, 1 s⁻¹, 10 s⁻¹, 100 s⁻¹, and 1000 s⁻¹. After the measurement at 1000 s⁻¹, the scattering was measured at rest. For each shear-rate a counting time of 3.4 h was employed to obtain good counting statistics. All data were corrected for the empty cell scattering and slit smearing effects.

The shear-rate dependent scattering for each of the TiO₂ dispersions with a different polymer dispersant contrast matched are shown in Figs. 1–4. The TiO₂ dispersed with the high MW acrylate polymer salt shows a decrease in low angle scattering with increasing shear-rate (Fig. 1), indicating a shear induced breakup of aggregates of TiO₂. After cessation of shear, the low angle scattering intensity increases, indicating re-aggregation of the TiO₂ with the high MW acrylate polymer salt. Conversely, the TiO₂ dispersed with the low MW acrylate polymer salt shows a slight increase in scattering with increasing shear-rate (Fig. 2). This indicates a shear induced aggregation of TiO₂ particles. This aggregation appears to be irreversible, since the scattering after cessation of shear has the highest intensity.

A.I. Nakatani¹
A. VanDyk¹
L. Porcar²
J.G. Barker²

¹ Rohm and Haas Company
Spring House, PA
19477

² NIST Center for Neutron Research
National Institute of Standards and Technology
Gaithersburg, MD
20899-8562

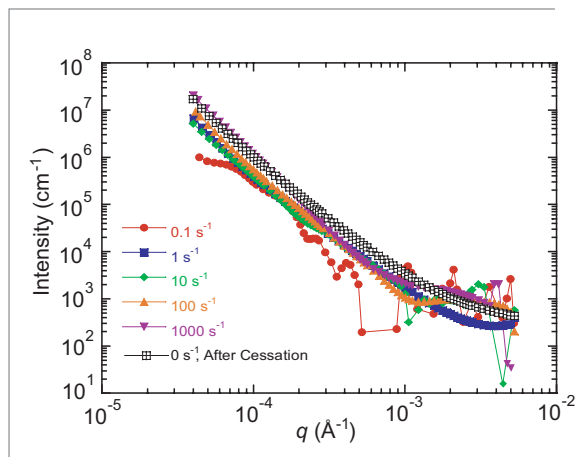


FIGURE 2: Smearing-corrected shear-rate dependent scattering from a TiO_2 dispersion stabilized with a low MW acrylate polymer salt.

The TiO_2 dispersed with the high MW hydrophobic acrylate copolymer salt shows a decrease in low angle scattering intensity with increasing shear-rate (Fig. 3). After cessation of shear, the low angle scattering appears to increase, but not to the level observed at the start of the shear history. These results indicate the TiO_2 dispersed with the high MW hydrophobic acrylate copolymer salt exhibits a shear induced break up of aggregates and after cessation of shear, reaggregation of the TiO_2 occurs. Finally, the TiO_2 dispersion stabilized with the low MW

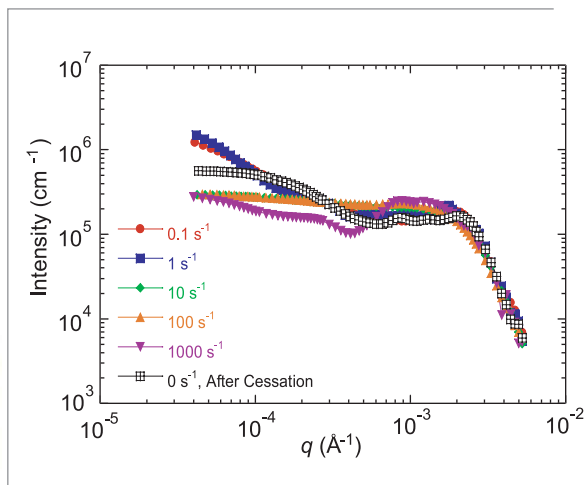


FIGURE 3: Smearing-corrected shear-rate dependent scattering from a TiO_2 dispersion stabilized with a high MW hydrophobic acrylate copolymer salt.

hydrophobic acrylate copolymer salt also shows an increase in low angle scattering intensity with increasing shear-rate (Fig. 4). Therefore, the low MW hydrophobic acrylate copolymer salt also appears to produce a dispersion which undergoes shear induced aggregation. However, on cessation of shear the scattering intensity decreases, indicating the aggregates formed during shear slowly redisperse.

We believe these are the first results which demonstrate the sensitivity of dispersions to the molecular weight and chemistry of the dispersant molecules, along with the shear-rate dependent behavior of the dispersions. The unique capabilities of the USANS instrumentation were a key in obtaining these results. The complimentary study of these dispersions, in which the TiO_2 has been contrast matched, so the scattering from the dispersant molecules as a function of shear-rate will be reported separately.

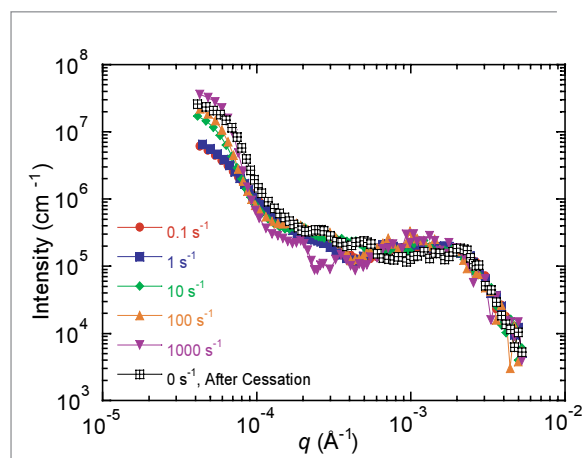


FIGURE 4: Smearing-corrected shear-rate dependent scattering from a TiO_2 dispersion stabilized with a low MW hydrophobic acrylate copolymer salt.

Changes in Blood Protein Structure under Static and Hydrodynamic Shear Conditions

The binding of multimeric blood plasma protein von Willebrand factor (VWF) to platelet receptor Gplb α under high shear stress is an important step regulating atherothrombosis [2,3] (Fig. 1). The function of this protein is also altered under pathological fluid flow conditions in abnormally constricted (stenosed) arteries. In the current study we measured the structure in solution of VWF that was isolated from various human blood-type samples. In order to understand how the individual domains of VWF are organized in the multimeric protein, a dimeric form of the protein called protomer VWF was produced recombinantly and its solution structure was also measured. Finally, in order to determine if large scale or local protein structural changes are sufficient to affect function, we measured VWF conformation under two distinct conditions: upon addition of denaturant (Guanidine-HCl) and under fluid shear.

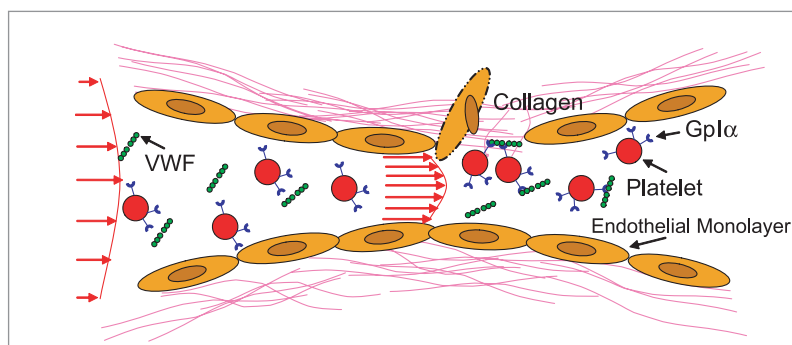


FIGURE 1:

Immobilized von Willebrand Factor (VWF) binding to platelets promotes platelet deposition at sites of vascular injury where the endothelial monolayer is disrupted. High fluid shear stress as may occur in constricted (stenosed) regions of the arterial circulation may also promote VWF binding to specific receptors on blood platelet surface.

Light scattering and small-angle neutron scattering (SANS) were applied under static (no fluid flow) conditions to study the solution structure of human VWF multimers and protomer. Our observations suggest that these proteins resemble prolate ellipsoids in solution with radii of gyration (R_g) of ≈ 75 nm and ≈ 30 nm for the multimer and protomer forms, respectively. The ellipsoid major and minor axes radii were of length ≈ 175 nm and ≈ 28 nm for multimers, and ≈ 70 nm and 9.1 nm for protomers. The multimer is organized into substructural domains at length scales indicative of the entire protein itself (≈ 75 nm), elements of the protomer quaternary structure (≈ 16 nm), and individual functional domains (≈ 4.5 nm) (Fig. 2a). Individual domains of ≈ 4.5 nm were also observed in the protomer. Amino acids occupied a small ($\approx 2\%$) volume in both multimeric and protomer VWF ellipsoids, compared to other proteins like bovine serum albumin (98%) and fibrinogen (35%). ADAMTS-13, a metalloprotease that cleaves VWF, is found in blood, and the absence of this protease leads to severe bleeding complications. In our studies, we observed that treatment of VWF with 1.25M denaturant Guanidine-HCl, which increases the susceptibility of VWF to proteolysis by ADAMTS-13, caused local structural changes at length scales below 10 nm without altering the protein R_g (Fig. 2b). Measurements by other methods reveal a pattern of dimer and trimer units that indicate stable non-covalent interactions within the multimer.

Since the function of von Willebrand Factor is altered upon application of fluid forces, VWF isolated from blood plasma cryoprecipitate was placed in a quartz couette cell [4] (Fig. 3a) and laminar fluid shear was applied in the range from 300/s to 3000/s. SANS measurements were simultaneously performed to assay *in situ* protein solution structural changes in response to hydrodynamic forces. In five out of six different experiments performed with different pools of human VWF, we observed changes at length scales < 10 nm (Fig. 3b) which were reminiscent of the above-mentioned changes in protein structure upon addition of denaturant Guanidine-HCl. These structural changes were irreversible on the time scales studied. Further, even though careful studies were performed to test the hypothesis that changes in protein conformation on a larger scale take place in response to fluid shear, no unequivocal evidence in support of this view was obtained. Control runs were performed to confirm that the observed protein conformation change can indeed be attributed to VWF in solution and not to VWF bound to the Couette-wall. Our studies also show that changes in neutron scattering patterns were specific to VWF, since a smaller protein bovine serum albumin did not undergo similar changes in scattering intensity upon application of fluid shear.

S. Neelamegham¹
I. Singh¹
P. Alexandridis¹
L. Porcar^{2,3}

¹ State University of New York at Buffalo
Buffalo, NY 14260

² NIST Center for Neutron Research
National Institute of Standards and Technology
Gaithersburg, MD 20899-8562

³ University of Maryland
College Park, MD 20742

Overall, the small angle scattering and biochemical investigations performed under no flow conditions demonstrate for the first time that the VWF solution structure is stabilized by non-covalent interactions between different monomer units. Studies performed with Guanidine·HCl suggest that local, and not large-scale, changes in protein conformation are sufficient for ADAMTS-13 mediated proteolysis. Studies performed under fluid shear conditions also support the proposition that local changes at length scales < 10 nm may have significant functional consequences during human vascular pathologies. These functional alterations may be due to changes in the nature of interaction between neighboring domains of VWF or due to release of non-covalent interactions that stabilize VWF solution structure under static con-

ditions. Finally, the results motivate further biochemical and small angle scattering investigations of VWF structure at smaller time scales and under different shear protocols.

SANS data were obtained using the 30m NG-3 instrument. The study was supported by NIH grants HL76211 and HL77258.

REFERENCES

- [1] G. Beaucage, G., J. Appl. Crystallog. **29**, 134 (1996).
- [2] Z.M. Ruggeri, Nat. Med., **8** (11) 1227 (2002).
- [3] H. Shankaran, P. Alexandridis, and S. Neelamegham, Blood **101**, 2637 (2003).
- [4] L. Porcar, W.A. Hamilton, P.D. Butler, and G.G. Warr, Rev. Sci. Inst. **73**, 2345 (2002).

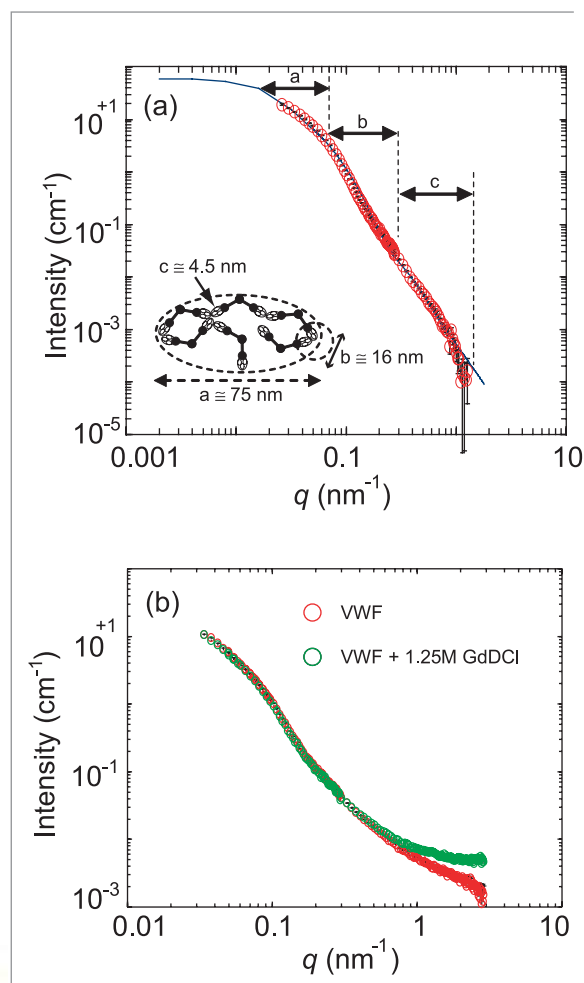


FIGURE 2:

(a) Small angle scattering data were fit to the unified equation in Ref. 1. This analysis revealed that human VWF has three distinct structural levels a, b, c within multimeric protein. Level a is the multimeric molecule, b is an intermediate structure that likely represents the globular domain at the N-terminus of VWF, and c represents individual protein domains. Discrete points represent experimental data while smooth lines are model fits. (b) SANS data for multimeric VWF before and after treatment with 1.25M Gd·DCI shows that Gd·DCI does not affect the R_g of the protein, though it alters structural features at length scales < 10 nm.

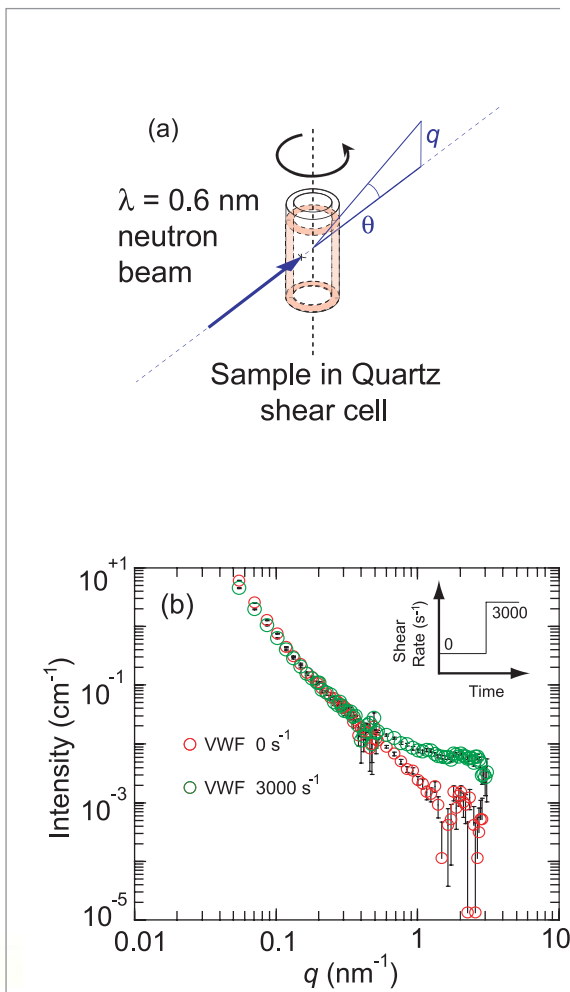


FIGURE 3:

(a) Schematic drawing of a couette shear cell in which VWF was sheared and protein solution structure was evaluated in real-time. (b) A representative shear run where the fluid shear rate was increased from 0/s to 3000/s at a fixed time point. Increase in scattering intensity is observed in the high q range and a small decrease is observed at low q .

Recent advances in preparing double-network hydrogels (DN-gels) from crosslinked polyelectrolyte and linear polymer have resulted in materials with fracture toughness comparable to that of joint cartilage while containing more than a 90 % volume fraction of water (Fig. 1) [1]. DN-gels are prepared by polymerizing a high molecular weight linear polymer within a swollen polyelectrolyte network. In general, the polyelectrolyte network is rigid but extremely fragile (like jelly) while the neutral linear polymer is highly viscous but readily deformable (like putty).

Since neither of the components is individually tough, the unique double-network morphology should be expected to account for this intriguing mechanical behavior. Here we highlight the use of neutron scattering in determining, for the first time, the structure of DN-gels as well as the structure of the individual components. To cover a broad range over four orders-of-magnitude in wavevector q , data from both ultra-small angle neutron scattering (USANS) and SANS were collected and compiled from each sample. The measurements were made using USANS instrument at BT-5 and the SANS diffractometers at NG-3 and NG-7 at the NCNR.

The DN-gels studied in this work were prepared *in situ* by polymerizing linear polyacrylamide (PAAm) at several concentrations within a crosslinked poly(2-acrylamide,2-methyl,1-propanesulfonicacid) (PAMPS) network. The total network structure was rendered observable using neutron scattering contrast by immersing the hydrogenated double-networks in deuterated water. To determine the structure of PAAm chains within the DN, samples were prepared by polymerizing deuterium-labeled acrylamide monomer (d_3 -PAAm) within the PAMPS network swollen in regular water. Matching the neutron contrast of the d_3 -PAAm chains with that of a mixture of light and heavy water then allows us to characterize the PAMPS network structure within the DN-gels. Figure 2 shows the total structure of DN-gels measured over four orders-of-magnitude in wavevector, q . The scattering intensity at ultra-small angles ($I(q)$, $q \rightarrow 0.00001 \text{ \AA}^{-1}$), which is related to the extent of heterogeneity in DN-gels, surprisingly, decreases with the addition of PAAm to the PAMPS single-network. This suggests that the PAAm chains are preferentially situated within the low crosslink density regions of

the PAMPS gel, thus resulting in a gradually homogenized double-network structure with increasing PAAm concentration [2]. But the heterogeneity reoccurred to some extent for the DN-gel with more than 1.5M polyacrylamide. While the initial homogenization of the PAMPS network slightly improved the toughness of DN-gels prepared at low PAAm concentration, the toughest of the DN-gels, containing more than 1.5M PAAm, is almost as heterogeneous as the primary PAMPS network. However, the individual component structure of PAMPS and PAAm within the DN-gels gets homogenized at high PAAm loadings, as determined from the USANS results.



FIGURE 1: Pure PAMPS gel breaks down under compression at 40 % by volume (a), but the toughest DN-gel regains its size and shape after 90 % compression by volume (b). (Reproduced with permission from Ref. 1.)

T. Tominaga^{1,2}
 V.R. Tirumala¹
 P. Butler³
 E.K. Lin¹
 H. Furukawa²
 J.P. Gong²
 Y. Osada²
 W-L. Wu¹

¹ Polymers Division
 National Institute
 of Standards and
 Technology
 Gaithersburg, MD
 20899-8541

² Hokkaido
 University
 Sapporo, Japan

³ NIST Center for
 Neutron Research
 National Institute
 of Standards and
 Technology
 Gaithersburg, MD
 20899-8562

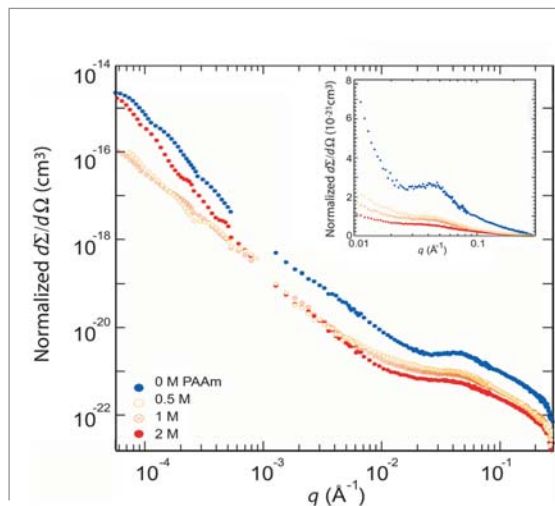


FIGURE 2: SANS and USANS data from DN-gels prepared at different PAAm concentrations as shown in the legend. The inset shows the change in the polyelectrolyte scattering peak with the addition of PAAm. The data are normalized to the contrast factor.

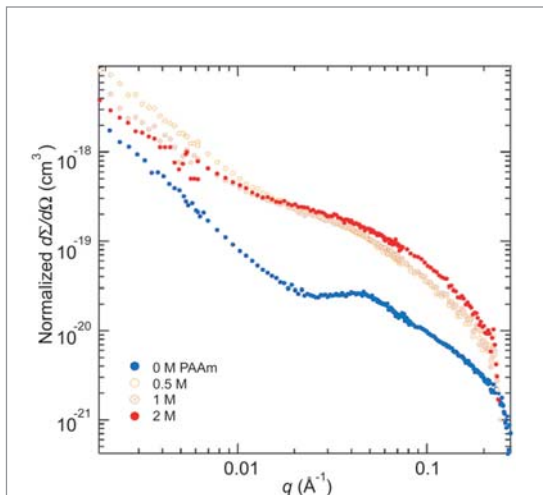


FIGURE 3: SANS data from the PAMPS network alone measured from DN-gels prepared at different PAAm concentrations shown in the legend. The data are normalized to the contrast factor. The PAAm network has been rendered invisible by contrast-matching it to the aqueous matrix.

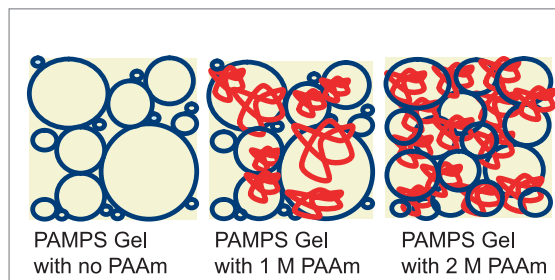


FIGURE 4: Schematic diagram showing the evolution of double-network structure from the primary PAMPS gel with increase in PAAm concentration from 0 M to 1 M and 2 M. PAMPS and PAAm are represented by blue and red colors respectively.

The scattering data at high- q offers insight into the interactions between the linear PAAm and the PAMPS network. A well-defined scattering peak resulting from intrachain correlations is characteristic of a swollen polyelectrolyte in a polarizable medium [3]. For the present case of the PAMPS primary network used in DN-gels, this scattering maximum occurs at $\approx 0.045 \text{ \AA}^{-1}$. By making the PAAm network invisible using contrast matching to the aqueous matrix, the behavior of the PAMPS network alone can be measured.

Figure 3 shows the result of varying the (invisible) PAAm concentration on the PAMPS peak. The peak position remains constant for DN-gels at all PAAm concentrations but the peak amplitude diminishes with PAAm loading since the electrostatic repulsion is screened by PAAm. This is noteworthy since PAAm is not expected to be sufficiently ionized to screen out the electrostatic repulsions among the PAMPS, even though water soluble. Regardless of their origin, the SANS results at high q suggest strong interactions between PAMPS and PAAm in aqueous solution. From these results, the structural changes in the PAMPS gel with the addition of PAAm to form the toughest DN-gel can be conceptualized as shown in Fig. 4. We are currently investigating the origin of these interactions to further determine their effect on the fracture toughness of DN-gels.

REFERENCES

- [1] J.P. Gong, Y. Katsuyama, T. Kurokawa, Y. Osada, *Adv. Mater.* **15**, 1155 (2003).
- [2] Y.-H. Na, T. Kurokawa, Y. Katsuyama, H. Tsukeshiba, J.P. Gong, Y. Osada, S. Okabe, T. Karino, M. Shibayama, *Macromolecules* **37**, 5370 (2004).
- [3] V.M. Prabhu, E.J. Amis, D.P. Bossev, N. Rosov, *J. Chem. Phys.* **121**, 4424 (2004).

A Mechanism for the Onset of Bioactivity in Biomolecules



At low temperatures biomolecules (proteins and DNA) exist in a glassy state, a state which has no conformational flexibility and shows no biological functions. In a hydrated biomolecule, at and above 220 K, this flexibility is restored and the protein or DNA is able to sample more conformational sub-states, thus becoming biologically functional. This 'dynamical' transition of biomolecules is believed to be triggered by its strong coupling with the hydration water, which also shows a similar dynamic transition. Our experiments described below demonstrate that the origin of the characteristic temperature controlling both the activity of the biomolecules and the transition in the behavior of $\langle x^2 \rangle$ is the Fragile-to-Strong dynamic crossover (FSC) phenomenon in the hydration water, which shares the same crossover temperature at 222 ± 2 K with the biomolecules. At the FSC, the structure of hydration water makes a transition from predominantly high-density (more fluid state) to low-density (less fluid state) forms derived from existence of the second critical point at an elevated pressure.

Using the high-resolution quasielastic neutron scattering (QENS) method at the High Flux Backscattering Spectrometer (HFBS) at the NCNR and the Relaxing-Cage Model (RCM) [1] for the analysis, we determine the temperature dependence of the average translational relaxation time, $\langle \tau_T \rangle$, for the hydration water. The dynamic crossover temperature of hydration water is defined as follows. At high temperatures, $\langle \tau_T \rangle$ follows a super-Arrhenius behavior (called a 'fragile' behavior [2]) describable approximately by a Vogel-Fulcher-Tammann (VFT) law: $\langle \tau_T \rangle = \tau_1 \exp[DT_0/(T - T_0)]$, where D is a constant providing the measure of fragility and T_0 , the ideal glass transition temperature at which the relaxation time appears to diverge. In reality, however, this divergence is avoided by the system. Instead, an Arrhenius behavior (called a 'strong' behavior [2]) sets in below the crossover temperature T_L where the functional dependence of the relaxation time switches to a law: $\langle \tau_T \rangle = \tau_1 \exp[E_A/k_B T]$. In this equation, E_A is the activation energy for the relaxation process and k_B , the Boltzmann constant. The crossover temperature T_L is defined by the intersection of these two laws, which gives $1/T_L = 1/T_0 - (Dk_B)/E_A$. In the case of hydration water in both lysozyme protein and DNA, we found $T_L = 222 \pm 2$ K, which agrees well with the characteristic transition temperature in protein observed before [3]. Since the average relaxation time $\langle \tau_T \rangle$ is a measure of the mobility of a typical hydration water molecule, this result implies that the sudden change in the trend of mobility of water molecules at the crossover temperature triggers the so-called glass transition of biomolecules [4-7].

Figure 1 shows the mean-squared hydrogen atom displacements $\langle x^2 \rangle$ (calculated from the translational Debye-Waller factor, $S_H(Q, \omega = 0) = \exp[-Q^2 \langle x^2 \rangle]$)

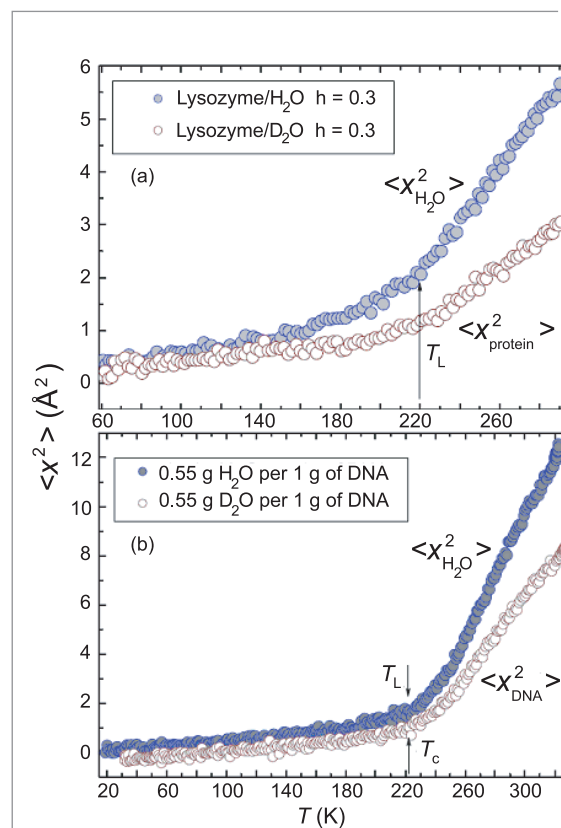


FIGURE 1:

Mean-squared atomic displacement $\langle x^2 \rangle$ of all the hydrogen atoms at 2 ns time scale measured by an elastic scan with resolution of 0.8 μeV (HFBS at NIST), as a function of temperature for H_2O hydrated and D_2O hydrated protein (Panel a) and DNA (Panel b). The solid circles represent $\langle x^2 \rangle$ dominated by contributions from H atoms in hydration water, while the empty circles, that dominated by H atoms contained in protein or DNA molecules.

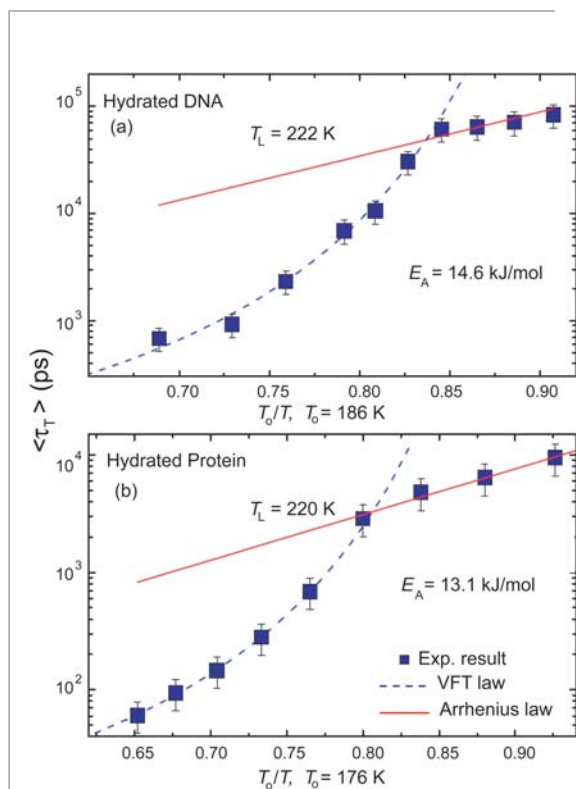
S-H. Chen¹
L. Liu¹
X. Chu¹
Y. Zhang¹
E. Fratini²
P. Baglioni²
A. Faraone^{3,4}
E. Mamontov^{3,4}
V. Garcia Sakai^{3,4}

¹ Massachusetts Institute of Technology Cambridge MA 02139

² University of Florence 50019 Florence, Italy

³ University of Maryland College Park, MD 20742

⁴ NIST Center for Neutron Research National Institute of Standards and Technology Gaithersburg, MD 20899-8562


FIGURE 2:

The extracted Q -independent average translational relaxation time $\langle \tau_T \rangle$ vs. T_0/T from fittings of the quasielastic spectra plotted on a log scale. Panel (a) is a result from hydrated DNA [8], whereas Panel (b) is the same quantity measured in hydrated lysozyme protein [9]. There is clear evidence in both cases that a well-defined cusp-like dynamic crossover behavior occurs at T_L indicated in the respective figures. The dashed lines represent fitted curves using the VFT law, while for the solid lines the fitting is according to the Arrhenius law. T_L in both cases occurs at 222 ± 2 K.

obtained by a method of elastic scan in hydrated lysozyme protein (Panel a) and hydrated DNA (Panel b), respectively. In both panels, one sees that at low temperatures up to their respective crossover temperatures, all curves have a gentle linear temperature dependence. However, at above the crossover temperatures, they rise sharply with different slopes. We call the crossover temperature of H_2O T_L , and that of protein or DNA T_C , with both values at approximately 222 ± 2 K. This is to say that the dynamic crossover phenomenon of both protein and DNA and that of their hydration water are highly correlated, and occur at a similar temperature. It is more striking to note that the T_L of H_2O hydrated in protein and that in DNA are close to each other. These results signal our later conjecture that the dynamic crossover temperature is independent of the biomolecules. To define precisely the T_L , we performed dynamic

measurements at HFBS. In Fig. 2, we present the temperature dependence of the average translational relaxation time, $\langle \tau_T \rangle$, for the hydrogen atom in a water molecule, calculated by RCM, for both protein and DNA cases [8-9]. Both H_2O and D_2O hydrated samples were measured. The contribution of scattering from biomolecules is subtracted out during the signal processing by taking the difference of the signals between the two samples. It is seen that, in the temperature range from 270 K to 230 K, $\langle \tau_T \rangle$ obeys VFT law, a signature of fragile liquid, quite closely. But at $T_L = 222 \pm 2$ K it suddenly switches to an Arrhenius law, a signature of a strong liquid. So we have a clear evidence of FSC in a cusp form. It is to be noted that the crossover temperature of protein hydration water is sharply defined at $T_L = 220$ K, the T_0 for the fragile liquid turns out to be 176 K, and the activation energy for the strong liquid, $E_A = 13.1$ kJ/mol, which are slightly lower than in the DNA case, $T_L = 222$ K, $T_0 = 186$ K, and $E_A = 14.6$ kJ/mol.

In summary, an investigation of the average translational relaxation time, of protein and DNA hydration water as a function of temperature reveals a hitherto unnoticed Fragile-to-Strong dynamic crossover at $T_L = 222 \pm 2$ K, close to the universal dynamic transition temperature T_C documented for biomolecules in the literature. The coincidence of the dynamic transition temperature T_C of biomolecules, signaling the onset of anharmonic molecular motion, and the FSC temperature T_L of the hydration water suggests that the change of mobility of the hydration water molecules across T_L drives the dynamic transition in biomolecules.

REFERENCES

- [1] S.-H. Chen, C. Liao, F. Sciortino, P. Gallo, P. Tartaglia, Phys. Rev. E **59**, 6708 (1999).
- [2] C.A. Angell, J. Non-Crys. Sol. **131-133**, 13 (1991).
- [3] B.F. Rasmussen, A.M. Stock, D. Ringe, G.A. Petsko, Nature **357**, 423 (1992).
- [4] W. Doster, S. Cusack, W. Petry, Nature **337**, 754 (1989).
- [5] W. Doster, S. Cusack, W. Petry, Phys. Rev. Lett. **65**, 1080 (1990).
- [6] M. Tarek, D.J. Tobias, Phys. Rev. Lett. **88**, 138101 (2002).
- [7] D. Vitkup, D. Ringe, G.A. Petsko, M. Karplus, Nat. Struct. Biol. **7**, 34 (2000).
- [8] S.-H. Chen, L. Liu, X. Chu, Y. Zhang, E. Fratini, P. Baglioni, A. Faraone, E. Mamontov, submitted to Phys. Rev. Lett. (2006).
- [9] S.-H. Chen, L. Liu, E. Fratini, P. Baglioni, A. Faraone, E. Mamontov, to appear in Proc. Nat. Acad. Sci. USA (2006).

The Dynamic Transition in RNA is Solvent-Induced



Much as glasses 'melt' when heated through a glass transition, all hydrated proteins undergo an analogous 'dynamic transition' in the temperature range of $T_D \approx 200$ K to 230 K, in which there is a distinct onset of increased motion within these large molecules. An intriguing aspect of this transition is that it correlates well with the appearance of measurable biochemical activity in proteins [1-2]. Much evidence exists, both experimental and computational, that supports the idea that solvent dynamics controls the observed dynamic transition [3-4]. A contrasting view is that the transition is an inherent property of proteins themselves, and arises from components such as the methyl groups on the side chains [5]. To assess if a universal mechanism drives the dynamical transition in biomolecules we studied the dynamics of tRNA using neutron scattering spectroscopy. Despite vast differences in the architecture and backbone structure of proteins and RNA, hydrated tRNA undergoes the dynamic transition at the same temperature as hydrated lysozyme, a common protein found in egg-white. This similarity supports the idea that the dynamic transition is solvent induced. Our results also suggest that methyl groups are not the main contributor to the dynamic transition in biological macromolecules; however, they may explain strong differences in the dynamics of tRNA and lysozyme observed at low temperatures.

Neutron scattering probes molecular dynamics directly and the observable time scales cover the range of internal motions occurring in proteins. Incoherent neutron scattering probes the dynamics of H atoms because their scattering cross-section is significantly larger than that of any other atom. H atoms are distributed throughout tRNA and lysozyme, providing information on their overall motions. Measurements were performed on the High Flux Backscattering Spectrometer (HFBS) at the NCNR. Elastic scans were measured at a heating/cooling rate of 0.7 K/min and quasielastic scattering measurements were taken using an energy window of ± 17 μ eV (with a resolution of 0.85 μ eV).

lysozyme shows an onset of anharmonicity with a stronger temperature dependence at $T \approx 100$ K. In Fig. 2 the resulting quasielastic spectra shows significant broadening relative to the instrumental resolution at 300 K for both hydrated tRNA and lysozyme. This indicates a relaxation process occurring in the 300 ps to 5 ns timescale. Hydrated tRNA at 200 K and dry tRNA at 300 K show no broadening, consistent with the harmonic behavior observed in $\langle u^2 \rangle$. In contrast, the spectra of dry lysozyme at 320 K and wet lysozyme at 200 K show quasielastic broadening, indicating a relaxation process occurring at temperatures below the dynamic transition, in agreement with the anharmonicity observed in $\langle u^2 \rangle$, and which is absent in tRNA.

G. Caliskan^{1,2}
R.M. Briber³
D. Thirumalai³
V. Garcia Sakai^{2,3}
S.A. Woodson¹
A.P. Sokolov⁴

¹ Johns Hopkins University
Baltimore, MD 21218

² NIST Center for Neutron Research
National Institute of Standards and Technology
Gaithersburg, MD 20899-8562

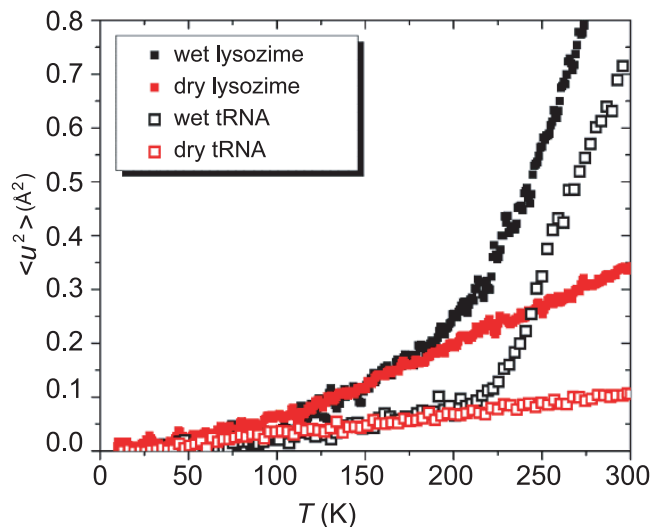
³ University of Maryland
College Park, MD 20472

⁴ University of Akron
Akron, OH 44325

Figure 1 shows the mean square hydrogen displacement $\langle u^2 \rangle$ of tRNA and lysozyme in dry and hydrated states, obtained from analyzing the elastic scattering intensity as a function of the scattering wavevector. In both hydrated samples, $\langle u^2 \rangle$ increases sharply above $T \approx 200$ K to 220 K, characteristic of the dynamic transition. Dry tRNA exhibits a linear increase in $\langle u^2 \rangle$ over the entire temperature range, a signature of harmonic behavior. In contrast, dry

FIGURE 1:

Mean-squared hydrogen displacement as a function of temperature for lysozyme (solid symbols) and tRNA (open symbols) in hydrated (black) and dry (red) forms. Error-bars are smaller than ± 0.02 \AA^2 .



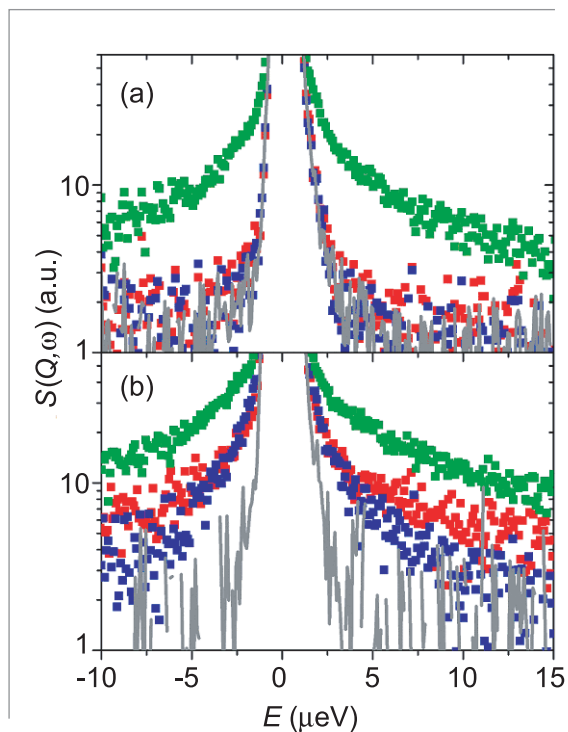


FIGURE 2:

Quasi-elastic scattering spectra of wet tRNA at 300 K (green) and 200 K (blue) and dry tRNA at 300 K (red) (a). Similar data for wet lysozyme at 295 K (green) and 200 K (blue) and dry lysozyme at 320 K (red) (b). The solid gray lines represent the resolution.

The similarity in T_D of hydrated tRNA and lysozyme indicates that the dynamic transition is not an intrinsic property of the macromolecule. Extensive measurements on various hydrated proteins, DNA and now tRNA, reveal the dynamic transition in the same temperature range, despite differences in backbone chemistry and 3D structure. It has been argued that the dynamic transition of hydrated biomolecules is primarily a result of the transition from liquid-like to solid-like dynamics that occurs in water on molecular time and length scales. The dynamic crossover for water occurs at $T_C \approx 220$ K to 230 K.

Further evidence for a solvent induced transition is the observation that the dynamic transition of lysozyme in glycerol [3] occurs at the same temperature as the dynamic crossover of pure glycerol. Furthermore, simulations have shown that when the translational motion of water is artificially restricted, the protein behaves as if it were below the dynamic transition even at 300 K [6]. This suggests that arrest of the translational motion of the solvent molecules blocks the motion of the biomolecule.

Based on the similarity of the temperature dependence of $\langle u^2 \rangle$ and NMR-determined orientational order parameter for methyl-bearing side chains, it has been proposed [5] that the freezing of rotational relaxation is the cause of the dynamic transition in proteins. However, the paucity of methyl groups in

tRNA suggests that the freezing of their rotational motion is unlikely to be the cause of the dynamic transition. Instead, the dynamic transition is related to another relaxation process that enters the energy window of the backscattering spectrometer at temperatures above T_D and appears as a significant broadening of the scattering spectra in the hydrated biomolecules [Fig. 2]. The microscopic nature of this process is unknown for proteins or for DNA. One suggestion based on MD-simulations is that the α -helices in myoglobin become dynamically active above T_D . If this is correct, this type of motion would require translational motion of water molecules.

The most significant difference between the dynamics of tRNA and lysozyme is the absence of anharmonicity in tRNA at low temperatures. An additional relaxation process occurs in lysozyme. It has been ascribed to methyl group dynamics that contribute significantly to the scattering spectra. This is consistent with our results for tRNA which lacks this relaxation component at low temperatures. However, these differences could also be due to the different flexibility of the polypeptide and polynucleotide backbones.

The present analysis clearly demonstrates that neither the 3D structure of biological macromolecules nor their chemical backbone affect the dynamic transition. This conclusion supports the idea [6] that unfreezing the translation of solvent molecules is the main cause of the dynamic transition in biomolecules. Our results also suggest that the rotation of methyl groups is not the main cause of the dynamic transition, although they may cause the low-temperature anharmonicity observed in proteins. Understanding the microscopic nature of the motions that activate in the nanosecond-picosecond time range in biological macromolecules above T_D remains an important challenge as these motions are intrinsically linked to biochemical interactions.

REFERENCES

- [1] B.F. Rasmussen, A.M. Stock, D. Ringe, G.A. Petsko, *Nature* **357**, 423 (1992).
- [2] H. Lichtenegger, W. Doster, T. Kleinert, A. Birk, B. Sepiol, G. Vogl, *Biophys. J.* **76**, 414 (1999).
- [3] A.M. Tsai, D.A. Neumann, L.N. Bell, *Biophys. J.* **79**, 2728 (2000).
- [4] A.L. Tournier, J. Xu, J.C. Smith, *Biophys. J.* **85**, 1871 (2003).
- [5] A.L. Lee, J. Wand, *Nature* **411**, 501 (2001).
- [6] M. Tarek, D.J. Tobias, *Phys. Rev. Lett.* **88**, 138101 (2002).
- [7] L. Cordone, M. Ferrand, E. Vitrano, G. Zaccai, *Biophys. J.* **76**, 1043 (1999).

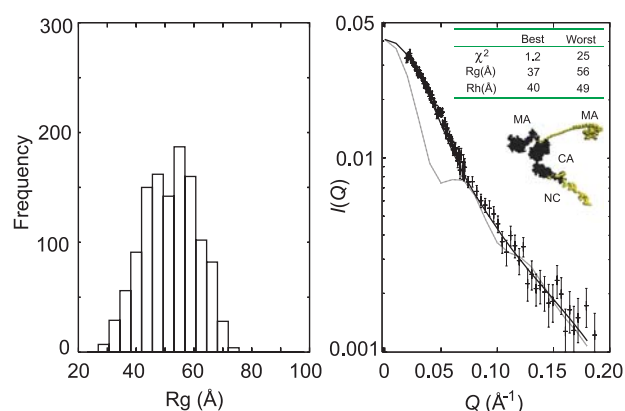
Studying Intrinsically Disordered Proteins by Small-Angle Neutron Scattering



A suite of computational methods is being developed with the double aim of aiding the analysis of small angle (neutron: SANS, x-ray: SAXS) scattering data from measurements on macromolecular systems and aiding in the design of subsequent experiments. Specifically, we are merging methods developed to search conformational space of small molecular pharmaceuticals with the conformational search problem posed by intrinsically disordered proteins and nucleic acids. This is achieved by generating an ensemble of macromolecular structures that have small angle scattering patterns that are consistent with experiment by varying sets of backbone dihedral angles and using importance sampling and linear algebraic methods. These algorithms have been incorporated into a graphical user interface called SASSIE intended for the NCNR user community.

FIGURE 1:

Analysis of an ensemble of protein structures of the full-length HIV-1 Gag protein by comparison of calculated patterns with experimentally determined small-angle neutron scattering data. Histogram of Rg values (left panel) and a comparison of experimental and theoretical SANS patterns of HIV-1 Gag protein (right panel). The experimental data are shown as points with error bars, while the best (black) and worst fit (grey) are shown as lines. The generation and evaluation of millions of Gag-1 structures indicates that monomeric HIV-1 Gag protein is folded over and not extended under physiological conditions. This implies that the protein undergoes a major conformational change when assembled into the intact virus particle.



J.E. Curtis¹
N.F. Berk¹
S. Krueger¹
P. Coleman²
S.J. Moeller²
R.B. Ross²
S. Datta³
A. Rein³

¹ NIST Center for Neutron Research
National Institute of Standards and Technology
Gaithersburg, MD
20899-8562

² 3M Corporate Research
Laboratory, USA
3M Center
St. Paul, MN
55144-1000

³ National Cancer Institute, NCI-Frederick
Frederick, MD
21702-1201

We have used these tools to predict the first full-length structures of the HIV-1 Gag protein [1]. This macromolecule is the major structural protein element in the virus that causes AIDS. The knowledge of the structure of this protein may allow for the development of drugs that prevent the assembly of virus particles *in vivo*. Additionally, we have determined structures of full-length Protein A, which is the major reagent used to purify antibodies by the pharmaceutical industry. Knowledge of the structures that Protein A adopts at thermal equilibrium may help to improve product yields. These tools, once mature, may be useful in the study of many intrinsically disordered proteins and the elucidation of macromolecular interactions in solution.

Proteins are vital components of biological systems that have a variety of structural and catalytic functional roles. Historically, atomic level structural knowledge of proteins has relied upon x-ray diffraction and nuclear magnetic resonance (NMR) spectroscopy. These methods have had an immeasurable impact on the elucidation of many biological problems. Recently, however, it has been estimated that $\approx 20\%$ to 30% of the proteins encoded by the eukaryotic genome have regions that are structurally ill-defined and thus many proteins are intrinsically dis-

ordered [2]. These disordered proteins have biological function and control mechanisms that are largely unclassified. Thus, a less realized role of proteins in many biological processes has emerged. Many disordered proteins have functionality that is directly related to their flexibility. Due to their inherent disorder, atomic descriptions are not generally available for the entire molecule since the molecules occupy an ensemble of interchanging conformations in solution.

Structural data for several regions of the HIV-1 Gag protein have been determined by x-ray and NMR methods. However, the determination of a full-length structure from either protein crystals or solution has not been achieved. The five major regions of the HIV-1 Gag protein are connected by amino acid residues that have been determined by experiment to

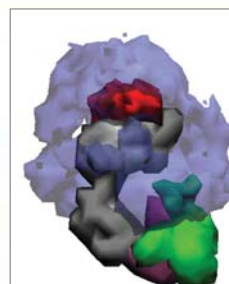
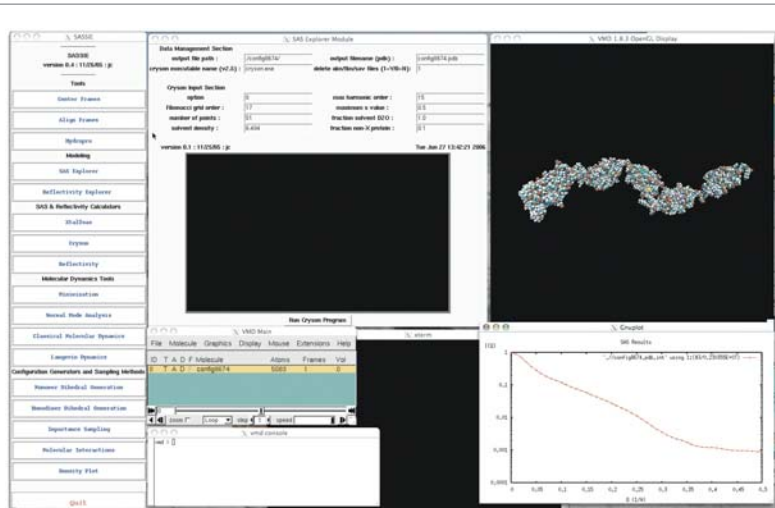


FIGURE 2:

Probability density plot depicting allowed structural arrangements of the individual sub-domains of the HIV-1 Gag protein. The regions are colored as follows: matrix, transparent blue; amino-terminal linker, red; capsid, grey; p2-linker, mauve; nucleocapsid, green.

FIGURE 3:

An example of the SASSIE software environment applied to the calculation of the SANS patterns from the atomic coordinates of a single configuration of protein-A. The interface allows for real-time calculation of SAS and reflectivity profiles of molecular objects as well as methods to generate and analyze ensembles of intrinsically disordered proteins and nucleic acids.



be highly flexible. Despite a large experimental effort to find a single structure, this flexibility suggests that given the disordered nature of the HIV-1 Gag protein, its non-aggregated state is characterized by an ensemble of structures. We have used the 30 m SANS instrument on the NG-3 beamline at the NCNR to determine the structural characteristics of the HIV-1 Gag protein in the monomeric state under physiological conditions. Using atomic positions available from experiment as a starting point, we have developed molecular models of the full-length HIV-1 Gag protein to create large ensembles of structures for analysis. While not rigorously exhaustive, the generation of millions of structures by varying the protein backbone dihedral angles is reasonably tractable using modest computational resources.

In Fig. 1 we compare the experimentally determined SANS patterns of monomeric HIV-1 Gag protein to a few theoretically determined curves from full-length atomistic models of the protein. Clearly, in all cases, extended structures have SANS patterns that deviate significantly from the experimentally determined data. Thus, in the case of the search for a single representative structure of the protein, extended structures do not have SANS patterns consistent with experiment.

In Fig. 2 we show a probability density plot of various regions of the HIV-1 Gag protein. The density plot was created using a Metropolis importance sampling method to determine representative linear combinations of structures that are consistent with the experimental data. As before, the most likely conformations are those that are folded over and not extended. Thus, one advantage of these methods is that they are useful in ruling out candidate structures that do not significantly contribute to the observed patterns.

In the native assembled HIV-1 virus particle the Gag protein is oligomerized to form the outer shell of the virus. The individual Gag protein molecules have been shown to align in extended conformation that is ordered with other Gag protein molecules to form the concentric shell of the virus. Thus the HIV-1 Gag

protein must undergo a major conformational change upon virus assembly. A detailed analysis of the microscopic interactions that are involved in this oligomerization process from the disordered/folded-over state may potentially lead to the development of therapeutic molecules to disrupt this process that may have value in the treatment of AIDS.

We have condensed the modeling, structure generation, and analysis algorithms into a graphical user interface called SASSIE. In addition to the analysis of structurally disordered proteins, the analysis package allows for the calculation of SAS (SAXS/SANS) and reflectivity profiles in real-time as the user manipulates the molecule(s) on the display. For example, in Fig. 3, we show the calculation of the SANS patterns of a single conformation of the Protein A described above.

In summary, we have developed methods and user-friendly graphical software to aid in the design and analysis of SANS experiments of disordered molecules. We have applied these methods to study the conformation of several proteins [1,3]. While the individual structural or ensemble solutions may not be unique, we have found that there is utility in knowing both what types of structures do and do not significantly contribute to a particular patterns. This knowledge allows for a more systematic analysis of both single and ensemble conformation structures that can exist in solution. Therefore, these methods will have important applications in the use of SANS to study the structure and function of disordered proteins.

REFERENCES

- [1] S.A.K. Datta, J.E. Curtis, W. Ratcliff, P.K. Clark, R.M. Crist, J. Lebowitz, S. Krueger, and A. Rein, *J. Mol. Biol.* (submitted).
- [2] C.J. Oldfield, Y. Cheng, M.S. Cortese, C.J. Brown, V.N. Uversky, and A.K. Dunker, *Biochemistry* **44**, 1989-2000 (2005).
- [3] D. Lee, *et al.*, *Mol. Cell* **22**, 423-430 (2006), D. Lee, *et al.*, *Mol. Cell* (in preparation).

Micro-organization of lipids and cholesterol in cellular lipid membranes is thought to be an essential regulatory mechanism important for cell survival [1]. Improper distribution and organization of the various lipids and cholesterol in mammalian cell membranes can profoundly affect the initiation and progression of disease [2]. The organization of the hydrocarbon core of lipid bilayers, such as the chain ordering and orientation, is still rather unclear due to the lack of experimental quantitative data. The time and ensemble average of lipid terminal methyl groups in lipid bilayers is a key to answering many questions regarding the organization and motion of the acyl chains.

Recent molecular dynamics simulation results [3], as well as nuclear magnetic resonance studies [4-6], suggest that some acyl chains undergo extreme bending motions, which bring the methyls close to the bilayer polar interface. The simulations were aimed at reproducing the complete structure of the DOPC (dioleoylphosphatidylcholine) bilayer reported by Wiener and White [7]. Excellent agreement was found between the simulated and experimental results for the transbilayer positions and widths of the carbonyl, glycerol, phosphate, and choline groups, but the results for the water and the double-bonds showed significant discrepancies with respect to the experiment. These differences, however, were not as dramatic as those observed between the simulated and experimental terminal methyl group width. A much wider terminal methyl distribution was predicted by the simulation (Fig. 1).

Because of the much higher coherent scattering length of deuterium (^2H) compared with hydrogen, the d6-DOPC allowed direct determination of the mean transbilayer position and distribution of the label. This was accomplished through a direct comparison of the profiles obtained for d6-DOPC bilayers with those obtained for the hydrogenous form. A similar approach was used to determine the transbilayer distribution of the waters of hydration, except H_2O and $^2\text{H}_2\text{O}$ were used. The water distribution shows the extent of water penetration into the polar regions of the bilayer. As shown in Fig. 2, while the water distribution can be described by a Gaussian, the methyl distribution is characterized by a central Gaussian-shaped part accompanied by long tails that extend into the polar interface. The area under these tails accounts for $\approx 20\%$ of the total area under the total methyl profile.

These experimental results are broadly consistent with the prediction of the MD simulation [3]. An analysis of the simulation trajectories of the terminal methyl groups shows that about 30% of the methyl groups eventually visit the polar membrane interface. Most visit the interface for 5 ns or so, but a small percentage stay much longer, 20 ns to 50 ns. We conclude that, though the hydrocarbon core of a lipid bilayer is organized into distinct domains, the acyl

M. Mibaitescu¹
 F. Castro-Roman¹
 R. Chamberlin¹
 D.L. Worcester²
 D.J. Tobias¹
 S.H. White¹

¹ University of California at Irvine
 Irvine, CA 92697

² University of Missouri at Columbia
 Columbia, MO 65211

Neutron diffraction and specific molecular deuteration were therefore employed in this work to determine the methyl group distribution directly. All the neutron diffraction experiments were performed at the Advanced Neutron Diffractometer/Reflectometer (AND/R) [8] located at the NCNR. High-purity terminal-methyl deuterated oleic acid was synthesized and in turn was used to synthesize DOPC with deuterated terminal methyl groups (d6-DOPC).

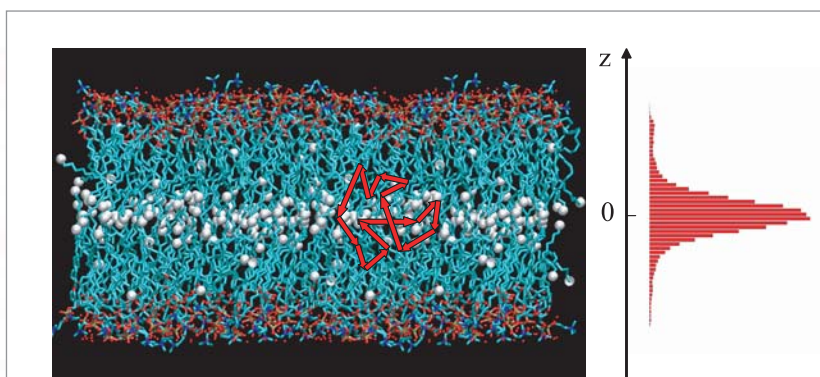


FIGURE 1: Molecular dynamics simulation of a DOPC bilayer. CHARMM [11] force fields were used to simulate a bilayer constituted of dioleoylphosphatidylcholine (DOPC) lipids hydrated with 5.4 waters/lipid (66% relative humidity). The terminal methyl groups are shown as white beads. The density distribution of the terminal methyl groups resulting from the simulation is shown in the bar graph on the right.

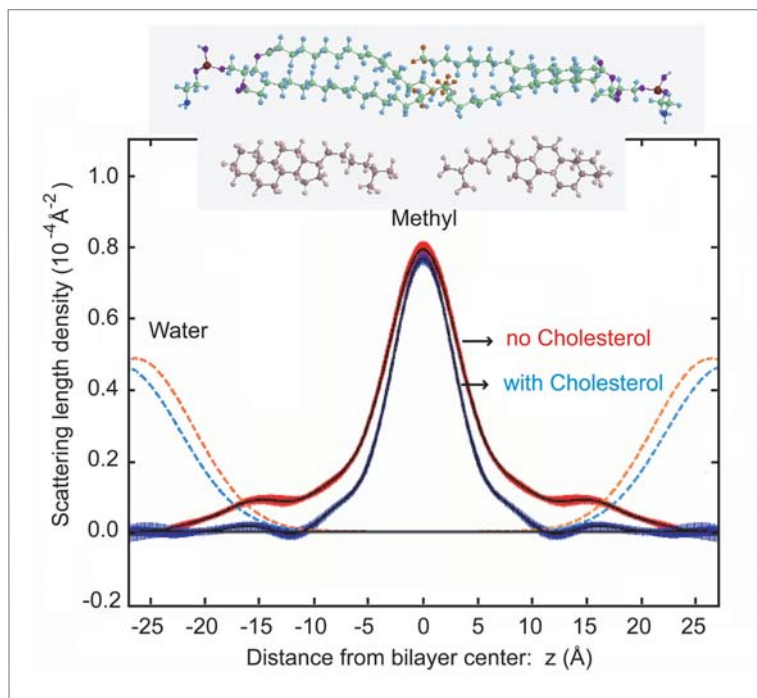


FIGURE 2:

Cholesterol effect on the chain order. The terminal methyl distribution in a pure DOPC bilayer (red) and a DOPC bilayer containing 33 % Cholesterol (blue), respectively, measured at 86 % relative humidity. The blue and orange dotted curves represent the water distributions with and without cholesterol, respectively. The top inset illustrates the general arrangement of two opposing DOPC lipids in a bilayer with the terminal methyls shown as orange beads. Cholesterol molecules (lower images) insert into each leaflet of the bilayer with their steroid ring part toward the water interface.

chain ends visit the water interface surprisingly often due to molecular disorder. One can speculate that this extreme form of disorder could be detrimental to membrane protein function. Many proteins involved in signaling, for example, apparently prefer to associate with ordered cholesterol-rich domains [9]. Cholesterol, acting as an important regulator of lipid bilayer organization may create optimal conditions for fast dynamical interactions of membrane receptors with their ligands during signaling.

How does cholesterol affect the terminal-methyl distribution? To answer this question, the experiment of Fig. 1 was repeated with cholesterol in the DOPC bilayer. Figure 2 reveals that cholesterol causes a general retraction of the chain ends, because cholesterol restricts the motion of the chains due to the rigidity of its steroid moiety. The retraction of the chain ends to the center of the bilayer in the presence of cholesterol is a dramatic demonstration of the ordering and stabilizing role of cholesterol in lipid bilayers. The results demonstrate unambiguously that, without the ordering effect of cholesterol, the terminal methyl groups can explore the space over the entire hydrocarbon region, and parts of the headgroup region. These are unprecedented direct experimental observations, which were stimulated by recent progress in neutron diffraction instrumentation for biological systems [8], molecular dynamics simulation procedures [3], and methods for molecular deuterium labelling [10].

ACKNOWLEDGMENTS

This study was carried out as part of the *Cold Neutrons for Biology and Technology* project supported by the NIH National Center for Research Resources (RR14812) and The Regents of the University of California. Additional support was provided by a grant from the National Institute of General Medical Sciences (GM68002).

REFERENCES

- [1] K. Simons, and E. Ikonen, *Nature* **387**, 569 (1997).
- [2] F.R. Maxfield, and I. Tabas, *Nature* **438**, 612 (2005).
- [3] R.W. Benz, F. Castro-Roman, D.J. Tobias, and S.H. White, *Biophys. J.* **88**, 805 (2005).
- [4] Z.-C. Xu, and S. Cafiso, *Biophys. J.* **49**, 779 (1986).
- [5] P.E. Godici, and F.R. Landsberger, *Biochemistry* **13**, 362 (1974).
- [6] D. Huster, and K.J. Gawrisch, *J. Am. Chem. Soc.* **121**, 1992 (1999).
- [7] M.C. Wiener, and S.H. White, *Biophys. J.* **61**, 434 (1992).
- [8] <http://www.ncnr.nist.gov/programs/reflect/ANDR>
- [9] L. Finegold, Ed., *Cholesterol in Membrane Models*, CRC Press, Boca Raton, FL (1993).
- [10] R. Chamberlin, *et al.*, unpublished.
- [11] S.E. Feller, *et al.*, *Biophys. J.* **73**, 2269 (1997).

Changes of Diphtheria Toxin Bound to Lipid Membranes

In order to control bacterial toxins, it is important to understand how they invade cells. The bacterial toxins diphtheria, tetanus, and botulinum invade cells through a process of high affinity binding, internalization via formation of a membrane-bound compartment within a cell (an endosome), and subsequent membrane penetration of the catalytic domain activated by a pH drop in the endosome [1,2]. Each of these toxins is composed of three domains: a binding domain, a translocation domain, and an enzyme or catalytic domain. The process of enzyme translocation across the membrane is not well understood with regard to the detailed conformational changes that occur at each step and whether the proteins act alone or as oligomers. A detailed understanding of the mechanism of enzyme translocation may enable means of inhibiting the harmful effects of these toxins. A particularly important long-term goal is to mitigate the lethality of botulinum neurotoxin, which is a potential terrorist or biowarfare agent. While botulinum, tetanus, and diphtheria are extremely potent toxins, they also have tremendous potential utility in medicine [1, 3]. Further development of new therapies and cancer treatments based on the re-engineering of the toxins will benefit greatly from a full understanding of the enzyme translocation mechanisms.

To begin to address these questions, we performed neutron reflectivity measurements for diphtheria toxin (DT) bound to Langmuir monolayers and to tethered lipid bilayers. We followed pH-dependent conformational changes of the toxin for several bulk DT concentrations. First we examined the structure of DT (CRM197, a nontoxic mutant) adsorbed to Langmuir monolayers of dipalmitoylphosphatidylglycerol (DPPG) at different bulk concentrations. Reflectivity data are shown in Fig. 1 for a DT concentration of 0.93 μM . In these measurements the lipids and the proteins were protonated and the subphase was a phosphate buffer solution in H_2O .

The measurements revealed pH ranges over which large conformational changes occurred as well as pH ranges over which little or no observable change occurred. The main stages of conformational change are shown in Fig. 1. The detailed structure of the adsorbed layer at each state will be unambiguously determined only when data for another contrast is obtained (d-lipids), and so the profiles in Fig. 1b should not be considered unique. However the qualitative trends are clearly evident in the data. While no adsorption could be detected at pH 7.6, strong adsorption occurred at pH 6.5, where the data are consistent with one principle layer of ≈ 80 Å. Adsorption continued to increase to pH 6.3, but with little change in the profile shape (not shown). Below pH 6.3, the adsorbed amount is nearly constant, and the changes in the reflectivity data indicate changes in conformation of the adsorbed protein. At pH 5.81 two layers are resolved. Some segments have penetrated into the lipid tails at this point. With a decrease in pH to 5.26 the layer adjacent to the lipid film became thinner and more concentrated in amino acids whereas the outer layer extended still further

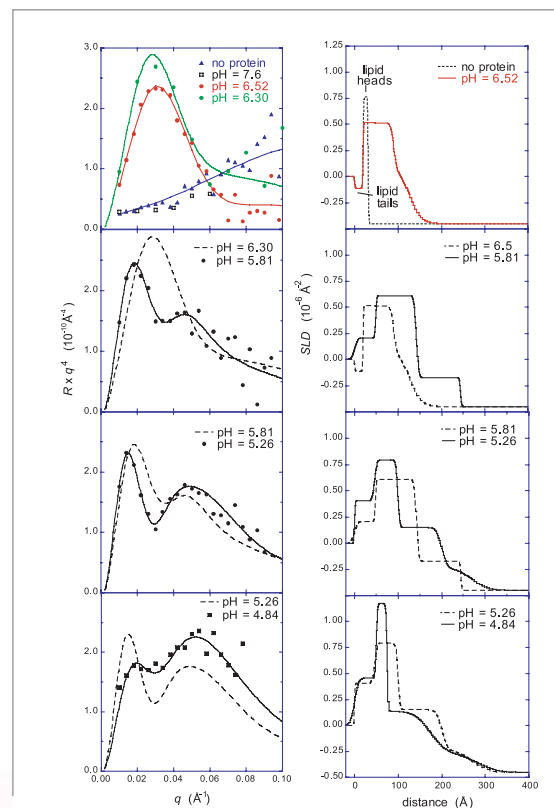


FIGURE 1: Reflectivity and fitted scattering length density (SLD) profiles for DT binding to Langmuir monolayers of DPPG at 0.93 μM .

into the subphase. Upon further decrease in pH to 4.84, the inner layer became even thinner and more concentrated. The outer layer appeared to contract somewhat, but this cannot be determined unambiguously from the present data alone. Overall, with decreasing pH it appears that one domain, presumably the translocation domain, collapses and inserts into the membrane, whereas a second domain, pre-

M.S. Kent¹
H. Yim¹
J.K. Murton¹
S. Satija²
C.F. Majkrzak²
D.J. McGillivray^{2,3}
M. Lösche^{2,3}

¹ Sandia National Laboratories
Albuquerque, NM
87185

² NIST Center for Neutron Research
National Institute of Standards and Technology
Gaithersburg, MD
20899-8562

³ Carnegie Mellon University
Pittsburgh, PA
15213

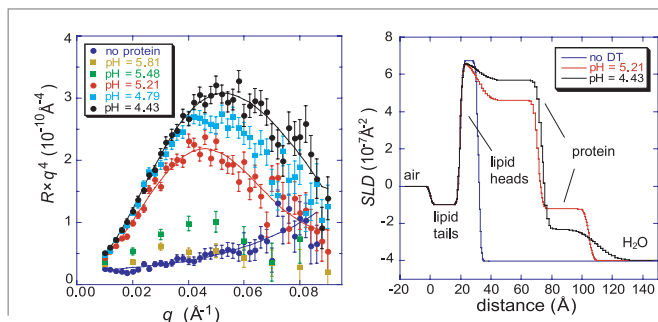


FIGURE 2: Reflectivity and fitted SLD profiles for DT binding to Langmuir monolayers of DPPG at 0.31 μM .

sumably the catalytic domain, extends or unfolds. Analogous data at a bulk DT concentration of 0.31 μM are shown in Fig. 2. These data show several important differences relative to the data at 0.93 μM . First, no significant adsorption occurs until pH 5.5. Second, upon initial adsorption the layer is much thinner ($\approx 50 \text{ \AA}$) than that at 0.93 μM . This may indicate adsorption of monomers at 0.31 μM and adsorption of dimers at 0.93 μM . The data fitting suggests two layers for the protein structure and little penetration of amino acids into the lipid film, but these details must be confirmed by acquiring data for a second contrast. Third, with decreasing pH the peak simply moves to slightly higher q . A second peak never appeared at lower q as was the case for 0.93 μM . At 0.31 μM the layer remains thin and simply becomes more concentrated, in contrast to the results for 0.93 mM.

and pH. Much more work is needed to sort out this complex behavior. However, the present data reveal several important features and suggest a number of interesting hypotheses to be tested in future work. First, distinctly different interfacial structures of DT resulted at different bulk protein concentrations. This suggests that oligomerization of DT may impact the translocation process. Second, at 0.93 μM several distinct layers could be resolved within the adsorbed protein structure, with a large expansion of the outer layer and strong insertion of the inner layer occurring with decreasing pH. The large expansion may indicate unfolding of one of the domains, presumably the catalytic domain. Finally, at the lipid monolayer and bilayer membranes under the same conditions of concentration and pH, different adsorbed layer structures resulted. This could be due to the use of gel versus fluid phase lipids, the constraint of constant area in the bilayer case versus constant pressure in the monolayer work, or the obvious structural difference in one versus two leaflets.

A series of measurements was performed for DT binding to tethered bilayers of dimyristoylphosphatidylglycerol (DMPG) from a 0.31 μM solution in D_2O phosphate buffer. The bilayers were tethered onto gold-coated wafers using the solvent exchange method [4]. The tethering molecule and tethering protocol were supplied by the Cold Neutrons for Biology and Technology group [4]. Some data for this series are shown in Fig. 3. Data were obtained to $q_z = 0.3 \text{ \AA}^{-1}$, but only the lower q_z range where the effect of the protein is most prominent is shown in Fig. 3. No adsorption occurred until pH = 5.6, at which point two layers are required to fit the data. With decreasing pH the layer expanded substantially, and three layers are required to fit the data at pH 5.2 and below. The strong expansion with decreasing pH is similar to the results observed for binding to Langmuir monolayers of DPPG at 0.93 μM and in contrast to the results for binding to DPPG at 0.31 μM . Strong insertion into the bilayer did not occur, as indicated by the low SLD of the lipid tail region throughout the series. However, the fitting suggests a small perturbation of the inner leaflet, which could indicate helices lying parallel to the headgroups in that layer. Such a result would be consistent with a structure proposed previously [5].

Sandia is a multiprogram laboratory operated by Sandia Corporation, a Lockheed Martin Company, for the United States Department of Energy under contract DE-AC04-94AL85000.

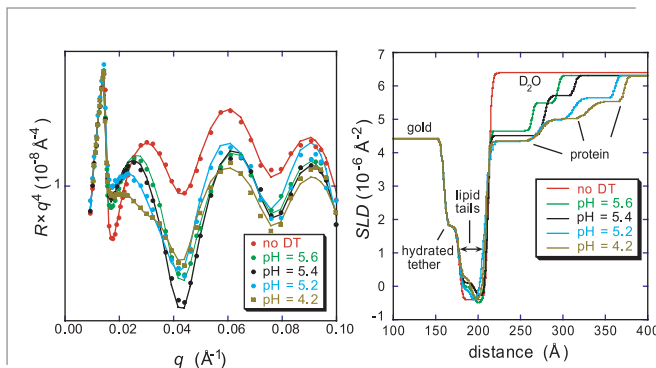


FIGURE 3: Reflectivity and fitted SLD profiles for DT binding to tethered bilayers of DMPG at 0.31 μM .

In conclusion, this initial work has revealed a rich variety of structures for DT bound to monolayers and tethered bilayers as a function of bulk concentration

REFERENCES

- [1] A. Chenal, P. Nizard, and D. Gillet, *J. Toxicology Toxin Reviews* **21** 321 (2002).
- [2] G. Lalli, S. Bohnert, K. Deinhardt, C. Verastegui, and G. Schiavo, *Trends in Microbiology* **11** 431 (2003).
- [3] G. Schiavo, M. Matteoli, and C. Montecucco, *Physiological Reviews* **80**, 717 (2000).
- [4] G. Valincius, D.J. McGillivray, W. Febo-Ayala, D.J. Vanderah, J.J. Kasianowicz, M. Lösche, *J. Phys. Chem. B.* **110** 10213 (2006).
- [5] L. Senzel, M. Gordon, R.O. Blaustein, K.J. Oh, R.J. Collier, and A. Finkelstein, *J. Gen. Physiol.* **115** 421 (2000).

Functional Toxin Pores in Tethered Bilayers: Membrane Association of α -hemolysin

Several toxins form pores on the surface of susceptible cells that penetrate the membrane barrier. The pores allow unregulated ion diffusion across the membrane, leading to cell death (lysis). The protein α -hemolysin (α HL) is a toxin produced by the bacteria *Staphylococcus aureus* which is the subject of recent study, in particular because it shows promise for development as a stochastic biosensor for small ions [1], proteins [2], and large molecules, including DNA [3, 4]. Using a system that we previously designed and optimized, we have incorporated the protein into a robust biomimetic solid-tethered bilayer membrane (tBLM). Monitoring the incorporated pore's ion transport properties with electrical impedance spectroscopy, we verified that the toxin retains its natural functionality. This enabled the characterization of the interaction between the membrane and protein using neutron reflectometry (NR) at the Cold Neutrons for Biology and Technology's Advanced Neutron Reflectometer/Diffractometer (AND/R) [5].

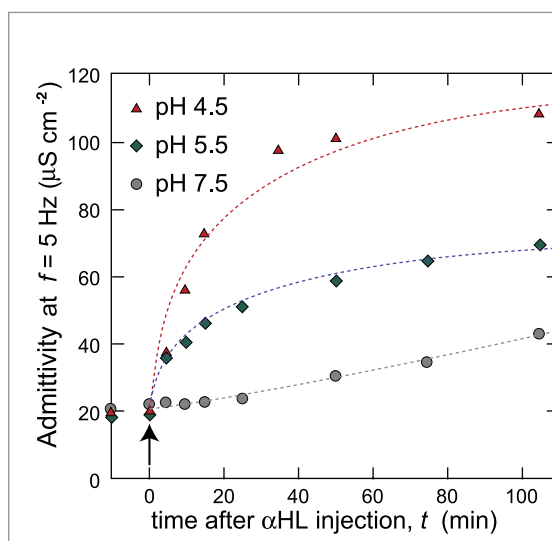


FIGURE 1: Change in tBLM-covered electrode admittance at $f = 5$ Hz, indicative of α HL incorporation, as a function of buffer pH.

The development of practical biosensors based on natural membrane proteins, such as α HL, is a subject of considerable effort. However, many problems must be overcome in the design of a system suitable for technical manipulation and measurement while preserving the biological activity of the protein. Natural cell membranes are intrinsically complex and disordered, a specific molecular architecture of lipids, sterols, proteins, glycolipids, etc., which drives the development of simpler model systems that are more amenable to preparation and characterization. Biosensors must also be robust, preferably reusable, and allow the behavior of the membrane-associated protein to be readily probed.

Using a common approach [6] we have addressed these issues in developing a solid-supported, tethered bilayer membrane (tBLM), which can be formed in a simple fashion on gold-covered surfaces, and which is surface-decoupled through a controllable hydrated polymer spacer [7]. The tBLMs were optimized for α HL incorporation using electroimpedance spectroscopy (EIS), a technique that is capable of rapidly probing the ion transport properties of the membrane pore. The increase in the tBLM admittance is a function of the number of active pores incorporated (Fig. 1).

The electrical parameters of the toxin in the tBLM can be compared with α HL in unsupported black lipid membranes, where they have been comprehensively studied [8]. Unfortunately, unsupported lipid membranes are limited for structural studies of the protein because of their limited size ($\approx 10^2$ mm²), and unsuitable for biosensor development as they are fragile, being sensitive to shock and vibration. However, the comparison of the effects of polymers on pore conductivity [8] and response to pH [9], confirms that the toxin has retained its functionality in the tBLM, with the implication that the protein has also retained its native structure.

Using the optimized conditions, incorporation of α HL into the biomimetic tBLM occurs at a surface coverage large enough that its effect is readily observable in the raw neutron reflectivity (Fig. 2). These effects can be fitted using a simple layer model, which accounts for the most prominent feature of the protein, its large cap domain exterior to the membrane. In order to obtain more information about the interactions between the protein and the tBLM it was assumed that the in the tBLM the α HL channel x-ray crystal structure is valid.

D.J. McGillivray^{1,2}
F. Heinrich^{1,2}
M. Lösche^{1,2}
I. Ignatjev³
G. Valincius³
D.J. Vanderab⁴
J.J. Kasianowicz⁵

¹ Carnegie Mellon University
Pittsburgh, PA 15213

² NIST Center for Neutron Research
National Institute of Standards and Technology
Gaithersburg, MD 20899-8562

³ Institute of Biochemistry and Vilnius Gedimino Technical University,
LT-2600, Vilnius Lithuania

⁴ Biochemical Sciences Laboratory
National Institute of Standards and Technology
Gaithersburg, MD 20899-8312

⁵ Electrical and Electronic Engineering Laboratory
National Institute of Standards and Technology
Gaithersburg, MD 20899-8110

The modeling of the NR shows that the protein spans the tBLM, with the stem penetrating $\approx 5 \text{ \AA}$ into the headgroup region on the inner leaflet (Fig. 3). The protein rim appears to interact strongly with the lipid headgroups, and even perturbs the hydrophobic tails, of the outer leaflet. This confirms the predictions of Song *et al.*, from analysis of the crystal structure that the cap region would be “probably in close proximity, if not in direct contact, with the membrane bilayer” [10]. The overhang between the membrane-penetrating stem domain and the rim domains is lined with basic and acidic residues, forming a suitable enclosure for the zwitterionic phospholipid headgroups, while the very edge of the rim contains a number of aromatic residues that can interact with the tail region of the lipid bilayer. The extension of the stem into the polar headgroup region on the far side of the membrane also stabilizes the band of charged residues that rings the bottom of the stem domain.

The NR modeling shows that the protein is incorporated into the bilayer at $\approx 36 \%$ of the estimated maximum possible packing density of the protein. This packing density, ≈ 1 channel per 310 nm^2 , is qualitatively similar to that observed in lysed cells [11]. The incorporation of such a large amount of the protein in the bilayer, without bilayer collapse, emphasizes the robustness of the solid-supported system.

The authors acknowledge useful discussions with Dr Hirsh Nanda. This work was supported by the NSF (grant nos. 0555201 and 0457148). ML and AND/R are supported, through the CNBT, by the NIH under grant no. 1 R01 RR14812 and by The Regents of the University of California. JJK is supported in part by the NIST Office of Law Enforcement Standards and a NIST Single Molecule Manipulation and Measurement Competence Award.

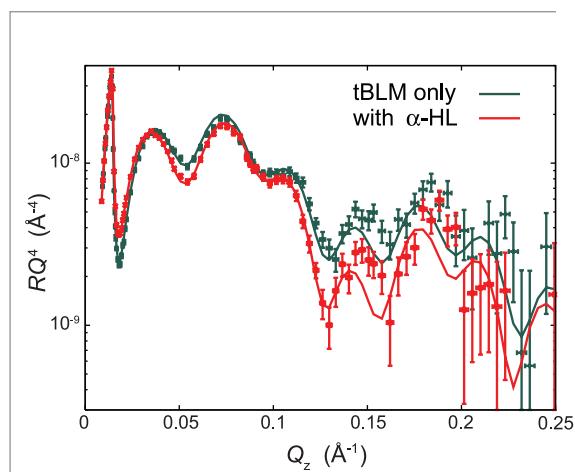


FIGURE 2:

NR and fitted models of the tBLM before and after α HL exposure, measured in D_2O . Fits were also constrained to other water contrasts (not shown).

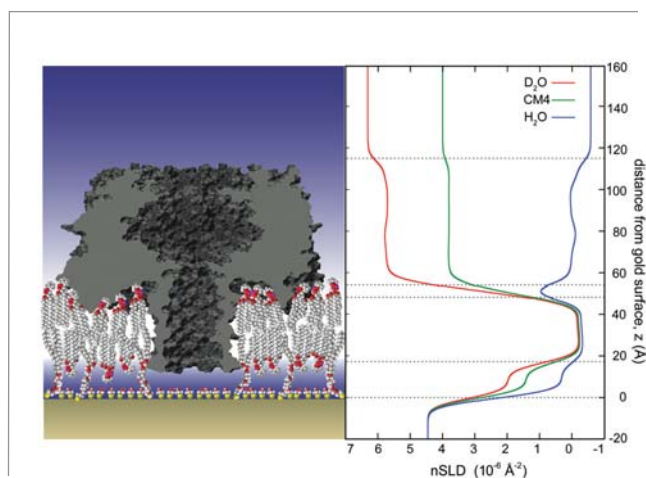


FIGURE 3:

(Left) A scaled cartoon of the functional α HL pore incorporated into a tBLM on gold, derived from the neutron scattering length density (nSLD) profile depicted on the right. (Right) The nSLD profile derived from simultaneous fitting of data measured in D_2O , H_2O and a $D_2O:H_2O$ mixture (CM4) using the x-ray crystal structure of the protein. The combination of EIS and neutron reflectometry on a robust tethered membrane system has enabled the combined study of the structure and the functionality of a toxin with potential biotechnology applications. The functionality of the membrane is preserved in the biomimetic environment, and the neutron reflectometry reveals that the x-ray crystal structure is well-preserved in the membrane-bound form of the protein. The scattering also reveals details of the intimate binding between the protein and the membrane, confirming predictions based on the toxin structure.

REFERENCES

- [1] S.M. Bezrukov, J.J. Kasianowicz, Phys. Rev. Lett. **70**, 2352 (1993).
- [2] J.J. Kasianowicz, S.E. Henrickson, H.H. Weetall, B. Robertson, Anal. Chem. **73**, 2268 (2001).
- [3] J.J. Kasianowicz, E. Brandin, D. Branton, D.W. Deamer, Proc. Natl. Acad. Sci. U.S.A. **93**, 13770 (1996).
- [4] J.J. Kasianowicz, Nat. Mater. **3**, 355 (2004).
- [5] J.A. Dura, D. Pierce, C.F. Majkrzak, N. Maliszewskij, D.J. McGillivray, M. Lösche, K.V. O'Donovan, M. Mihailescu, U.A. Perez-Salas, D.L. Worcester, S. White, Rev. Sci. Instr. (2006), in press.
- [6] B.A. Cornell, V.L.B. Braach-Maksytyis, L.G. King, P.D.J. Osman, B. Raguse, L. Wiczorek, R.J. Pace, Nature **387**, 580 (1997).
- [7] G. Valincius, D.J. McGillivray, W. Febo-Ayala, D.J. Vanderah, J.J. Kasianowicz, M. Lösche, J. Phys. Chem. B **110**, 10213 (2006).
- [8] S.M. Bezrukov, I. Vodyanoy, R.A. Brutyan, J.J. Kasianowicz, Macromolecules, **29**, 8517 (1996).
- [9] J.J. Kasianowicz, S.M. Bezrukov, Biophys. J. **69**, 94 (1995).
- [10] L.Z. Song, M.R. Hobaugh, C. Shustak, S. Cheley, H. Bayley, J.E. Gouaux, Science **274**, 1859 (1996).
- [11] S. Bhakdi, J. Tranumjensen, Microbiol. Rev. **55**, 733 (1991).

Modeling Neutron Measurements on Friction Stir Welded Steel

The accurate prediction of the macroscopic deformation response of a material, especially in complex loading conditions, requires the consideration of the underlying microstructural changes. Simulation of polycrystal material deformation based on deformation of the constituent crystallites holds the promise to do just that — and to predict a wide range of properties both on the continuum and crystal levels. For the latter, neutron diffraction has the ability to probe crystallite deformation selectively, and to track certain changes in the crystallite orientation distribution during deformation, thus making it an ideal tool for in-situ experiments. The results of such a simulation-experiment comparison, based on elastoviscoplastic polycrystal plasticity implemented in a finite element framework, and applied to the deformation of a friction stir welded stainless steel show good agreement with both macroscopic and neutron diffraction data.

Design of modern high performance engineering components requires increased understanding of material response to a variety of loading conditions. However deformation processing of polycrystalline materials alters their microstructure and thus leads to changes in their macroscopic properties. Therefore, to adequately predict the response of the material to any

loading condition, the ability to represent the microstructure of the modeled material is key. Multiscale models, such as polycrystal plasticity based models, possess the ability to do just that by modeling the response of the individual crystals and their interactions to accurately predict the macroscopic response. Moreover, they offer the rare possibility of direct comparison of simulated crystal deformation-derived quantities with those obtained by diffraction. The importance of this approach cannot be overstated because it offers the rare possibility of direct comparison of simulated crystal deformation-derived quantities with those obtained by diffraction.

Such an approach is especially suitable for configurations in which nonuniform initial microstructures cause strength gradients and nonuniform deformations under applied load. The stainless steel friction stir weld samples studied here are prime examples with relatively large-grained base material where the size distribution peaks at 20 μm , followed by a narrow heat affected zone (HAZ) and a fine-grained weld zone (grain size peak at 4 μm) (Fig. 1). Also, the crystallite orientation distribution (ODF) in the base and weld material are different, with the base

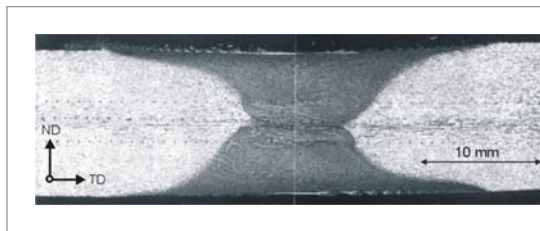


FIGURE 1:

Weld zone of an actual specimen [1]. The grain size in the weld zone (dark) is approximately 5 times smaller than in the base material (light). The heat affected zone is not visible but it extends about 1 mm away from the weld zone.

material having a weak rolling texture and the weld exhibiting a weak cube texture component.

The simulation methodology used here [1,2] accounts for the specimen heterogeneity in two ways: first, by assigning each finite element the orientation dependent elastic/plastic properties of a single

crystal, and second, by a similar finite element formulation for the continuum scale, for which the element properties are derived from the first formulation. This is done using a polycrystal average based on a Taylor-like linking assumption. Furthermore, the polycrystal average is not uniform but depends on the location in the specimen to account for macroscopic property gradients. Model initialization parameters include the initial local ODFs and location-dependent slip system hardness. The latter is chosen such that it accounts for grain size differences using a Hall-Petch relationship. By tracking certain finite elements with single crystal properties throughout the deformation, it is possible to derive certain quantities such as orientation dependent strain and change in orientation due to rotations. With respect to the neutron experiments, the first is compared to (hkl)-dependent lattice strains, the second to changes in peak intensities. The peak width — which is very sensitive to dislocation density and therefore plastic strain — was not used for comparison because it was strongly affected by instrumental parameters. The deconvolution of instrumental effects on peak broadening will be the subject of future work.

D.E. Boyce¹
P.R. Dawson¹
B. Stille¹
T. Gnäupel-Herold²
H.J. Prask²

¹ Cornell University
Ithaca, NY 14853

² NIST Center for
Neutron Research
National Institute of
Standards and
Technology
Gaithersburg, MD
20899-8562

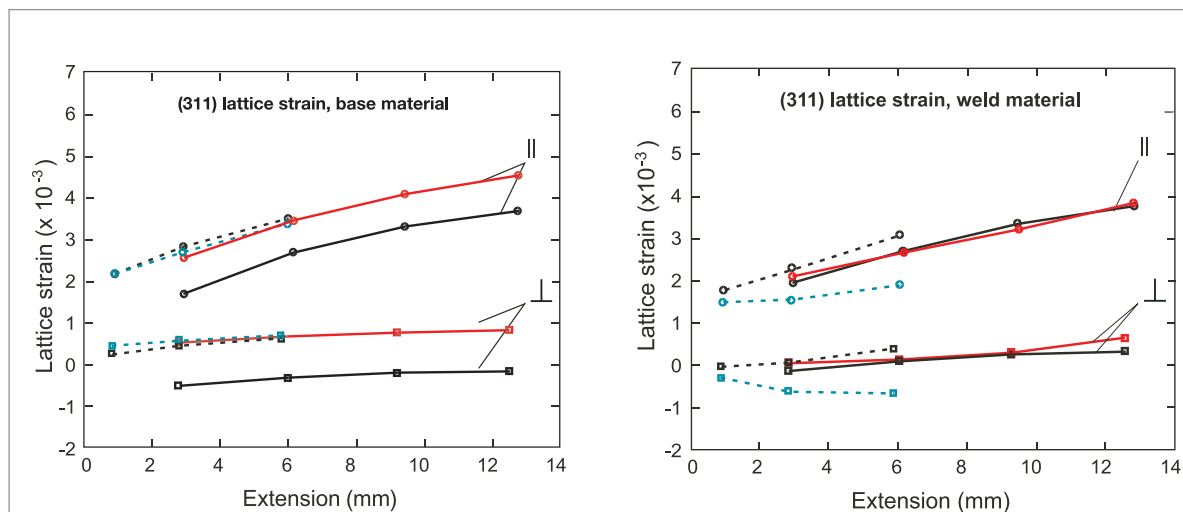


FIGURE 2: Lattice strain comparisons for base and weld material. Solid lines are Specimen A. Dashed lines are Specimen B. Black lines are experiment. Colored lines are simulation. The uncertainties are 1×10^{-4} . The symbols || and \perp denote the scattering vector parallel and perpendicular to the applied stress direction.

The diffraction experiments were conducted at the BT8 Residual Stress Diffractometer. Several specimen geometries with different gage section shapes were used. The specimens were deformed in the TD-direction using a screw-driven load frame with 3-4 unloading episodes up to the final extensions > 12 mm, equivalent to more than 20 % strain. Diffraction peaks were collected for the weld and the base separately using appropriate sampling volumes depending on the specimen dimensions. Results are presented for two geometries: specimen A with 6.70 mm (ND) \times 1.98 mm (RD) and specimen B with 3.94 mm (ND) \times 3.34 mm (RD).

The elastic strains for grains in certain orientations can be inferred directly from the change in the peak positions in the neutron data. The results of both measurement and simulation for weld and base material are shown in Fig. 2.

The overall agreement between simulation and experiment is very good; if there is a difference then it is by a constant offset, which is most likely due to the reference d-spacing chosen to calculate the experimental lattice strains from the d-spacings. The results shown here along with results for other reflections [3] indicate that the change in slip system hardness is predicted correctly. Further evidence for the performance of the simulation is found in the good estimate of the overall hardening as seen in Fig. 3. This graph compares the experimental and predicted extension for a given applied force (at the start of an unloading episode), showing very good agreement overall.

The multiscale methodology used here for simulation performed well on the microscopic and on the macroscopic scale. It represents one of the

rare attempts to reconcile microscopic and macro-scale behavior in deformation and, as such, illustrates very well the complexity necessary for the success of such a model. As a payoff, the model is able to predict many parameters that were equally well matched by experimental results, such as specimen shape after deformation, crystallite orientation distribution function, and slip system strength. (For a full account, see Ref. 3.)

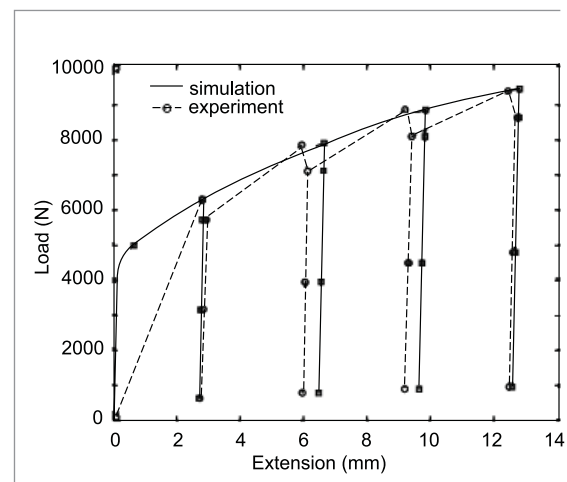


FIGURE 3: Load-extension curve for specimen B for a series of loading-unloading cycles.

REFERENCES

- [1] E. Marin, P. Dawson, *Comput. Method Appl. Mech. Eng.* **165**, 1 (1998).
- [2] E. Marin, P. Dawson, *Comput. Method Appl. Mech. Eng.* **165**, 23 (1998).
- [3] D.E. Boyce, P.R. Dawson, B. Sidle, T. Gnäupel-Herold, accepted for publication in *Computational Materials Science*.

High Resolution Depth Profiling in a Plane Strain Channel Section

The emergence of new materials has created additional challenges in the simulation of sheet metal forming with one problem being the accurate prediction of springback. The residual stresses responsible for springback can be measured non-destructively by two methods: synchrotron x-ray and neutron diffraction. Through improvements in methodology, neutron diffraction has made much progress in improving the spatial resolution down to 0.1 mm, thus enabling through-thickness stress measurements on sheets as thin as 0.8 mm.

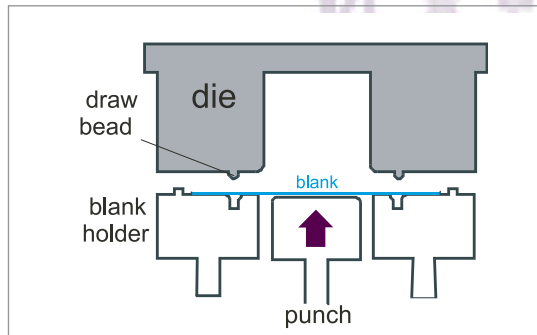


FIGURE 1:
Sketch of the channel draw (first stage).

Advances in steel production have brought about new kinds of steel, typically with substantial increases in strength without sacrificing formability. A significant fraction of steels is used in the form of sheet metal which is usually further processed through forming operations such as stamping and deep drawing. In order to ensure quality and cost effectiveness in the application of these processes for production parts, the simulation of various aspects of forming has become a key stage in the application of these materials. In order to characterize forming-related properties and to compare finite element codes used for the simulation, standardized tests are used in which specimens are deformed by large bi-axial strains using complex strain paths. For a number of years now there has been a good tradition of a strong collaboration between industrial concerns such as car companies and government/academia which entails participation in sheet metal forming benchmark tests.

One of the most recent tests is the “Numisheet 2005 Benchmark #3: Channel Draw/Cylindrical Cup” which is a two stage forming test consisting of a channel draw (Fig. 1), followed by a cup test on the channel side walls [1,2]. The concept was to verify not only the strain fields achieved during the two stage forming process, but also to test the ability of numerical models to predict both strain and stress fields during multi-stage forming processes. Accurate numerical results for the first stage forming and springback are essential to guarantee proper initial state variables for the subsequent stage simulation.

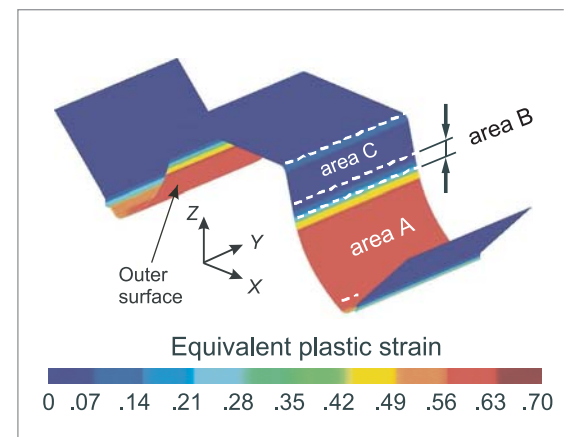


FIGURE 2:
Equivalent plastic strain distribution for a channel after springback with predicted strains. Neutron measurements were performed in area A.

The main parameter varied in this test was the draw bead penetration which essentially varies the magnitude of a bending/unbending cycle and acts as a pre-strain. The characteristic shape of a specimen with draw bead pre-strain is shown in Fig. 2. The curvatures of areas A, B and C (opening of the “U”) represent the springback and it is caused by through-thickness stresses.

T. Gnäupel-Herold¹
D.E. Green²
T.B. Stoughton³
M.A. Iadicola⁴
T. Foecke⁴

¹ National Institute of Standards and Technology
NIST Center for Neutron Research
Gaithersburg, MD 20899-8562

² University of Windsor
Windsor, ONT, Canada N9B 3P4

³ General Motors R&D Center
Warren, MI 48090-9055

⁴ National Institute of Standards and Technology
Metallurgy Division
Materials Science and Engineering Laboratory
Gaithersburg, MD 20899-8553

The task of measuring stresses with a minimum of seven locations through walls of curved panels with thicknesses ≤ 1 mm poses a considerable challenge because it essentially requires neutron beams to be no more than 0.1 mm wide in the thickness direction. In order to keep the data acquisition time within ≈ 1 h, aperture configurations were chosen such that the total illuminated gage volume was > 1 mm³. An example is shown in Fig. 3. It also illustrates the new concept of “shaped apertures” where for certain directions the incident beam aperture takes on the shape of the specimen, *e.g.*, by giving it a curvature. Depending on the aperture-to-specimen distance resolutions down to 0.1 mm can be achieved. It can be argued that, at the current state of beam optics for neutron diffraction, higher spatial resolutions < 0.1 mm become unfeasible due to beam divergence. Using this technique, a series of through-thickness measurements in area A of the channel sidewall was performed, the results of which are shown in Fig. 4.

The results of the neutron stress measurements highlight the long-known fact that springback decreases with higher draw bead penetration due to increased plastic deformation. In this forming experiment springback is characterized as the curvature of area A which generally decreases with increasing draw bead penetration. A similar tendency is visible in the stress distributions where the magnitude of compressive stresses at and near the outer surface (Fig. 2) increases with the draw bead penetration. However, the mechanical equilibrium of both stresses and bending moments appears to be severely affected, most likely by intergranular stresses as suggested by the stresses becoming overall compressive at higher draw bead penetrations and therefore higher levels of accumu-

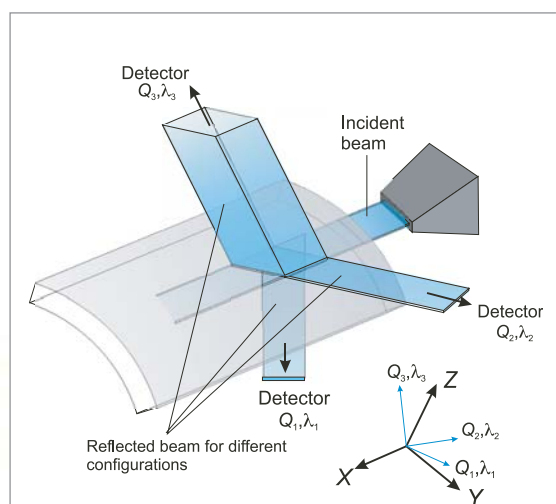


FIGURE 3: High spatial resolution strain measurement on sheet metal specimens. The three reflected beams Q_1 , Q_2 , Q_3 represent three different orientations of the specimen.

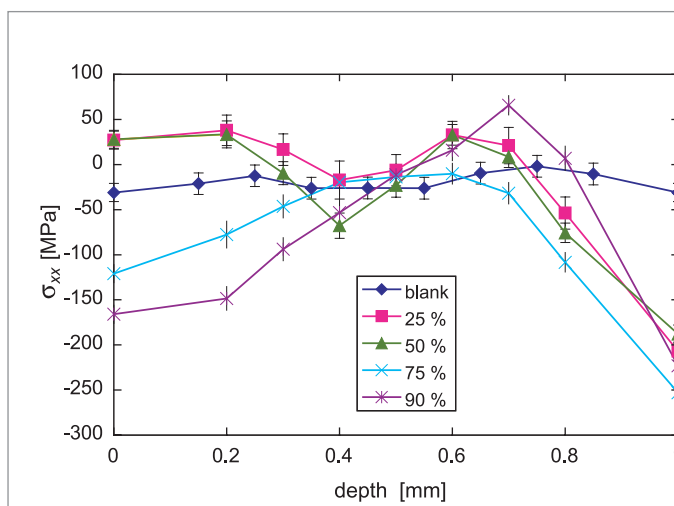


FIGURE 4: Through-thickness residual stresses (x-direction), measured in area A.

lated plastic deformation. Intergranular stresses arise because when stress is applied grains with a certain orientation yield at different stresses than neighboring grains (having different orientations). Upon release of the applied stress, grains with different orientations relative to each other are typically at different states of residual stress. This issue cannot be resolved from the data present; it requires either the averaging over different (hkl) or the tracking of the change in *d*-spacing on a specimen with a similar deformation path but without long-range residual stresses (such as through thickness stresses).

The neutron diffraction results presented here, although incomplete, represent a step forward in the methodology of making strain measurements at the highest possible spatial resolution at moderate durations for data acquisition. The demand for such measurements arises where two requirements have to be met at the same time: that for spatial resolution ≈ 0.1 mm and that for good averages, *i.e.*, that the strains measured are representative for larger areas > 10 mm². The latter is problematic for synchrotron radiation diffraction but becomes a necessity in neutron diffraction due to the need for large gage volumes.

REFERENCES

- [1] M.C. Oliveira, A.J. Baptista, J.L. Alves, L.F. Menezes, D.E. Green, T. Gnaeupel-Herold, M.A. Iadicola, T. Foecke, T.B. Stoughton, *Two Stage Forming: Experimental and FE Analysis*, Proceedings of International Deep Drawing Research Group (IDDRG), June 2006, Porto, Portugal.
- [2] D.E. Green, T.B. Stoughton, T. Gnaeupel-Herold, M.A. Iadicola, T. Foecke, *Influence of Drawbeads in Deep Drawing of Plane-Strain Channel Sections*, Proceedings of IDDRG, June 2006, Porto, Portugal.

Neutron Imaging Facility at BT-2 and Tomography of Fuel Cells

Understanding and modeling the polymer electrolyte membrane (PEM) fuel cell is critical to optimally engineering these systems for consumer vehicles. Until recently, experimental data on the water distribution inside an operating fuel cell has been unavailable to researchers modeling these devices. However, the application of neutron radiography to image PEM fuel cells is now providing valuable insight into the details of where liquid water is formed during fuel cell during operation [1-4]. This is due to the unique ability of neutrons to penetrate the components of the fuel cell and yet still scatter strongly from hydrogen bound mainly in water molecules. Neutron radiography is sensitive to water at the level of $500 \mu\text{g}/\text{cm}^2$ (depending on the conditions of the experiment). In order to make this capability widely available to the scientific and engineering communities in the United States, the NCNR in collaboration with the NIST Physics Laboratory Ionizing Radiation Division and General Motors Fuel Cell Activities has built a new facility for neutron radiography that incorporates extensive infrastructure support for fuel cell experiments.

The Neutron Imaging Facility is a thermal neutron radiography facility located at BT-2 at the NCNR. It is depicted in Figs. 1 and 2. It was built and commissioned in early 2006 after the previous Neutron Imaging Facility located at BT-6 was decommissioned. This new facility provides ample room to set up fuel cell experiments and provides fuel cell testing equipment, hydrogen, nitrogen, air, deionized water and chilled water inside the C100 confinement room. To do this, an extensive safety review was required to understand the hazards associated with the use of hydrogen gas, which is a potential hazard. After extensive computational fluid dynamics modeling using the NIST Fire Dynamics Simulator (FDS) [5] available through the Building and Fire Research Laboratory, it was determined that hydrogen accidentally or purposefully released in the room would turbulently mix with surrounding air lowering the concentration below the flammability limit (4 % in air by volume) at 1.2 m above the release point at the

maximum release rate of 22.4 L/min. Throughout the room the concentrations were found to be 40 times lower than the flammability limit. This maximum release rate is assured because hydrogen used in the facility is produced by an electrolysis unit at a maximum rate of 18.8 L/min. No stored inventories of

hydrogen are used, so the possibility of an accidental release of a large amount of hydrogen does not exist.

Running fuel cells requires accurate control over the mass flow rate of hydrogen, air and nitrogen that are supplied to the fuel cell. In addition to controlling the mass flow, the humidity of the gases must also be controlled from 0 % to 100 % for a range of tempera-



FIGURE 1:
Photo of the Neutron Imaging Facility at BT-2

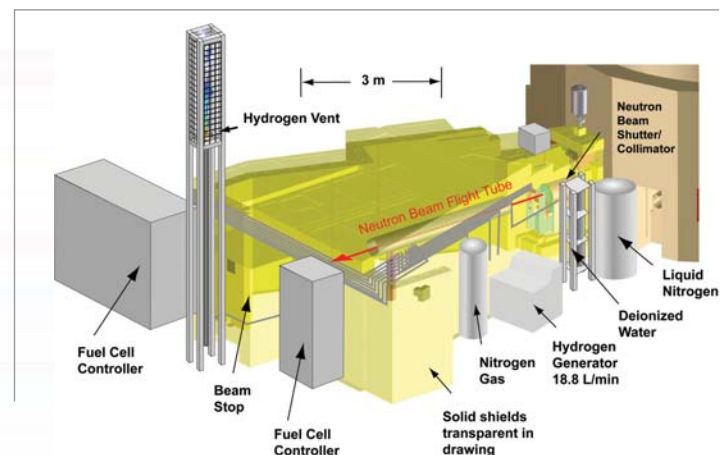


FIGURE 2:
Schematic drawing of the Neutron Imaging Facility at BT-2.

D.L. Jacobson¹
D.S. Hussey¹
M. Arif¹
J. Gagliardo²
J. Owejan²
T. Trubold²

¹ Ionizing Radiation Division
National Institute of Standards and Technology
Gaithersburg, MD
20899-8461

² General Motors
Fuel Cell Activities
Honeoye Falls, NY
14472

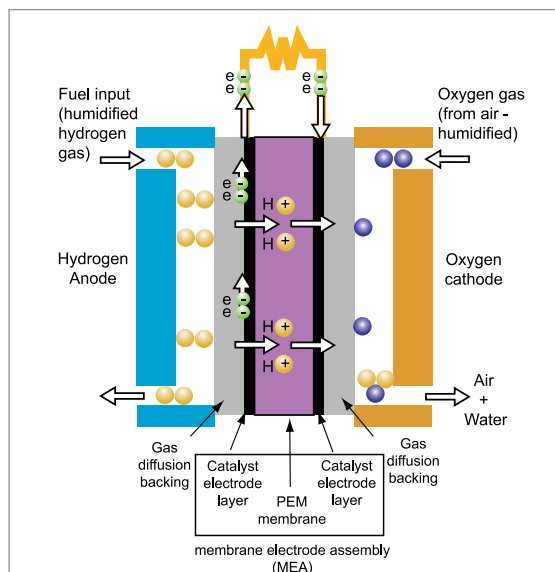
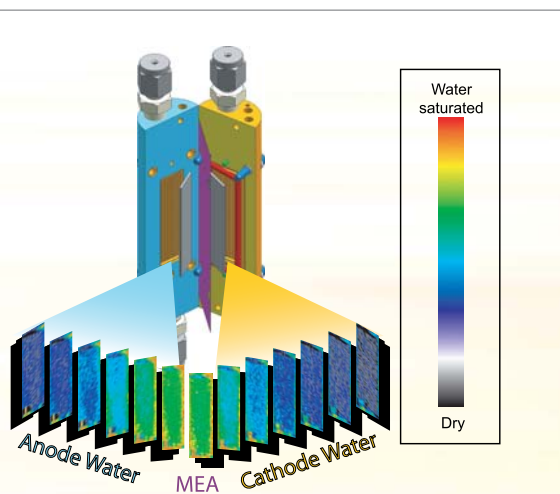


FIGURE 3:
Schematic diagram of the operation of a fuel cell.

tures. These functions are performed using a fuel cell test stand that incorporates accurate mass flow control for all gases used by the cell. In addition to mass flow control, an electronically controlled electrical load can also be applied. All of these features are automated to allow users to step through an extensive series of testing protocols.

Researchers using the facility are only required to bring fuel cells of their own design to the facility. A diagram of how a fuel cell works is shown in Fig. 3, and an example of a fuel cell designed for the purpose of demonstrating tomography is shown in Fig. 4. Fig. 4 also shows the reconstructed 3-D distribution of water in the fuel cell as measured at the facility. Both the anode and the cathode are distinguished, and the water distribution is shown in slices going from the anode to the cathode. Although water is produced on the cathode side during cell operation, these data demonstrate that in the steady state, unexpectedly, the anode side also remains wet. Water formed on the cathode may be transferred back to the anode through various mechanisms such

FIGURE 4:
Results from neutron tomography of a fuel cell running in the steady state. The upper part shows a 3-D drawing of the cell studied and the lower part displays the tomography data showing water in slice planes scanned from anode to cathode on either side of the membrane electrode assembly (MEA). A significant finding shown here is that water is observed distributed on both the anode and the cathode.



as chemical back-diffusion and hydraulic pumping associated with the material properties of both the membrane electrode assembly and the gas diffusion media. In addition to these source mechanisms, gas flow (of hydrogen) is much less effective at removing water on the anode side compared to the cathode side where the much higher flow rate of air aids in water removal.

Although this new facility is optimized to provide state-of-the-art fuel cell systems control infrastructure for fuel cell developers, it is by no means limited to the study of fuel cells alone. This facility is open to a diverse user community through formal peer reviewed research proposals. Applications of neutron imaging to a variety of non-destructive and *in situ* investigations, from the dynamics of two phase fluid flows to geology and beyond are expected. Future developments for the facility will produce an order of magnitude increase in image resolution as well as a further expansion of fuel cell testing infrastructure to allow freeze-thaw testing of fuel cells.

REFERENCES

- [1] R.J. Bellows, M.Y. Lin, M. Arif, A.K. Thompson, D. Jacobson, *J. Electrochem. Soc.* **146**, 1099 (1999).
- [2] M.A. Hickner, N.P. Siegel, K.S. Chen, D.N. McBrayer, D.S. Hussey, D.L. Jacobson, and M. Arif, *J. Electrochem. Soc.* **153**, A902 (2006).
- [3] P.A. Chuang, A. Turhan, A.K. Heller, J.S. Brenizer, T.A. Trabold, and M.M. Mench, in *FUEL CELL 2005, 3rd International Conference on Fuel Cell Science, Engineering and Technology*, pp. 31-37, ASME Proceedings, New York (2005).
- [4] D. Kramer, J. Zhang, R. Shimoi, E. Lehmann, A. Wokaun, K. Shinohara, and G. G. Scherer, *Electrochim. Acta* **50**, 2603 (2005).
- [5] NIST Fire Dynamics Simulator and Smokeview <http://fire.nist.gov/fds/>.

Development of New Cold Neutron Sources at the NCNR

The NCNR is planning an upgrade of the existing cold neutron source in addition to the proposed new cold neutron source that is central to the expansion initiative announced in February, 2006. A large volume, liquid deuterium (LD₂) source is being developed as a replacement for the advanced liquid hydrogen source, Unit 2, installed in 2002. It will reduce the effective temperature of the source spectrum from 38 K to 28 K, providing gains of at least 50 % for wavelengths greater than 4 Å, and more than a factor of two for wavelengths greater than 9 Å. The second source, for the proposed west guide hall, is necessarily a small volume of liquid hydrogen (LH₂) installed in BT-7 that will have the same spectral shape as Unit 2, but about twice its brightness.

As in the past, the neutron performance and energy deposition in these sources is simulated using the Monte Carlo transport code, MCNP. Figure 1, a geometry plot of the MCNP model, shows locations of the proposed sources. During spring and early summer, design of the LH₂ source has taken priority in preparation for the NCNR Expansion Initiative Workshop, and the Facility Developments section of this report contains some information about it. The cryostat assembly of this source, including the source, insulating vacuum, helium containment and D₂O cooling jacket, must have a diameter of less than 150 mm, so the moderator vessel has an OD of 110 mm with an exit cavity of 80 mm ID, and an optimum LH₂ thickness of about 4 mm. A 300 W to 400 W nuclear heat load is expected, not including refrigerator load-line and condenser losses.

Unlike BT-7, the cryogenic beam port, CT, has a 560 mm ID thimble, offering space for a large volume of LD₂. A wide range of sizes and shapes have been analyzed, from a "small", 20 L LD₂ vessel (with several percent hydrogen) to the maximum size, 460 mm OD, 60 L, vessel that could be installed in CT with the

required vacuum, He and D₂O jackets. The design will be optimized by varying the vessel diameter and length, the LH₂ content, if any, and the reentrant-hole width and depth, subject to the constraint of full illumination of the CTE (East) and CTW beam ports. Although the addition of H₂ can increase the brightness of an undersized LD₂ source, a large volume of LD₂ will produce the lowest effective temperature. This distribution will double the brightness of the longest wavelengths ($\lambda > 9$ Å), but will decrease the intensity at short wavelengths ($\lambda < 4$ Å). It is possible to adjust the shape of the LD₂ source spectrum, somewhat, by adding a small amount of hydrogen, and using a deeper reentrant hole.

A 35 L, 38 cm x 38 cm vessel was chosen as a compromise to mitigate the losses below 4 Å, and present a 2000 W to 2500 W heat load that could potentially be cooled by the existing refrigerator. Many choices concerning the LD₂ source were made last year, however, prior to the announcement of the expansion initiative. A new refrigerator may now be required because tests have shown that the capacity of our refrigerator is likely insufficient for the addition of the BT-7 source to the Unit 2 load. The new refrigerator would have the capability of cooling both the LD₂ and BT-7 sources. Full-scale mockups of both will be tested to ensure that each can be cooled with a naturally circulating thermosiphon; Unit 2 has operated very reliably in this mode.

P. Kopetka
R.E. Williams
J.M. Rowe

NIST Center for
Neutron Research
National Institute
of Standards and
Technology
Gaithersburg, MD
20899-8560

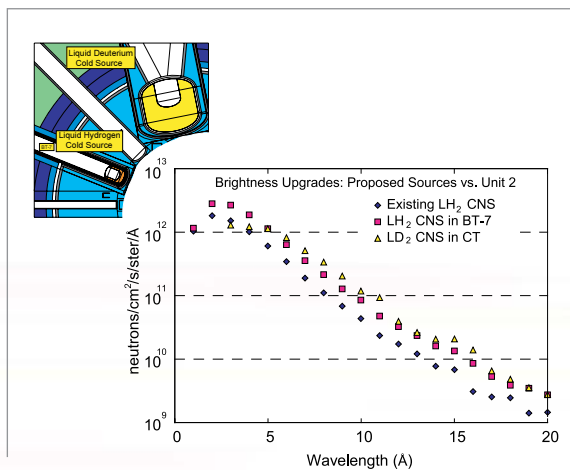


FIGURE 1: Left: northwest region of the NBSR core, showing the proposed cold neutron sources (CNS) upgrades. The existing LH₂ source in the CT port will be replaced by a large-volume, 35 L liquid deuterium source, and a new LH₂ source, just 0.75 L, will be installed in BT-7 for the West Guide Hall. Right: brightness comparison of the proposed CNS to Unit 2.

Improved Analysis of Short-lived Neutron Activation Products in Foods

TABLE 1:

LOD ranges and LOD/LOQ improvement factors for 16 elements in 40 TDS foods with Compton suppression INAA. NaCl content from < 0.005 % to 3.6 % mass fraction	Element Nuclide	keV	half-life	LOD range ^a mg/kg	average improvement factor vs. singles	number of foods > LOD	number of foods > LOQ
The Total Diet Study (TDS), sometimes called the market basket study, is an ongoing FDA program that determines levels of various contaminants and nutrients in foods. FDA's Laboratory at the NCNR provides quality assurance instrumental neutron activation analysis (INAA) for this FDA's this program [1]. To improve element limits of detection [2] (LODs), especially for iodine (recently added to the TDS Program), a Compton suppression system that discriminates against strayscattered background photons by using a coincident signal from a scintillator surrounding the Ge detector, previously used for prompt gamma-ray activation analysis, was converted to an INAA instrument. Combined with new irradiation and counting procedures, LODs improved by up to a factor of 4 for 16 elements with short-lived neutron capture products (half-lives of about 2 min to 1.5 d). Iodine mass fractions (0.075 to 2.03) mg/kg were measured in 17 of 40 TDS foods, with LODs ranging from (0.03 to 1.4) mg I/kg.	¹²⁸ I	443	25.0 min	0.029-1.35	1.38	17	9
	²⁴ Na	1368, 2754	15.0 h	0.68-26	1.28	40	40
	³⁸ Cl	1642, 2168	37.2 min	0.58-29	1.49	40	40
	⁴² K	1524	12.36 h	9.6-636	1.76	39	34
	⁵⁶ Mn	847	2.58 h	0.0041-0.22	1.74	38	35
	⁴⁹ Ca	3084	8.72 min	1.13-169	1.74	40	37
	²⁷ Mg	844	9.46 min	1.5-99	1.71	40	38
	⁶⁶ Cu	1039	5.10 min	0.22-11.9	2.04	13	1
	¹³⁹ Ba	166	1.40 h	0.72-34	1.13	0	0
	^{69m} Zn	439	13.76 h	19-880	1.36	1	0
	^{80m} Br	616	4.42 h	0.056-2.8	1.57	38	23
	²⁸ Al	1779	2.25 min	0.60-18	1.12	15	7
	⁵¹ Ti	320	5.76 min	0.83-32	1.28	3	3
	⁵² V	1434	3.75 min	0.010-0.22	1.42	10	4
	^{87m} Sr	388	2.81 h	1.0-53	1.36	2	0
	⁷⁶ As	559	26.32 h	0.28-15	1.50	0	0

^a e.g., for I, 9 of the 17 values > LOD were also > LOQ

Irradiation facilities at the NCNR, accessed through "rabbit tubes" (RTs), are highly thermalized. To determine the best irradiation site for iodine measurements (*i.e.*, which location had the greater epithermal and fast neutron component), NaCl/KI standards were irradiated in central and peripheral positions in RT1 and RT4. The central RT1 location was chosen for irradiations because it showed a 16 % enhancement of iodine activity over Na and Cl activity vs. the RT4 peripheral location. Forty foods from the TDS Program, multielement standards, NaCl fluence/geometry monitors, blanks, and control portions (NIST SRMs 1572 Citrus Leaves, 1566a Oyster Tissue, 1549 Milk Powder, and 1846 Infant Formula) were analyzed. Irradiations were performed for 10 s with counts beginning 2 to 3 min later. Count times were 30 min, with spectral data also saved after an initial 10 min count time for analysis of the short-lived species.

Compton suppression INAA results for TDS foods were compared to previous INAA procedures that used RT4 with singles counting and a 9 % relative efficiency Ge detector. ("Singles" are data collected at

the Ge detector without any reference to coincidence background reductions.) Figure 1 shows the effect of Compton suppression for iodine analysis compared to a simultaneous singles count for the same system and to the previous procedure. For all foods, an LOD improvement of about a factor of 4 was observed. Compton suppression results yielded LODs (and therefore limits of quantitation: LOQs) an average of 40 % lower than for singles data collected on the same system. A summary of the results for 16 elements in 40 TDS foods is given in Table 1. Greatest improvement is shown for Cu, K, Mn, and Ca. For control SRMs, agreement with certified values was found for all elements (All z-scores are < 1.7, where scores < 2 indicate agreement. A z-score of +1.7 corresponds to a measurement being 1.7 standard deviations above the mean [3].)

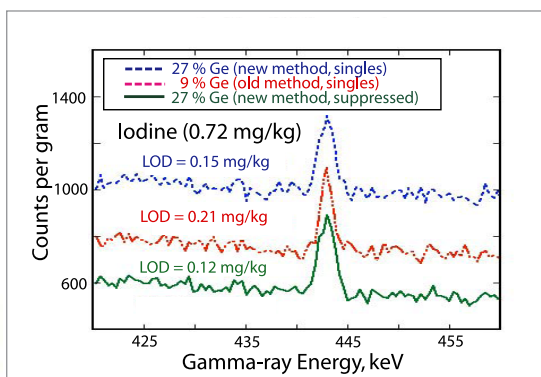


FIGURE 1.

Comparison of spectral data [30 min count times] for the iodine region for TDS food # 177 vanilla ice cream, light. Top and bottom spectra are from the present study (portion mass: 2.0 g). Middle spectrum is from previous work (portion mass 1.6 g).

REFERENCES

- [1] Total Diet Study website: <http://www.cfsan.fda.gov/~comm/tds-toc.html>
- [2] L.A. Currie, Anal. Chem. **40** (1), 586 (1968).
- [3] M. Thompson, R. Wood, J. AOAC Int. **76**, 926 (1993).

D.L. Anderson
W.C. Cunningham

Elemental
Research Branch
(HFS-338)
U.S. Food and Drug
Administration
College Park, MD
20740-3835

The New SRM 695 for Trace Elements in Multi-Nutrient Fertilizer

During the past seven years, several states within the U.S. have enacted new regulations that limit the amounts of selected non-nutritive elements in fertilizers. Internationally, several countries including Japan, China, and Australia, and the European Union also limit the amount of selected elements in fertilizers. Fertilizer manufacturers and state regulatory authorities, faced with meeting and verifying these limits, need to develop analytical methods for determination of the elements of concern and to validate results obtained using these methods. A new Standard Reference Material, SRM 695 Trace Elements in Multi-Nutrient Fertilizer, was developed to help meet these new requirements. SRM 695 has recently been issued with certified mass fraction values for 17 elements, reference values for five elements, and information values for two elements.

Until 1998, U.S. fertilizer manufacturers generally were required to guarantee only the nutrient content of their products. However, the recent discovery of high levels of As in some iron-based fertilizer materials and high levels of Cd in some zinc-sulfate based fertilizer materials prompted some states to enact regulations limiting the amount of selected non-nutritive (potentially toxic) elements in fertilizer materials. To date, ten states have enacted or proposed regulations, and other states are expected follow suit. When the non-nutritive metals As, Cd Co, Hg, Mo, Ni, Pb, Se and Zn were first limited by regulation in the U.S., there were few certified reference materials (CRMs) available to assist manufacturing and regulatory laboratories in method development and measurement validation and none with matrices similar to typical agricultural or homeowner fertilizer blends. NIST worked with the members of the manufacturing and regulatory community to develop the new SRM 695 Trace Elements in Multi-Nutrient Fertilizer.

The experimental design for certification of SRM 695 was based on the use of two or more independent analytical techniques performed at NIST to provide values for all regulated elements and for the nutrient elements (B, Ca, Cu, Fe, K, Mg, Mn, N, and P) and other elements if possible. The approach relied on non-destructive analytical techniques, instrumental neutron activation analysis (INAA), prompt gamma ray activation analysis (PGAA) and x-ray fluorescence spectrometry (XRF) for most elements. A combination of inductively coupled plasma optical emission spectrometry (ICP-OES), ICP-mass spectrometry (MS) and cold vapor isotope dilution (CV-ID) ICP-MS was used for six elements.

The certified values for 17 elements and reference values for five elements are shown in Table 1, together with the analytical techniques used. Certified values for all elements except As and Hg are the unweighted means of results from two or three analytical methods. The uncertainty listed with each value is an expanded uncertainty about the mean, with coverage factor 2, calculated by combining a between-method variance with a pooled, within-method variance [1] following the ISO Guide to the Expression of Uncertainty in Measurement/NIST Special Publication 1297 [2,3]. Reference values were provided when only one analytical technique was used or in cases for which there was not a complete evaluation of all sources of uncertainty. (See Ref. 4 for a complete description of certified, reference and information values for SRMs.)

TABLE 2. CERTIFIED AND REFERENCE MASS FRACTION VALUES FOR SRM 695

Element	Methods Used	Certified Values
As	INAA	(200 ± 5) mg/kg
Ca	INAA, XRF	2.26 % ± 0.04 %
Cd	INAA, ID-ICP-MS	(16.9 ± 0.2) mg/kg
Co	INAA, XRF	(65.3 ± 2.4) mg/kg
Cr	INAA, XRF	(244 ± 6.2) mg/kg
Cu	ID-MS, ICP-OES, XRF	(1225 ± 9) mg/kg
Fe	INAA, PGAA, XRF	3.99 % ± 0.08 %
Hg	ID-MS	(1.955 ± 0.036) mg/kg
K	PGAA, XRF	11.65 % ± 0.13 %
Mg	INAA, XRF	1.79 % ± 0.05 %
Mn	INAA, PGAA, XRF	0.305 % ± 0.005 %
Mo	ICP, XRF	(20.0 ± 0.03) mg/kg
Ni	ICP, XRF	(135 ± 2) mg/kg
Pb	ICP-OES, XRF	(273 ± 17) mg/kg
Na	INAA, XRF	0.405 % ± 0.07 %
V	INAA, XRF	(122 ± 3) mg/kg
Zn	INAA, XRF	0.325 % ± 0.005 %

Element	Method	Reference Values
Al	INAA, XRF	0.61 % ± 0.03 %
B	PGAA	0.111 % ± 0.002 %
N	PGAA	13.9 % ± 0.04 %
P	XRF	7.2 % ± 0.1 %
Se	INAA	(2.1 ± 0.1) mg/kg

REFERENCES

- [1] M.S. Levenson, D.L. Banks, K.R. Eberhardt, L.M. Gill, W.F. Guthrie, H.K. Liu, M.G. Vangel, J.H. Yen, N.F. Zhang, *J. Res. NIST* **105**, 571 (2000).
- [2] Guide to the Expression of Uncertainty in Measurement, ISBN 92-67-10188-9, 1st Ed. ISO, Geneva, Switzerland, (1993).
- [3] B.N. Taylor, C.E. Kuyatt, NIST Special Publication 1297, Guidelines for Evaluating and Expressing the Uncertainty of NIST Measurements Results 1994 Edition.
- [4] W.E. May, T.E. Gills, R.Parris, C.M. Beck II, J.D. Fassett, R.J. Gettings, R.R. Greenberg, F.R. Guenther, G. Kramer, B.S. MacDonald, S.A. Wise, Definitions of Terms and Modes Used at NIST for Value-Assignment of Reference Materials for Chemical Measurements NIST Special Publication 260-136 (1999).

E.A. Mackey¹
 C.N. Fales¹
 R.R. Greenberg¹
 M.P. Kronise¹
 S. Leigh¹
 S.E. Long¹
 K.E. Murphy¹
 R. Oflaz¹
 J.R. Sieber¹
 M.S. Rearick¹
 L.J. Wood¹
 L.L. Yu¹
 P.F. Kane²
 W. Hall³

¹ National Institute of Standards and Technology Analytical Chemistry Division Gaithersburg, MD 20899-8390

² Office of Indiana State Chemist Purdue University West Lafayette, IN 47907-2063

³ The Mosaic Company Mulberry, FL 33860

Residual Stress Determination as a Benchmark for a New Strain Measurement Technique

A friction stir welded (FSW) butt joint of 25.4 mm thick plates of aluminum alloys 7050-T7451 and 2024-T351 was used to measure cross-sectional maps of residual stresses using neutron diffraction and the recently developed contour method. Such thicknesses represent the state-of-the-art in FSW, and both measurement techniques validated that ability of FSW to produce low-magnitude stresses.

Friction Stir Welding (FSW) is a joining process which has seen remarkable growth in research, development and application in recent years. This is due to the ability of FSW to join a variety of alloys that can be dissimilar, difficult to weld in fusion welding, and to produce defect free welds with favorable strength properties without going through a melting process. FSW is heavily utilized in the aircraft industry where it offers the possibility of unitized structures made up of parts of different alloys and joined by FSW, thus reducing the cost associated with alignment and assembly.

A significant potential contributor to the durability behavior of FSW joints and surrounding material, however, will be the magnitude and distribution of residual stresses as an important influence on crack growth rates. Therefore, knowledge of residual stresses is crucial if accurate property measurements are required. Neutron diffraction is among the best-established methods for measuring sub-surface, tri-axial residual stresses which makes it useful as a comparative benchmark for other techniques such as the contour method [1]. The basic idea of this technique is as follows: One starts with an undisturbed part containing the stresses to be determined. Then, the part is cut in two which releases stresses and causes distortion on the cut surfaces of the two halves. The distortions can be measured very precisely by, for example, confocal laser ranging probes (used here).

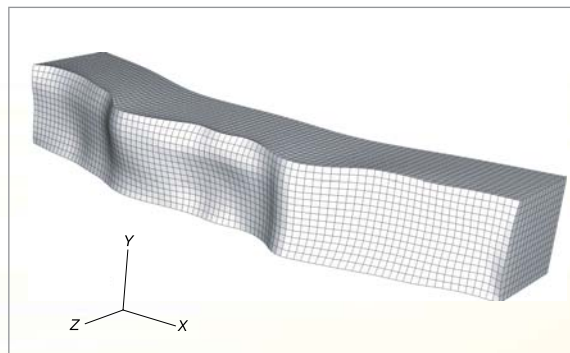


FIGURE 1:

Elastic finite element of half of test specimen with cut surface deformed into opposite of measured surface contour. Displacements magnified by factor of 1000. Part dimensions before the cut were 162(x) × 54(z) × 25.4(y) (in mm).

Using this numerical representation of the cut surface virtual stresses are applied to force the surface back into its original shape. The stresses applied in the last step are equal but opposite in sign to residual stresses before the cut.

Neutron measurements were performed along the x-direction (Fig. 1) close to the surfaces and in the mid-plane with 19 locations each (see Fig. 2 for spacing). After completing the neutron measurements the specimen was then cut by EDM and the contour analysis was performed (Fig. 1) using a mesh with approximately 30 locations per mm². The stresses obtained by the two methods are shown in Fig. 2.

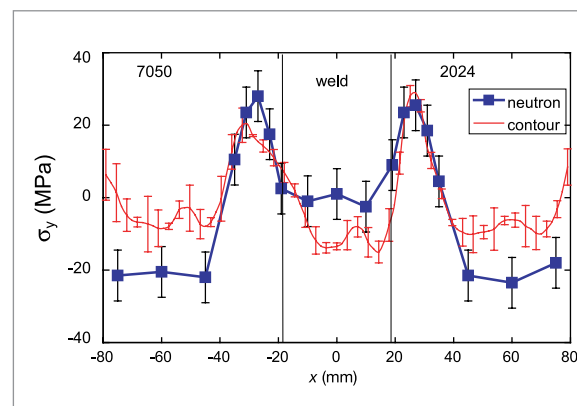


FIGURE 2:

Stresses normal to the mid-plane (Fig. 1) at 12.7 mm depth.

There is a general agreement between the two methods, and the findings show the ability of FSW to produce welds with low stress magnitudes (6 % of the yield strength) even in structures as thick as 25 mm. The subtle differences can be attributed to variations of the unstressed d-spacing and to the presence of intergranular stresses. The first is caused by inhomogeneous mixing of the two parent materials [2], creating mm-sized regions with differing d_0 , the second is due to the fact that both parent plates were stretched by 1.5 % prior to welding, thus creating grain-orientation dependent stresses between grains. The contour method, while being destructive, demonstrates superior area resolution and it is independent of the two factors affecting the neutron measurements.

REFERENCES

- [1] M.B. Prime, *Journal of Engineering Materials and Technology* **123**, 162 (2001).
- [2] M.B. Prime, T. Gnäupel-Herold, J.A. Baumann, R.J. Lederich, D.M. Bowden, R.J. Sebring, accepted for publication in *Acta Mat.*

M.B. Prime¹
T. Gnäupel-Herold²
H.J. Prask²
J.A. Baumann³
R.J. Lederich³
D.M. Bowden³
R.J. Sebring³

¹ Los Alamos National Laboratory
Los Alamos, NM 87545

² NIST Center for Neutron Research
National Institute of Standards and Technology
Gaithersburg, MD 20899-8562

³ The Boeing Company
St. Louis, MO 63166-0516